Impact of an Atmospheric Profiling Mission on NWP

Luis Kornblueh and Lennart Bengtsson
Max-Planck-Institute for Meteorology
Bundesstr. 55, D-20146 Hamburg, Germany

Gottfried Kirchengast
Institute for Meteorology and Geophysics
University of Graz
Halbärthgasse 1, A-8010 Graz, Austria

Xiang-Yu Huang, Per Høeg, and Georg Bergeton Larsen
Danish Meteorological Institute
Lyngbyvey 100, DK-2100 Copenhagen, Denmark

26 August 2000

A/1-3378/98/NL/GD

Study of Potential Utility of GNSS Occultation Signals for an Atmospheric Profiling Earth Watch Mission

by
Luis Kornblueh, Gottfried Kirchengast, and Xiang-Yu Huang

ESA STUDY CONTRACT REPORT

No ESA Study Contract Report will be accepted unless this sheet is inserted at the beginning of each volume of the report

ESA CONTRACT NO.	SUBJECT:		NAME OF CONTRACTOR
12954/98/NL/GD	Study of Potential Utility of GNSS Occultation Signals for an Atmospheric Profiling Earth Watch Mission		Max-Planck-Institut für Meteorologie
ESA CR( ) NO.	STAR CODE	No. of Volumes — This is volume No:	CONTRACTORS REFERENCE

ABSTRACT:
The potential impact of radio occultation measurements based on different constellations of Low Orbiting Satellites (LEOs) and a Global Navigation Satellite Systems has been studied. For this purpose a conventional data assimilation system based on the Optimal Interpolation (OI) technique has been used.
The constellations of LEOs have been selected by defining several statistical measures to assure good covergage with observations for a one, six, twelve, and twenty-four LEO setup. Based on the ECMWF reanalysis for a periode in January 1987 radio occultations have been simulated by the wave-optics methode. This set of observations have been completed by the original used observations of the ECMWF reanalysis after blacklisting and quality checking. This observations have been used in a standard intermittent procedure (6 hourly) to generate forecasts. The measure to analyse the results is the anomaly corelation.
The final result shows a promising performance of the system. Another important result is a saturation of the information content for specific constellations of GNSS and LEO satellites.

The work described in this report was done under ESA contract. Responsibility for the contents resides in the author or organisation that prepared it.

Names of authors:
Luis Kornblueh, Gottfried Kirchengast, Xiang-Yu Huang

NAME OF ESA STUDY MANAGER	ESA BUDGET HEADING	
Paul Ingmann DIV. Earth Science Division		

Contents

1 Introduction **3**

2 Satellite mission scenario **5**

2.1 Generic GRAS Observational Requirements 6

2.2 Detailed Description of Constraints 7

2.3 Basic Scenario Setup 9

2.4 Calculations of Baseline Scenarios 10

2.5 Analysis of Occultation Event Locations 10

2.6 The Format and Structure of all Result Plots 13

2.7 General Figure Structure of Baseline Scenario Results 14

2.8 Results of Mission Scenario Calculations 15

3 Creating of Realistic Scenarios **34**

3.1 Description of the Real Satellite Constellation Scenarios 36

3.2 Conclusions on Mission Scenarios 70

4 Definition of Mission Scenarios for the Assimilation Experiment **71**

5 Mission Scenario Definition Constraints **72**

5.1 The Penalty Function Concept 72

5.2 Definition of Penalty Functions 72

5.3 Computation of Performance Descriptors 75

6 Assessment Results and Discussion **76**

6.1 Summary of Mission Scenarios 76

6.2 Constellation Performance Assessment 76

6.3 Assessment Refinement by Latitudinal Statistics 79

7 Definition of an OSSE Study Test Mission Set **81**

7.1 Recommendation of Two Test Mission Options 81
7.2 Discussion of Options and Preferred Mission Set 81

8 Assimilation preparation **90**

9 Preparing the models state - a nudging application **92**

10 Assimilation Procedure **94**

10.1 Optimal Interpolation (OI) 96
10.2 GNSS RO preprocessing 97
10.3 Assimilation 101
10.4 Statistical Measures 103

11 Results and Conclusions **105**

1 Introduction

Because radio occultation measurements have been playing a very important role in the exploration of the atmospheres of the planets in the solar system (Kliore et al., 1965; Fjeldbo and Eshleman, 1968; Lindal et al., 1990; Lindal, 1992), the application of this technique to the atmosphere of the earth has been investigated as well. But in difference to the atmospheres of the other planets, where almost any new information was important, the exploration of the Earth's atmosphere raised significantly the accuracy requirements on the radio occultation measurements. The first radio occultation soundings of the Earth's atmosphere (Rangaswamy, 1976; Yakovlev et al., 1995) were not able to satisfy these requirements.

The situation changed significantly with the introduction of the US Global Positioning System (GPS). The use of the GPS system for the radio occultation measurements was suggested first by Gurvich and Krasil'nikova (in Russian 1987, in English 1990) and Melbourne et al. (1988). The GPS system consists of 24 operational satellites equipped with high-precision radio transmitters. It is able to provide high accuracy measurements of the atmospheric refraction and a good coverage of the Earth's surface (TERMA Elektronik AS, 1998). This allow the GPS measurements to compete with other data sources for operational meteorology. The biggest advantage of the radio occultation technique is the weather independence. A general review on the radio occultation techniques can be found in Kursinski et al. (1997).

The results of the first proof-of-concept experiment with the satellite Microlab-1 with a GPS-receiver on board (launched on April 3, 1995) were very promising, even if the receiver was not perfect for this purpose (Ware et al., 1996). This experiment also gave an insight into the difficulties arising in processing and utilization of the radio refractometric data.

The basic method of processing radio refractometric data till recently has been the Abel inversion (Phinney and Anderson, 1968; Fjeldbo and Eshleman, 1968) with the approximation of local spherical symmetry, neglecting the horizontal gradients of the atmospheric refractivity in the vicinity of the ray perigees (Ware et al., 1996; Kursinski et al., 1996; Hocke, 1997; Anthes et al., 1997; Kuo et al., 1997; Rocken et al., 1997). In the stage of a proof-of-concept experiment this approximation was sufficient. Theoretical investigations of the potential accuracy and horizontal resolution of the Abelian inversion (Gorbunov and Sokolovskiy, 1993; Gorbunov et al., 1996a) indicated that its errors become significant in the lower troposphere due to the complicated structure of the humidity field. Another new development is the replacement of the Abelian by a Fresnel inversion (Mortensen and Høeg, 1998).

The information content of radio occultation data for data assimilation in general was explored as part of a ESA study (TERMA Elektronik AS, 1998). Due to the fact that the simulation of a full data assimilation cycle for radio occultation data is impossible with the current available measurements a very general approach has been used. Assuming that the radio occultation receiver provides temperature data with global coverage a series of twin experiments were carried out assuming a homogenous distribution of simulated occultation measurements in both space and time. In this experiments it was assumed that observations were available from the top of a model atmosphere (e.g. 10 hPa) down to 300 hPa and further down to selected model levels until 850 hPa as lowest assimilation level, respectively. Real global model analysis data from the ECMWF reanalysis project where used. In the twin experiments

this real analysis data have been assimilated into the model with a forcing dominating the model. This is representing the true atmosphere. In the other runs the data have only been assimilated in assumed instrument observation regions between the top and the specific lowest level. A comparison between this different model runs shows the potential influence of later measured data on the state of the atmosphere. The results are showing remarkable improvements (about 75 %) in the reduction of error amplitudes and slightly better results in error phase. This results encourage the next step in the development of a data assimilation system. One important point to mention on this experiments are nevertheless the perfect global data coverage which can hardly be provided by real observations.

Numerical simulations of the tomographic reconstruction of the global atmospheric fields from the refractometric measurements performed by a multi- Low Earth Orbiting (LEO) satellite system (Gorbunov and Sokolovskiy, 1993) indicated that the number of the LEO satellites necessary for accurate reconstruction of the horizontal structure in the lower troposphere at a resolution of a Global Atmospheric Circulation Model is estimated to a few hundred. Such a big amount of LEO satellites is, however, extremely unlikely to become available in the future. In case of effective data-assimilation this amount can be, this is a first order estimation, significantly reduced to minimum of 12 – 16 LEO satellites and 46 Global Navigation Satellite System (GNSS) satellites with an reasonable coverage.

The logical next step in investigating the impact of radio occultation data is the simulation of the impact of real data on numerical weather prediction (NWP) models considering previous established satellite setups. This is the main task to be explored in this study.

The optimal way of utilizing refractometric data is a data assimilation framework such as Optimal Interpolation (OI) or 4d variational assimilation (4DVAR) into a global atmospheric circulation model (Eyre, 1994; Zou et al., 1995). This approach has very strong advantages compared with the tomographic reconstruction of the global atmospheric fields. It is capable of assimilating any amount of the data without resulting in high-frequency artifacts due to insufficient resolution, usual in the standard tomography. This advantage makes data-assimilation especially valuable in the situation when only one LEO satellite is available, and it is impossible to arrange a tomographic high-resolution scanning of the atmosphere. This method is also capable of assimilating any kind of measured data in an unique way. The problem of separation of the humidity and temperature influence on the refractivity, is also solved with this method automatically (Zou et al., 1995). As can be shown in the first attempt to assimilate radio occultation data (Zou et al., 1998a,b) this is in general possible. Unfortunately there are not enough data available to perform real experiments which show an improvement due to the additional radio occultation data. In the framework of an ESA study at MPI a 4DVAR operator has been developed (TERMA Elektronik AS, 1998). This can be used only in an operational 4DVAR environment which is presently available in Europe at ECMWF only. Work is ongoing in the CHAMP project of the Geoforschungszentrum Potsdam (GFZ-Potsdam) for the implementation of this operator in a data assimilation setup with the climate model ECHAM5 until 2002.

Due to the complexity of 4DVAR experiments in the expected size of this study and unpredictable problems as well as missing information on the error-covariance matrix essential for such a data assimilation setup, we suggest a more suitable system based on an Optimal Interpolation (OI) data assimilation scheme for the global case. This can be used together with

the MPI climate model ECHAM4 in forecast mode for the global coverage experiments.

The exploration of the NWP impact is split in four steps. First the setup of different satellite constellations is evaluated and the most promising in terms of spatial and time coverage are selected. The decision rules used are explained. Next step is the generation of the required observations out of predefined atmospheric states to accomplish the available standard and satellite observations for data assimilation usage. Third step is the data assimilation cycle itself. Finally conclusions have to be made up on the information gained.

2 Satellite mission scenario

Exploring the impact of GNSS Radio Occultation (RO) data on modern NWP systems requires the base information related to spatial and temporal sampling requirements. This requirements are given by the Report of the GRAS-SAG[1]. They are reviewed concerning their suitability briefly.

The basic requirements include horizontal and vertical sampling, both of which are associated (by the nature of the satellite-to-satellite sounding technique) with characteristic temporal sampling requirements for a given GNSS/LEO satellite constellation. Horizontal sampling expressed (to zeroth order) by the average sampling distance between individual occultation profiles depends strongly on the time interval allowed for a single sampling cycle based on the required time resolution. Vertical sampling, expressed by the average vertical distance of individual occultation rays sampled within a suitable height interval depends strongly on the sampling rate of the GNSS receiver(s) on board a LEO.

These interdependencies have to be kept in mind when focusing on reviewing the constellation-relevant requirements in the GRAS-SAG report. One implication is that the vertical sampling requirement only weakly depends on a given constellation. Thus it can be considered an off-line topic with respect to a constellation study. The mission scenario study therefore concentrates on the sampling of the geographical (horizontal) space.

It is also very important to take into account typical natural constraints on GNSS/LEO constellations. The GNSS side is very strongly constrained by prescribed layout of the existing GPS and GLONASS (Russian Global Navigation Satellite System) space segments so that these can be used, favorably, as firm-fixed reference constellations.

The LEO side, however, has much more degrees of freedom. Without assuming some basic constraints for this side, the investigation of optimal constellations is prohibitive due to the very large space of options. Sensible a priori constraints as introduced below help to greatly reduce the space of scenario options. This allows for a tractable number of scenarios to be studied.

[1]Global navigation satellite system Receiver for Atmospheric Sounding - Science Advisory Group

		Temperature	Humidity	Bending Angle
Horizontal Domain		Global	Global	Global
Horizontal Sampling(1)		< 300 km(2)	< 300 km(2)	< 300 km(2)
Vertical Domain		surface to 1 hPa (0 - 50 km)	surface to 300 hPa (0 - 10 km)	surface to 80 km
Vertical Resolution		0.5 - 1.0 km	0.5 km	< 0.5 km or equivalent in time sampling
Time Resolution		1 - 6 hrs	1 - 6 hrs	1 - 6 hrs
Absolute	0 - 30 km	< 1 K	< 10 % or < 0.2 g/kg(3)	< 1 μrad or 0.4 %(3)
Accuracy	30 - 50 km	< 2 K	n/a	< 1 μrad or 0.4 %(3)
Timeliness		2 - 3 hrs	2 - 3 hrs	2 - 3 hrs

Table 1: Generic GRAS Requirements for Operational Meteorology

Notes:

(1) This would be the mean sampling distance between atmospheric profiles.

(2) This assumed 20 to 25 satellites carrying GRAS.

(3) Whatever is larger.

2.1 Generic GRAS Observational Requirements

This work is concerned with the planning for a suitable satellite constellation for atmospheric temperature and humidity measurements for NWP using the radio occultation technique. The expected advantages of the occultation technique for the purposes of NWP were already discussed in several ESA-Reports and in the scientific literature.

To take the full advantage of the occultation method, one should use the whole GNSS using their high performance radio transmitters in high orbits along with sophisticated receivers on LEO satellites. This combination allows to make radio occultation measurements for the Earth's atmosphere with an accuracy useful for applications in operational meteorology, or NWP, as well as in climate and in ionospheric research.

Table 1 gives, following the GRAS-SAG report, a compact overview of the needed accuracies for performing operational meteorology at a substantially improved level concerning the absolute data accuracy and the really global distribution of the measurements, provided the satellite constellation is properly designed.

The important improvements compared to present weather data collection systems (as readily seen from table 1) are the globally distributed horizontal sampling with mean inter-event distances of less than 300 km (and with a reasonable time resolution of the order of less than 6 hrs) combined with a vertical resolution of about 0.5 - 1 km for all measured parameters. Also the needed absolute accuracies for the measured physical parameters are perhaps only achievable with GRAS instruments and by using state of the art atmospheric models.

Given the most modern global NWP systems, which achieve resolutions of T_L319 (< 62.5 km) horizontally, the horizontal resolution (achieved within ~ 6 hrs) could even be much better than 300 km, allowing still to gain further information. And Local Area Models (LAMs),

which achieve today resolutions of $\sim$ 10 km could in principle exploit data with even higher geographic resolution.

Important to note in relation to the GNSS occultation method is that this is a method unique in vertical resolution and absolute accuracy but - being a limb sounding method - its horizontal resolution is best suited to resolve all scales down to the mesoscale (down to $\sim$ 100 km), but not finer scales. Even when thinking of a comparatively large constellation of $\sim$ 100 LEO receivers, the scales resolved will be typically $>$ 100 km within a 6 hrs sampling cycle. The physical resolution of a profile from a single event is $\sim$ 200 - 300 km. It seems thus reasonable to assume a maximum constellation of $\sim$ 25 satellites, geometrically resolving all scales down to the physical resolution measure of a single event, as a quite reasonable implementation.

Such a constellation seems to be an ideal backbone of a global operational meteorology observing system for horizontal scales down to some 100 km - and delivers vertical profiling of unique capability at this resolution; for horizontal scales smaller than 100 km it should be complemented by other space born observing systems (e.g. high-spectral resolution downlooking sounders).

Based on this brief review and evaluation of reasonable horizontal resolution requirements of GNSS occultation, we choose the largest constellations to consist of 24 satellites. Since good NWP impact can be expect already with a significantly lower number of satellites, we will study also smaller constellation scenarios comprising either 6 or 12 satellites.

Another constraint on choosing the largest constellation to consist of 24 LEO satellites arises from the tremendous cost of the forward modelling of larger setups.

2.2 Detailed Description of Constraints

For the satellite constellation the horizontal sampling requirements together with the given time resolution requirement are the major challenge. Before designing specific satellite constellations, we shall take a look on several useful general mission constraints in order to reduce the space of scenario options. We will fix only the main orbital design parameters within the subspace obeying these constraints.

As said previous, the whole GNSS constellation of (ideally) 24 GPS and 24 GLONASS satellites is used for our purposes. The GPS and GLONASS satellites are orbiting the Earth in groups of 6 – 8 satellite per orbital plane using 3 – 4 different orbital planes in circular orbits about 20000 km above the Earth's surface. These systems form our basic GNSS system in High Earth orbit and are therefore a fixed quantity.

For the LEO segment of the satellite network there is in principal a lot more freedom in designing the orbital parameters, the satellite numbers per orbit plane, etc., but for practical reasons (size, complexity, and last but not least the system costs), some reasonable a priori constraints are introduced in advance before we start to quantify different LEO satellite scenarios.

- We fixed the height of the LEO's to $\simeq$ 800 km (i.e., $a \simeq 7170$ km, a is the semimajor axis of the satellite orbit) above ground. There are several good reasons for doing this (e.g.

to design near-polar sun-synchronous orbits, where the LEO crosses always at the same local time the equator, to avoid large air drag but to dig not too deep into the Van Allen belts, etc.). It is also well known that the price per mass unit grows with orbit height and the LEO mass would be about the same for all potential orbits. Also recommended, and used, is a nearly circular orbit in order to render the occultation conditions about the same all over the orbit; an eccentricity of $e \simeq 0.001$ will be tolerated and will be a fixed setting.

- The argument of the perigee will be tendatively placed at $\omega \simeq 90°$ and is in fact fixed there to best fit Earth's ellipticity effects for high-inclined orbits.
- The epoch does not alter at all and is fixed to $T = 96213.5$ (31. July 96, 12.00 hrs) to match the epochs in the GPS/GLONASS *.tle files. Absolute time is not relevant for this study.

After fixing the first three Kepler parameters, the three remaining orbital quantities are to be fixed. So what can be changed is Ω the node, I the inclination, and M the mean anomaly of the LEO satellite orbit at a given epoch. It is useful for further work to make also some constraints on these free parameters:

- For a given number of orbits, the individual orbit nodes Ω shall be equally separated along the equator as baseline. In case of deviations from this rule it will be separately mentioned.
- Constraints for the mean anomaly are that given some satellites per orbit, the satellites shall be equally separated in the orbit as baseline (e.g. 3 LEO's will be separated by 120°). In case of deviations from this rule it will be separately mentioned.
- Theoretically the orbital inclination I, finally, is an almost free parameter, which can vary from $0° \leq I \leq 180°$, but practically $0° \leq I \leq 98°$ (sun-synchronous orbits are the most retrograde ones allowed) shall be used without significant loss of generality.

With these orbital geometry constraints defined we move on to also make reasonable assumptions for several other relvant parameters, before we can construct a real satellite scenario. Despite all the limitations the number of possible constellation scenarios is otherwise still much to large. These settings include:

- The total number of satellites in a LEO case shall be limited to $N \leq 24$ in order to limit run-time, but to nevertheless allow to reach the 300 km/6 hrs horizontal resolution goal set out by table 1 above.
- One occultation event simulation shall generally run for half a day (12 hrs), half of which (6 hrs) will finally be used for computing the presented statistical measures (the other half is for verification purposes).
- The simulation domain shall be global.

O=1	O=1	O=1
S=1	S=3	S=6
I=98	I=98	I=98
I=90	I=90	I=90
I=80	I=80	I=80
I=70	I=70	I=70
I=60	I=60	I=60
I=30	I=30	I=30
I=0	I=0	I=0

Table 2: Basic LEO Satellite Constellation Scenarios

Notes:
O denotes the number of orbital plane(s).
S is the number of satellites per orbital plane.
I marks the inclination of the orbital plane(s).

- The rays (GNSS-LEO) shall be straight line.
- The Earth figure shall be spherical.
- Visibilities are not of interest as baseline.
- Occultation antennae are generally $-\vec{v}$ & $+\vec{v}$ antennae with typical azimuths (180°/0°), elevations (27°) and a Threshold Power Beam Width (TPBW) of 90°.
- Occultation events are geolocated computing at a single height level (we chose 1 km height above sea level, to be matched with an accuracy of 100 m). This 1 km target height for straight line rays represents well, based on experience, the tropopause-crossing locations of real events for bended rays.

Based on the constraints above, the basin space for constellation scenarios is still big, since the total number of satellites and the inclination range is rather wide. So we select in a next step some useful sampling of the scenario space by trial scenarios.

2.3 Basic Scenario Setup

We selected 21 single-orbit baseline cases for further evaluation. Common for all of them is that they use only one orbital plane (O=1) for the different satellite configurations. This single orbit plane contains 1, 3, or 6 satellites (S$\epsilon\{1, 3, 6\}$), and the inclination varies, in 7 (unequal) steps from an equatorial 0° to a sun-synchronous 98° orbit. A list of these basic scenarios is given for convenience by table 2.

The mean anomaly in-orbit spacing for the 3-satellite cases is 120°, for the 6-satellite cases it is 60°. These 21 baseline runs were necessary in order to get basic quantitative information and the possibility to define a reasonable sample of real scenario cases later on (see section 3).

2.4 Calculations of Baseline Scenarios

Next step in the evaluation of the 21 baseline scenarios is to calculate the tangent points of the straight-line GNSS-LEO rays with respect to the surface of the Earth. For this purpose, the EGOPS simulation tool was used (EGOPS is the End to end GNSS Occultation Performance Simulator, a software developed 1997-2000 under the leadership of IGAM/UoG for ESA). The MAnPl (Mission Analysis and Planning) tool of EGOPS is used for performing the simulations required here.

Before working with MAnPl under EGOPS, the so-called leo*.tle files for the LEO satellites have to be calculated (EGOPS uses standard NASA/NORAD two-line-element (tle) files, which contain all needed parameters for defining the satellite(s) orbit(s) (epoch of perigee, inclination, right ascension of ascending node, eccentricity, argument of the perigee, etc.). In the simplest case (only one satellite is orbiting, as in the first 7 cases) a *.tle file contains all necessary orbital parameter information in only two lines - therefore the name of these files. For calculation of leo*.tle files, EGOPS CreateTLEs routine was used for every different satellite constellation).

For the GNSS space segment of a satellite configuration, we took the standard gps*.tle and glo*.tle files contained in the EGOPS package (gps96213.tle and glo96213.tle, which contain full 24-satellite GPS/GLONASS standard constellations. This are later used after updating the internal time information for January 1987.

As stated before the EGOPS MAnPl tool is used for calculating simulated geometry data. These files contain beside other information the geographical coordinates of the tangent poinats of all occultation events within a simulated time range. For calculating those results, we need as EGOPS input parameters the UT Range, the Height Levels, the Geographic Area of Interest for the Occultation Events, the GNSS-LEO Ray Treatment, the Earth figure Model, the GRAS Antennae Specifications, and the LEO and the GNSS Specifications. A 12 hr simulation time was chosen from which a 6 hr time interval was cut out for data processing and analysis. Using a single Height Level was also sufficient for this kind of geographical coverage study. The orbital period of our chosen LEO satellites is near 100 min, the orbital period for the GNSS satellites is near 12 hrs; the orbit height is $\sim$ 20,000 km.

2.5 Analysis of Occultation Event Locations

With the tangent points obtained, we are now ready for statistical post-processing of these results to achieve better knowledge of the value of our basic satellite constellation scenario.

We chose to calculate the following 5 main statistical measures, which will also form the basis for a performance assessment of mission scenarios at a later stage:

- N $(= N_{occ}^{(\Delta T)}(A))$ $[1/(1000km)^2]$ is the total number of occultation events per unit area within a given sampling time (ΔT) in a given geographic area A.
- $\overline{d}$ $(= \overline{d}_{occ}^{(\Delta T)}(A))$ $[km]$ denotes the mean horizontal sampling distance between neighbor

occultation events within a given sampling time (ΔT) in a given geographic area A; $\overline{d} = \frac{1}{n_A}\sum_{i=1}^{n_A} d_i$, with n_A the number of events in $\{(\Delta T), A\}$.

- σ_d $(= \sigma_{docc}^{(\Delta T)}(A))$ $[km]$ is a sampling distance dispersion measure (rms deviation about mean) for given $\{(\Delta T), A\}$; $\sigma_d = \left[\frac{1}{n_A - 1}\sum_{i=1}^{n_A}\left(d_i - \overline{d}\right)^2\right]^{\frac{1}{2}}$.

- $\overline{t}$ $(= \overline{t}_{occ}^{(\Delta T)}(A))$ $[min]$ is the mean time separation between neighbor occultation events for given $\{(\Delta T), A\}$; $\overline{t} = \frac{1}{n_A}\sum_{i=1}^{n_A} t_i$.

- σ_t $(= \sigma_{tocc}^{(\Delta T)}(A))$ $[min]$ is the time separation dispersion measure for given $\{(\Delta T), A\}$; $\sigma_t = \left[\frac{1}{n_A - 1}\sum_{i=1}^{n_A}\left(t_i - \overline{t}\right)^2\right]^{\frac{1}{2}}$.

Furthermore, as global indices/single figures of merit, the following values were calculated as scalar quantities:

- $\sigma_N^{gl} = \left[\frac{1}{N_A - 1}\sum_{i=1}^{N_A}\left(N_i^A - N^{gl}\right)^2\right]^{\frac{1}{2}}$ & $\tilde{\sigma}_N^{gl} = \frac{\sigma_N^{gl}}{N^{gl}}$ represent the coverage inhomogeneity indices, i.e. global absolute & relative measures, respectively, of how (un)equally distributed the occultation events are in general (N_i^A is the number of events collected in region A, N_A is the number of areas).

- σ_d^{gl} & $\tilde{\sigma}_d^{gl} = \frac{\sigma_d^{gl}}{\overline{d}^{gl}}$ are the geographic irregularity indices, i.e. global absolute & relative measures, respectively, of how (ir)regularly the occultation events are distributed over geographic space.

- σ_t^{gl} & $\tilde{\sigma}_t^{gl} = \frac{\sigma_t^{gl}}{\overline{t}^{gl}}$ are the time irregularity indices, i.e. global absolute & relative measures, respectively, of how (ir)regularly the occultation events are ordered in time.

The two further external parameters required to be set for the analysis are $\{(\Delta T), A\}$:

As noted earlier a (ΔT) of 6 hrs was used, which is the upper bound of the time sampling requirement specifications according to table 1). We confirmed for our post-processing computations that the results are virtually invariant with respect to the specific choice of the 6-hr window within the basic 12-hr interval available from the basic tangent point location processing by EGOPS. All result shown were taken from the center of the 12 hrs time interval.

For better regional analysis of our data several different areas A were used . We computed the required statistical measures for the whole Earth. For all other values we limited the computations, because of computational speed, to the northern hemisphere or subregions of it. This is no real restriction at all, we just exploit the perfect north-south symmetry inherent in circular satellite orbits. This symmetry is indeed only broken to an irrelevant degree, as we confirmed for all measures by computing a hemispheric asymmetry factor (see further below). It is slightly broken only given that the total time span is not an integer multiple of the orbit period.

So we analyzed the following 49 different sub-global areas:

- Northern Hemisphere (NH).
- 6 Latitude Bands $\epsilon\{0° - 15°, 15° - 30°, 30° - 45°, 45° - 60°, 60° - 75°, 75° - 90°\}$ in NH.
- 6 Longitude Bands $\epsilon\{0° - 60°, 60° - 120°, 120° - 180°, 180° - 240°, 240° - 300°, 300° - 360°\}$ in NH.
- 6 x 6 Cells $\epsilon\{$the 36 15° x 60° LatLon cells from using the above bands$\}$ in NH.

All five statistical measures and the three global indices, plus a hemispheric asymmetry factor were calculated for all chosen areas. Thus, for example, the latitude averages for one measure are not just averaged results from the individual cell values making up this latitude band. This is important, since such operation were wrong given that there is no superposition principle valid in this context.

As first step in the computation process the size of the individual areas was determined by integrating over the respective spherical surface. This provides us with 50 different values, beginning from the area of the whole planet (about 510 x $10^6 km^2$) to the area of the smallest pieces (the 6 circumpolar cells $\geq 75°$). Using this for normalization and counting the number of events, i.e. tangent points which happen to fall into a given area, the computation of N is straightforward.

For computation of $\overline{d}$ and σ_d, respectively, it was necessary for having a robust general algorithm to proceed as follows: We need to calculate the average distance d_i from each tangent point location to its neighbor tangent points. This was accomplished by dividing the surrounding of the tangent point into 4 equal azimuth ranges (a north-, west-, south-, and east range), then computing the distance to the closest neighbor in each azimuth sector and averaging over the four minimum distances found. This yields, after performing for all events in an area, all d_i values. The calculation of $\overline{d}$ and σ_d is then straightforward based on the formulae given above.

With this method one obtains good results even in sparse-event situations, where more straightforward methods fail due to difficulties to deal with small event numbers in a given area.

The same method was chosen for the computation of $\overline{t}$ and σ_t, respectively, as it is obvious that time separations between neighbor events, t_i, can be handled in close link to the computation of the distances d_i. After the four closest neighbors are found as outlined above we take the times when these events occurred and average them to obtain t_i. Having these values the computation of $\overline{t}$ and σ_t is done based on the respective formulae above.

It should be noted that tight clouds of tangent point locations over a given area do not imply that they are also closely packed in time. This is due to the somewhat intricate way in which GNSS occultation events are sampled.

After preparing the 5 measures for all defined areas, the 6 global indices (σ_N^{gl}, $\tilde{\sigma}_N^{gl}$; σ_d^{gl}, $\tilde{\sigma}_d^{gl}$; σ_t^{gl}, $\tilde{\sigma}_t^{gl}$) were calculated.

2.6 The Format and Structure of all Result Plots

For optimum visualization of the results we used a concept comprising two panels per page with a 7 x 7 cell arrangement per panel. We give here a short description on how to understand the plots. Since all plot panels shown have a common structure, we provide this description just on this single place here for both the baseline scenarios following below and for the realistic scenarios following in section 3. We will explain the plot panel contents from top to bottom of panel.

At the top of each plot panel there are two header lines. The first line contains at its first position the name of the plot parameter (i.e. statistical measure) displayed, together with its physical unit. The following abbreviations are used for describing the 5 measures:

- Event No N/$(1000km)^2$ $[Mm^2]$, for the occultation event number density per square mega meter.
- Mean HDist md [km], for the Mean Horizontal Distance between neighbor occultation events, measured in kilometers.
- HDistDisp sd [km], for the Horizontal Distance Dispersion (rms distance about mean), measured also in kilometers.
- MeanTSep mt [min], for the Mean Time Separation between neighbor occultation events, measured in minutes.
- TSepDisp st [min], for the Time Separation Dispersion (rms separation about mean), measured also in minutes.

If there is more than one different satellite scenario plotted (up to 4 are possible per panel, each visualized by a histogram bar), the measure displayed for the different scenarios is of course one and the same for all scenarios.

The next three groups of acronyms in the first line give the main satellite constellation information. Beginning with the left one, O is the number of orbital planes used (O can be 1, 2 or 4 in our case), S is the number of individual satellites per orbital plane (S can be 1, 3, or 6 for symmetrical scenarios or 2, 4 or 8 for asymmetrical scenarios; see details on that in the description of the realistic scenarios), and I denotes the inclination of the orbital planes (I can be 00, 30, 60, 70, 80, 90 or 98 degrees). In case more than one scenario is plotted (we generally plotted, in order to save trees, 3 or 4 scenarios per panel), the individual values for O, S, and I, respectively, of the specific scenarios shown are separated by vertical lines for better recognition of the respective values (the leftmost value is associated with the leftmost histogram bars plotted in each of the 7 x 7 cells, the second-left value with the second-left histogram bars, and so on). In case more than one plane is involved (O greater than 1) the values for S and I comprise the information on the number of satellites in a plane and on the inclination of a plane, respectively, for all planes. For example, if O=2 (2 orbit planes), then S=42 and I=8030 if the first plane holds 4 satellites at 80 ° inclination and the second plane holds 2 satellites at 30 ° inclination. If the plot panel shows three different scenarios, typically

different due to trying different inclinations, this may look like O=2—2—2, S=42—42—42, I=8030—8055—9830 (i.e., the number of orbits and the distribution of satellites into the orbit is the same for all three scenarios, but the orbit inclination are varied).

The second header line shows, for the plotted measure, the two global indices defined above in section 2.4 (the absolute and relative global irregularity measures sX^{gl} and rsX^{gl}, respectively, with X denoting one of the 5 measures). This provides quantitative information, which supplements the displayed information in form of giving single figures of merit for the global behavior of the results presented. The second line also gives the value of the hemispheric asymmetry factor ($DX^{hem/gl}$, with X denoting one of the 5 measures) in order to routinely see how well the NH represents the globe. In full analogy to the first header line, the values corresponding to the different scenarios shown are separated by bars.

The actual results for a given statistical measure are visualized as histogram bars in a 7 x 7 cell arrangement, where the 36 single cell results (60 ° longitude cells x 15 ° latitude cells) are plotted in a 6 x 6 cell structure, the longitude band results in a 1 x 6 cell structure beneath the 6 x 6 cells, the latitude band results in a 1 x 6 cell structure to the right of the 6 x6 cells, and the total NH (northern hemisphere) results in the lower-right cell, respectively. While we fixed the size of the cells we left the ordinate axis scale adjustable to best fit the magnitude of values of any given measure (for enforcing clarity, this scale is only adjustable for all 49 cells together).

As mentioned earlier, each grid cell can contain from 1 to 4 histogram bars, representing results of 1 to 4 different mission scenarios. Note that, basically, the scenarios can be different in the number of orbital planes, their respective satellite numbers per plane, and in the inclinations (this will be visible from the first header line), but also in other parameters like right ascension of node, mean anomalies, etc. (which is not made visible but needs to be logged externally and mentioned in the caption/plot explanation as appropriate). For enhancing the quantitative information content of the plot, each histogram bar is tagged with its corresponding numerical value.

2.7 General Figure Structure of Baseline Scenario Results

The following figure structure description for the baseline results serves also as an indicator for the structure of the realistic scenario figures following further below.

The figures are regularly arranged in groups of 5 figure sheets (each sheet includes two separate plot panels), whereby each individual figure of the group shows one of the five statistical measures. The first sheet of such a group contains always the occultation event number density N, the second the mean distance md, the third the distance dispersion sd, the fourth the mean time separation mt, and the fifth time separation dispersion st, respectively.

Each individual figure visualizes the results of 7 (in some real scenario cases 6) scenarios for one statistical measure.

Common to those 7 (or 6) different satellite constellation scenarios is always the number of orbital planes (O) and the numbers of LEO satellites per orbit (S). The main difference is

in the different inclinations (I) of the orbital planes. For example, for all baseline scenarios (figures 4.1 to 4.15), I starts with an inclination of 0 ° for the leftmost histogram bars in the upper plot panel and ends with an inclination of 98 ° for rightmost histogram bars in the lower plot panel, the results in between corresponding to inclinations of 30, 60, and 70 degrees (upper panel) and of 80 and 90 degrees (lower panel). This can be directly seen from the first header line of the panels as explained in section 2.6 above.

The partitioning into separate packages of 7 (or 6) mission scenarios (visualized by one specific 5 figure group in all 5 measures) has been performed considering the following three main criteria:

- Different orbital planes (used for the real scenarios, chapter 3).
- Varying satellite numbers per orbital plane (used for the baseline scenarios and for the real scenarios).
- Maximum or minimum orbital plane (orbital node) separation, $\Delta\Omega$, relevant for drifting (i.e. non-sun sync) orbits where this separation continuously, and periodically, changes over time used for scenarios with planes that have different inclinations. For scenarios with different orbital planes but identical inclinations as purely sun-synchronous constellations orthogonal separation is used as a single case, since here no different orbit plane precession takes place because we have chosen circular orbits with all orbits at the same orbital heights.

Involving the insights gained from the results for the baseline scenarios presented below in section 2.8 we will then proceed to create a more realistic sample of satellite scenarios (which we call real or realistic scenarios), the results of which are presented in chapter 3.

2.8 Results of Mission Scenario Calculations

Figures 1 - 5 contain the results for the mission scenario calculations (table 2). For these simplest of our scenarios we assumed only one orbit plane with only LEO satellite. This serves as a reference scenario for true constellations.

Figure 1 shows that the number of occultation events is very unevenly distributed over the globe, with a maximum event number density reached of 3.5 [Mm^{-2}]. As expected, scenarios with low inclination give better densities near the equator, while constellations with higher inclined orbits have a better spreading of the occultation events. It is very obvious that these one satellite scenarios are certainly far from reaching the requirements given in table 1.

Figures 2 and 3 extend the results of figure 1. Large fluctuations of the mean distance and the mean horizontal distance dispersion can be seen everywhere in these two pictures.

For figures 4 and 5 the situation is about the same. The mean time separation and the time separation dispersion are varying from neighbor events occurring nearly simultaneously to time differences of nearly 3 hours between them (2 hours for the dispersion).

A primary reason for this irregularity is certainly that a single orbit plane allows to cover only about half of the globe with occultation events.

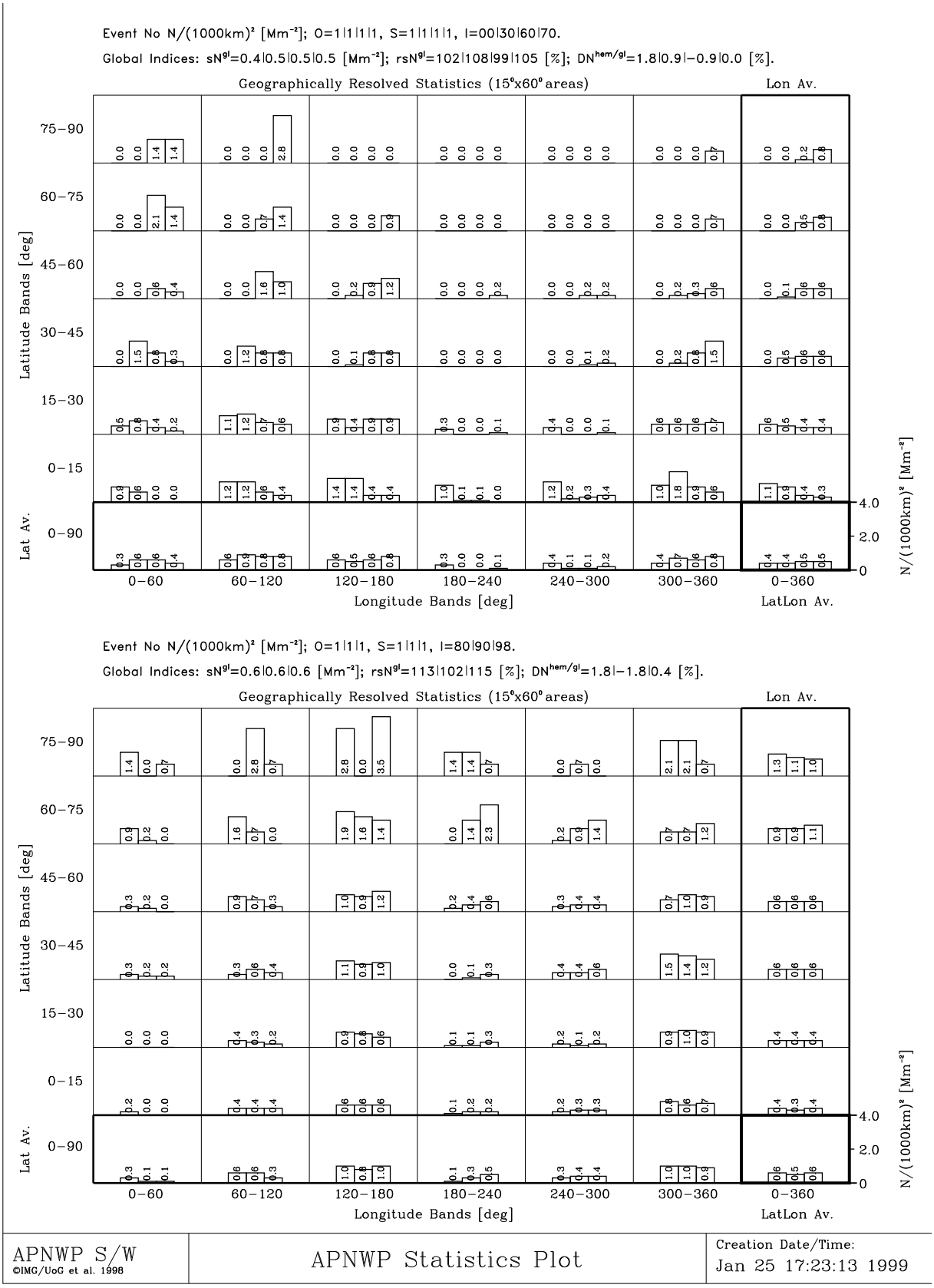

Figure 1: Occultation event number densities $N/(1000km)^2$ $[Mm^{-2}]$.

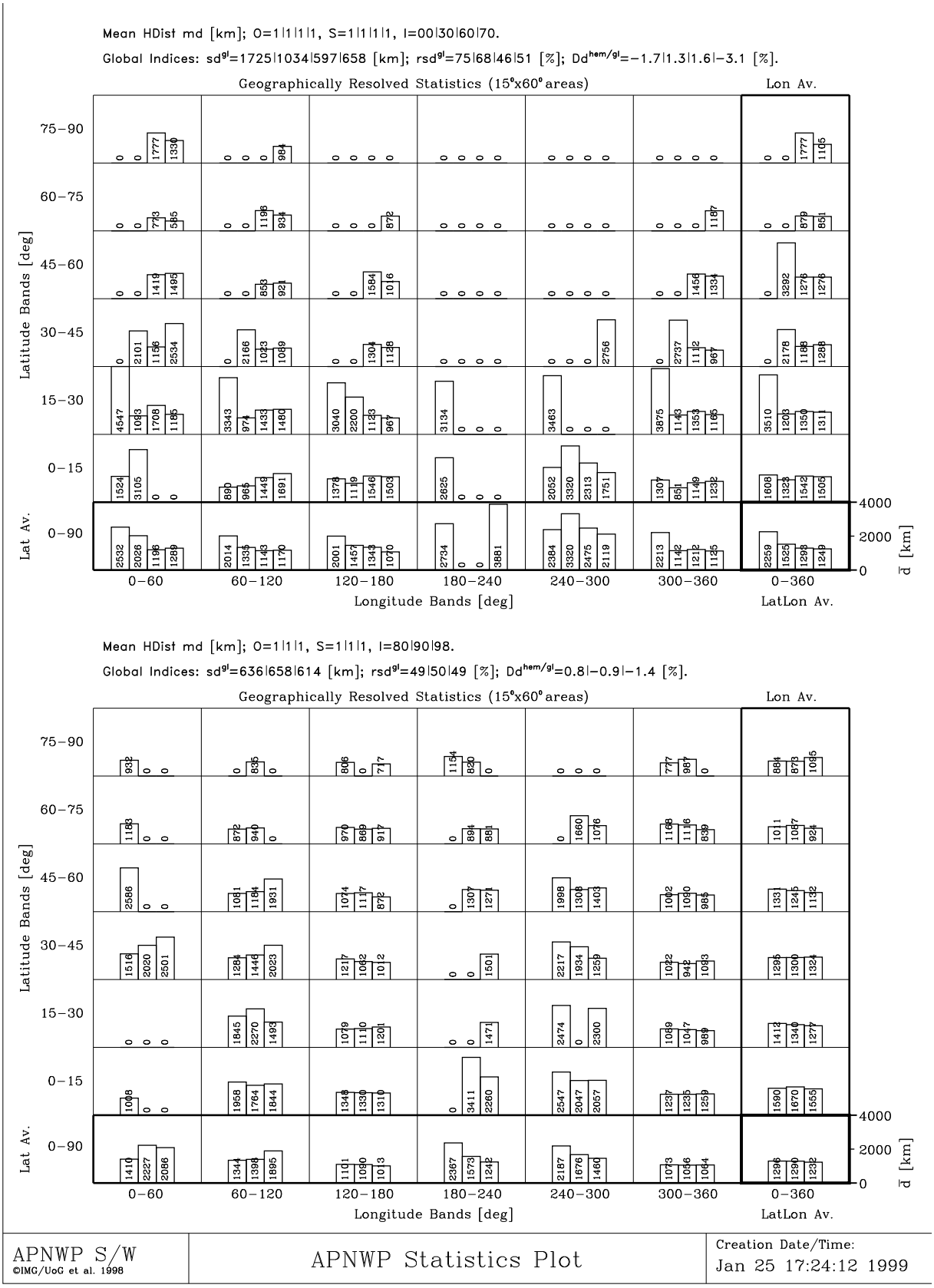

Figure 2: Mean horizontal distances $\overline{d}$ $[km]$.

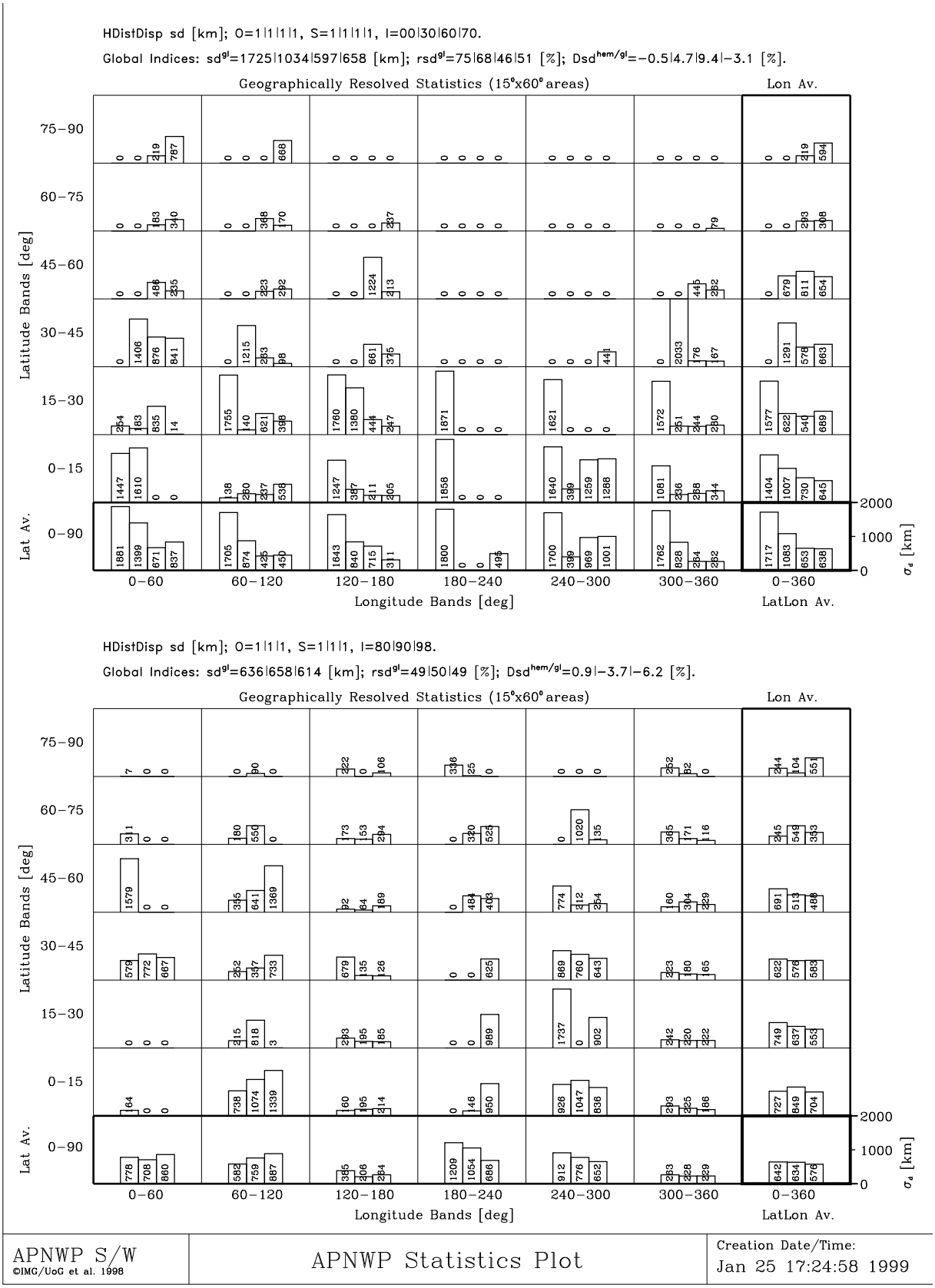

Figure 3: Horizontal distance dispersion σ_d $[km]$.

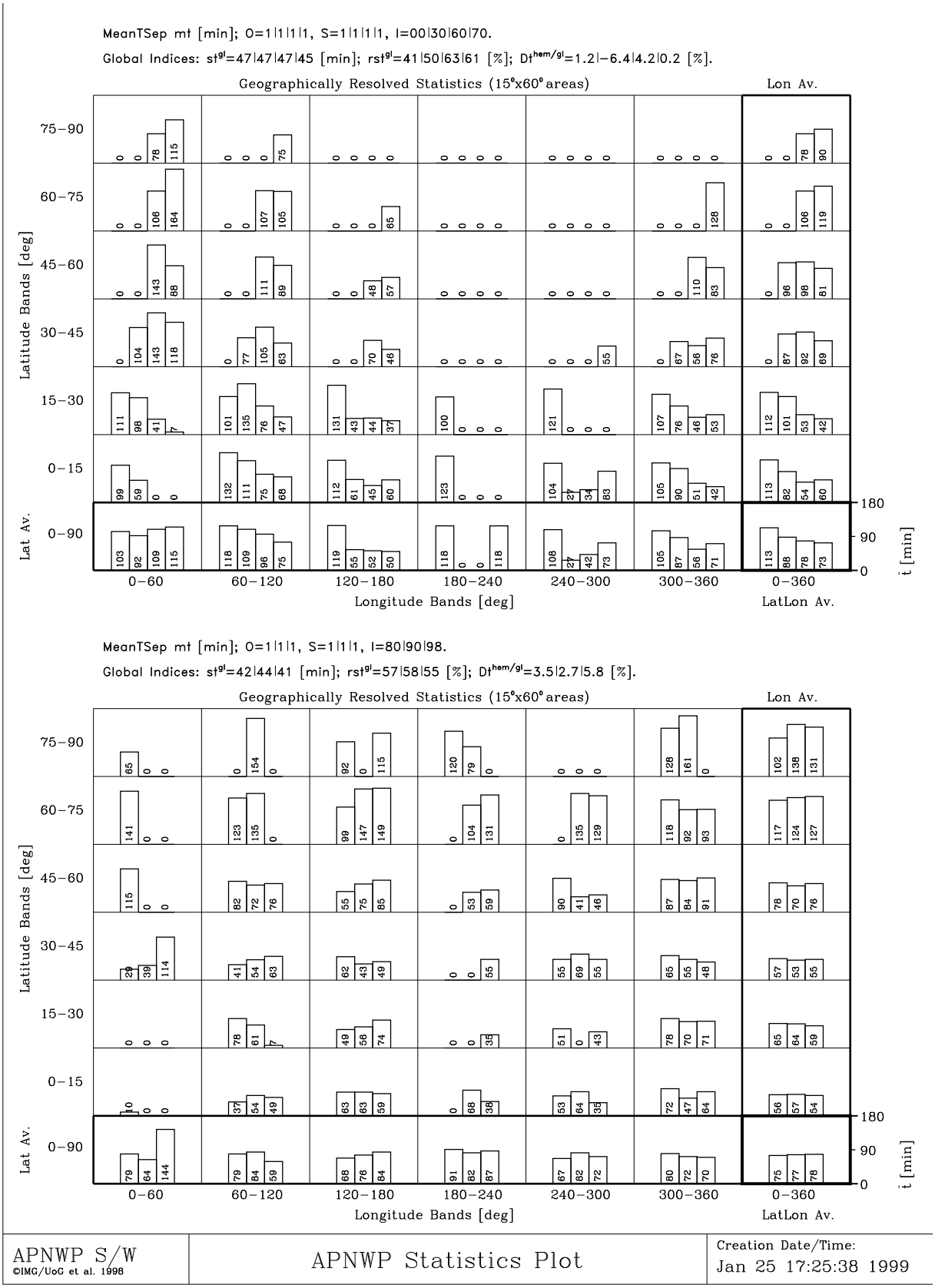

Figure 4: Mean time separation $\bar{t}$ $[min]$.

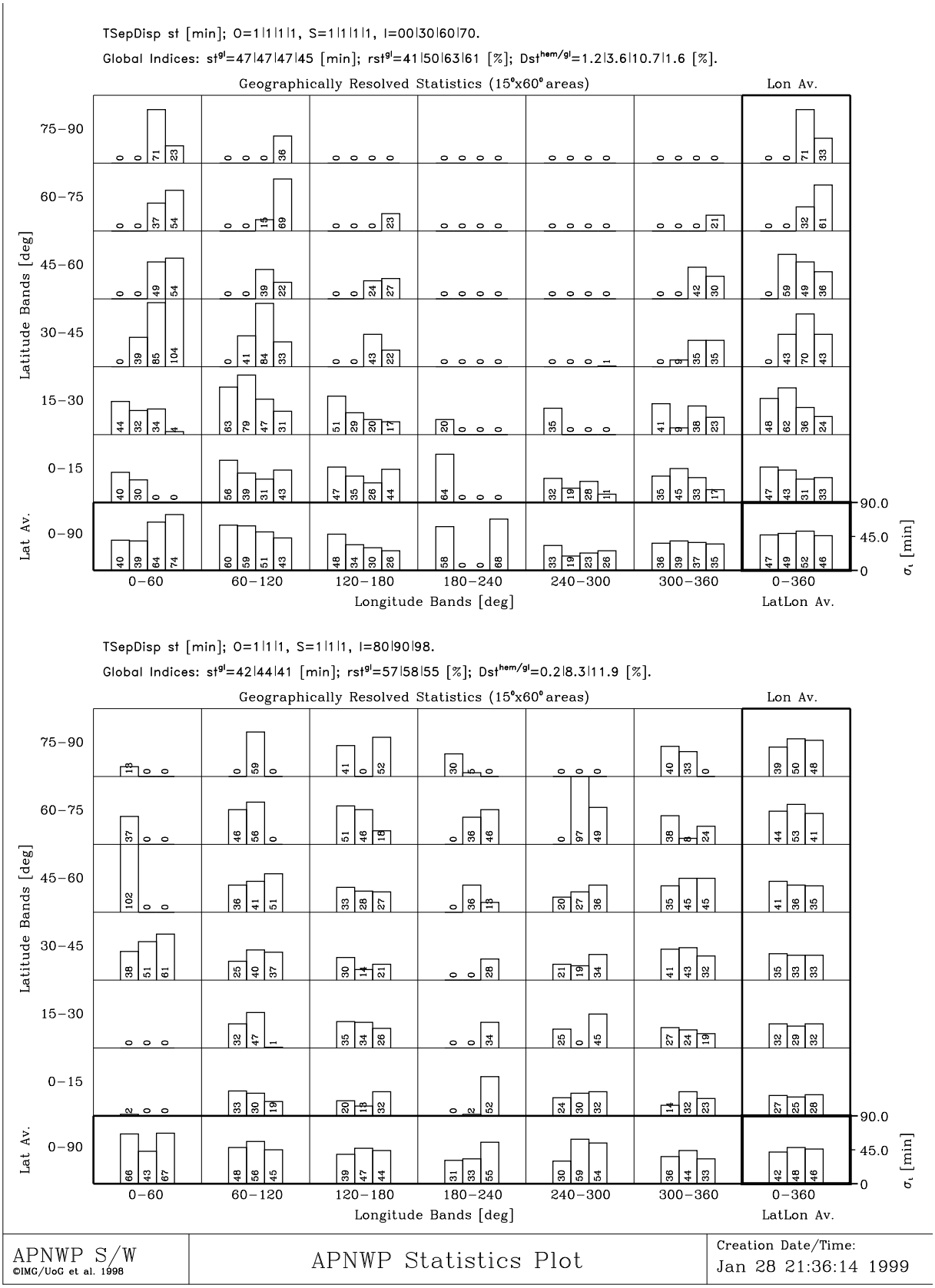

Figure 5: Time separation dispersion σ_t $[min]$.

Figures 6 - 10 contain the results for the middle column of the basic satellite scenario table shown in section 2.3 (table 2). We still deliberately assume only one orbit plane and again have the 7 scenarios differing by inclination, but here we use 3 satellites instead of one. According to our weak constraints baselined in section 2.2, the 3 satellites are equally spaced by 120 ∘ in the orbit.

A quick look at figure 6 shows that the number of occultation events is still very unevenly distributed over the globe (we still have one orbital plane only which does not allow to cover the full globe within 6 hours), the maximum number density now reaches 5.5 [Mm^{-2}]. As expected, scenarios with low inclination give better densities near the equator, while constellations with higher inclined orbits have a better spreading of the occultation events. In comparison to figure 1 it is obvious that average occultation event density has increased as should be natural for this 3 satellite constellation. Nevertheless this scenario is of course also very far away from fulfilling the requirements set out in table 1.

Figures 7 and 8 extend the results of figure 6. Large fluctuations of the mean distance and the mean horizontal distance dispersion can be seen everywhere in these two pictures. The mean distances are clearly shrinking, however, if one compares the results of figure 7 with figure 2.

Figures 9 and 10 express the same qualitative picture as their predecessors, figures 4 and 5. The mean time separation and the time separation dispersion are varying from neighbor events occurring only a few minutes apart to time differences of nearly 3 hours (2 hours for the dispersion). In general, however, the 3 satellite constellation already leads to a somewhat smoother time separation (and time dispersion) relative to the single-satellite case.

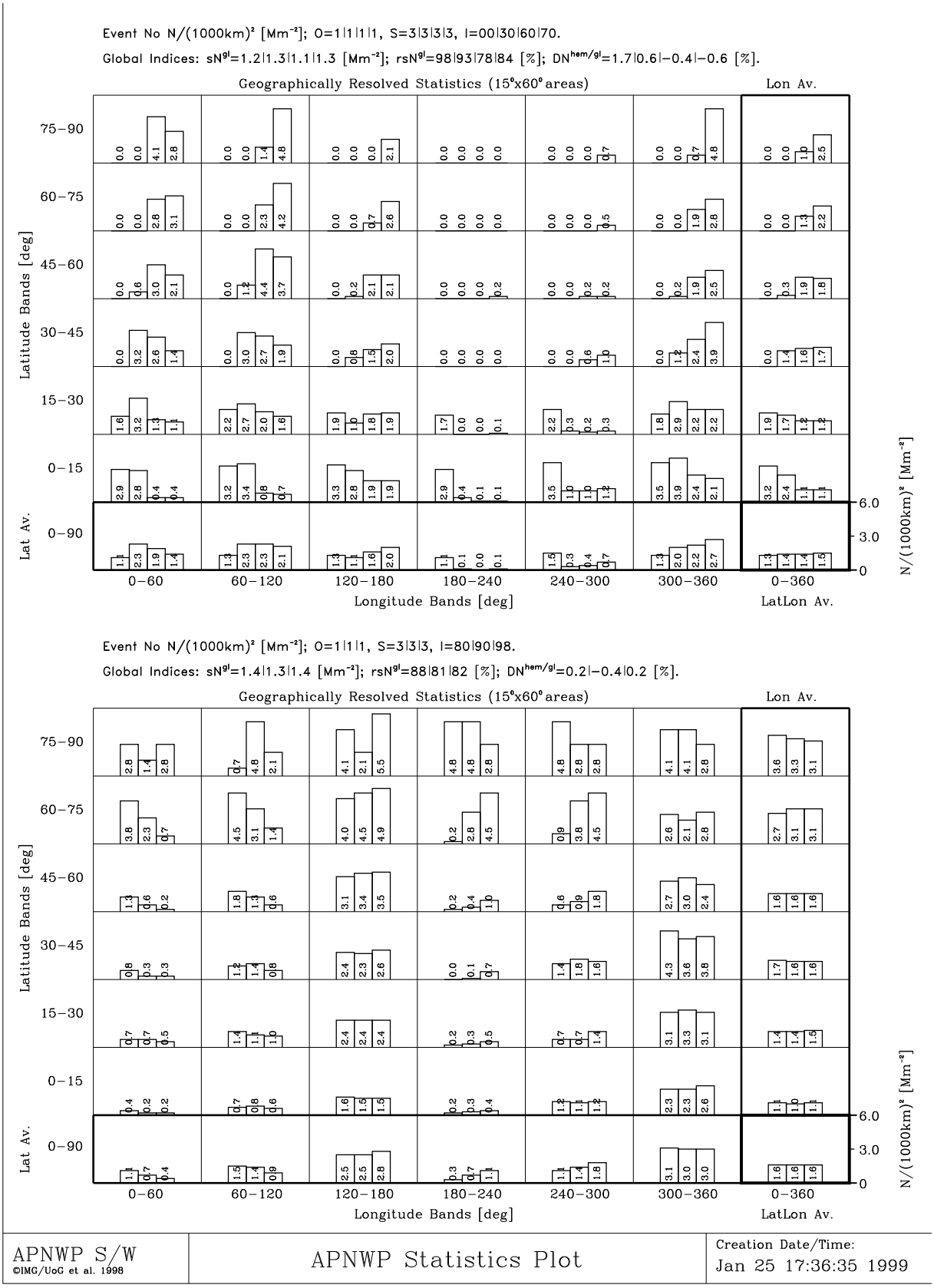

Figure 6: Occultation event number densities $N/(1000km)^2$ $[Mm^{-2}]$.

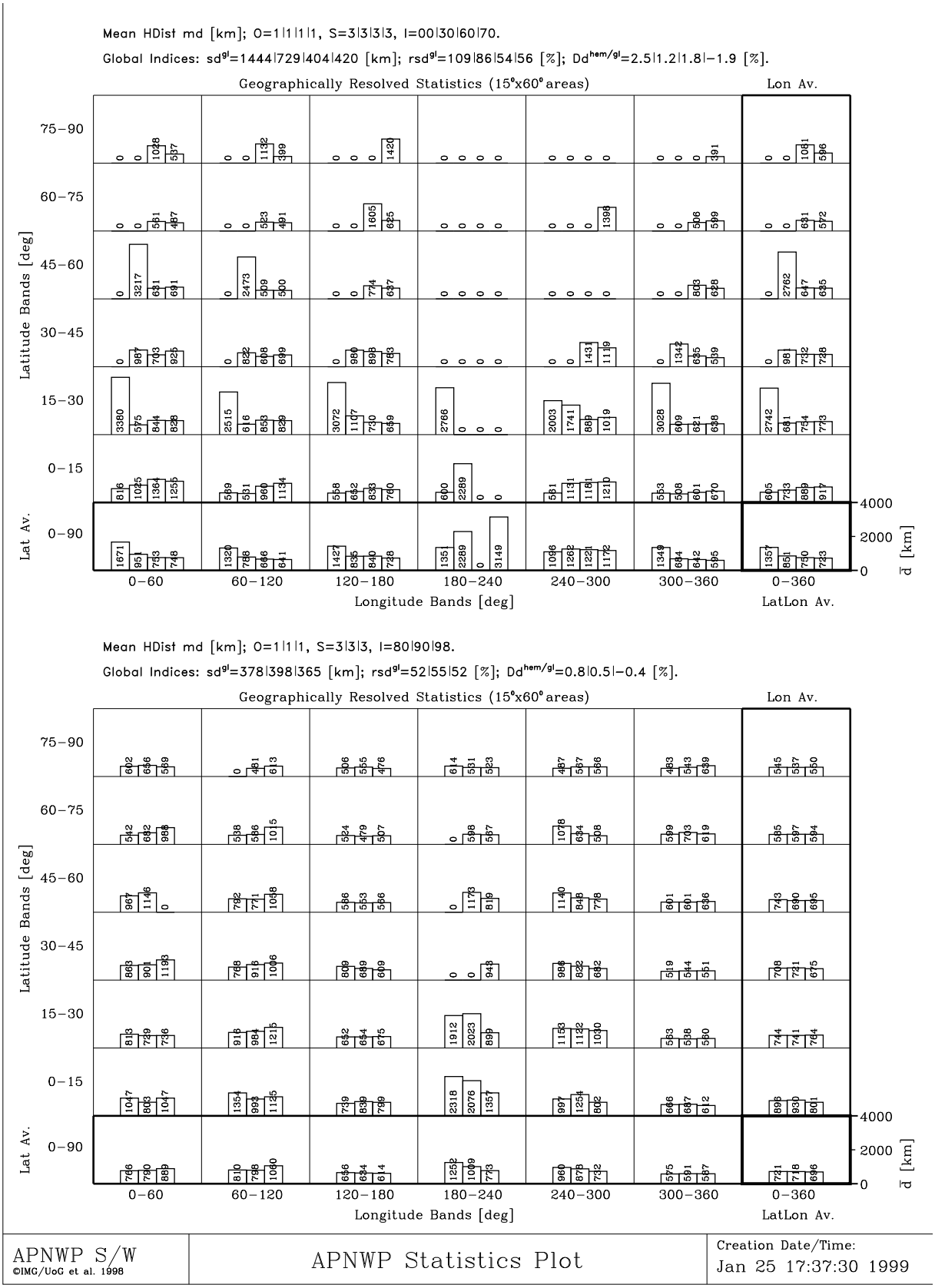

Figure 7: Mean horizontal distances $\overline{d}$ $[km]$.

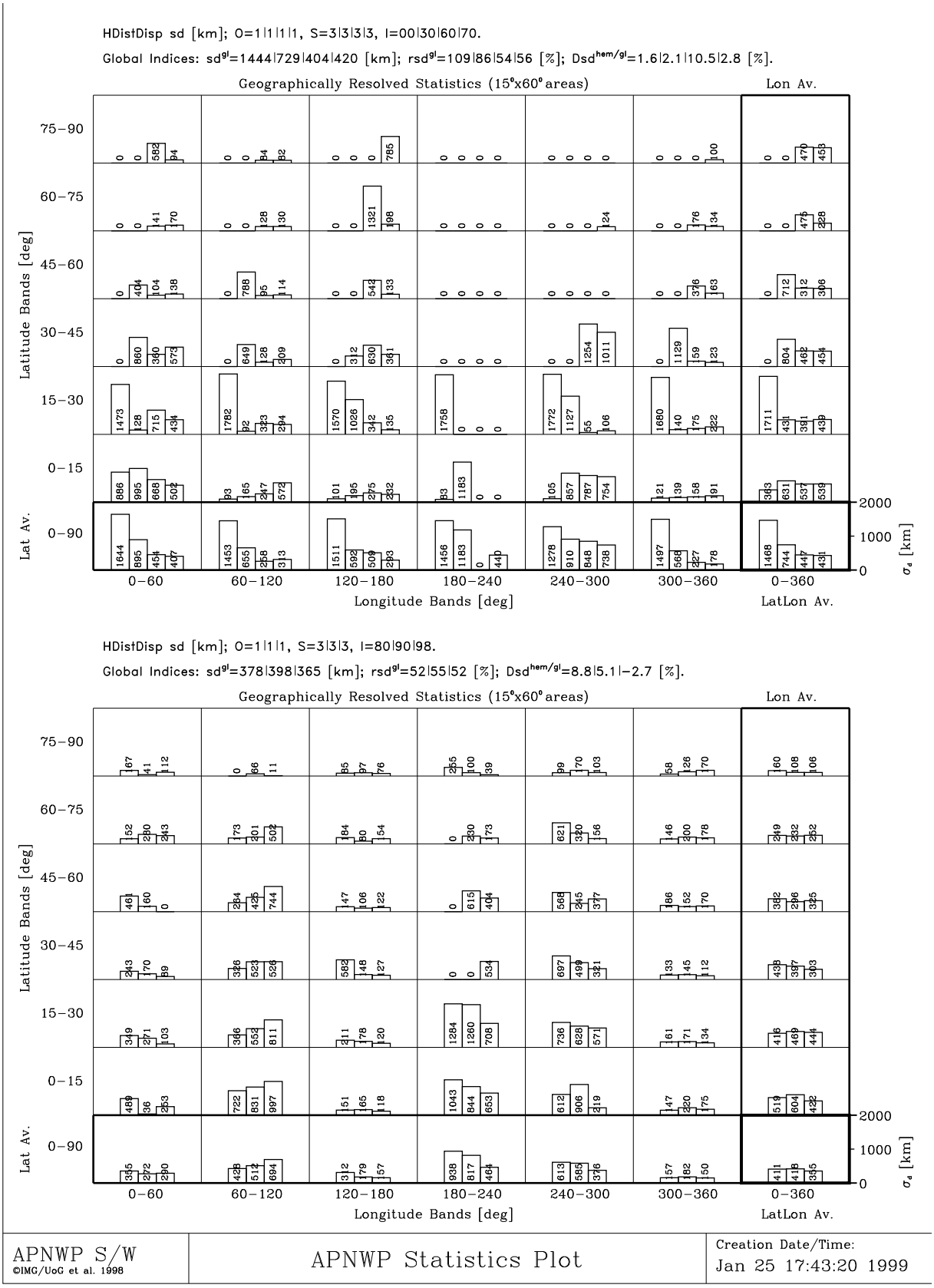

Figure 8: Horizontal distance dispersion σ_d $[km]$.

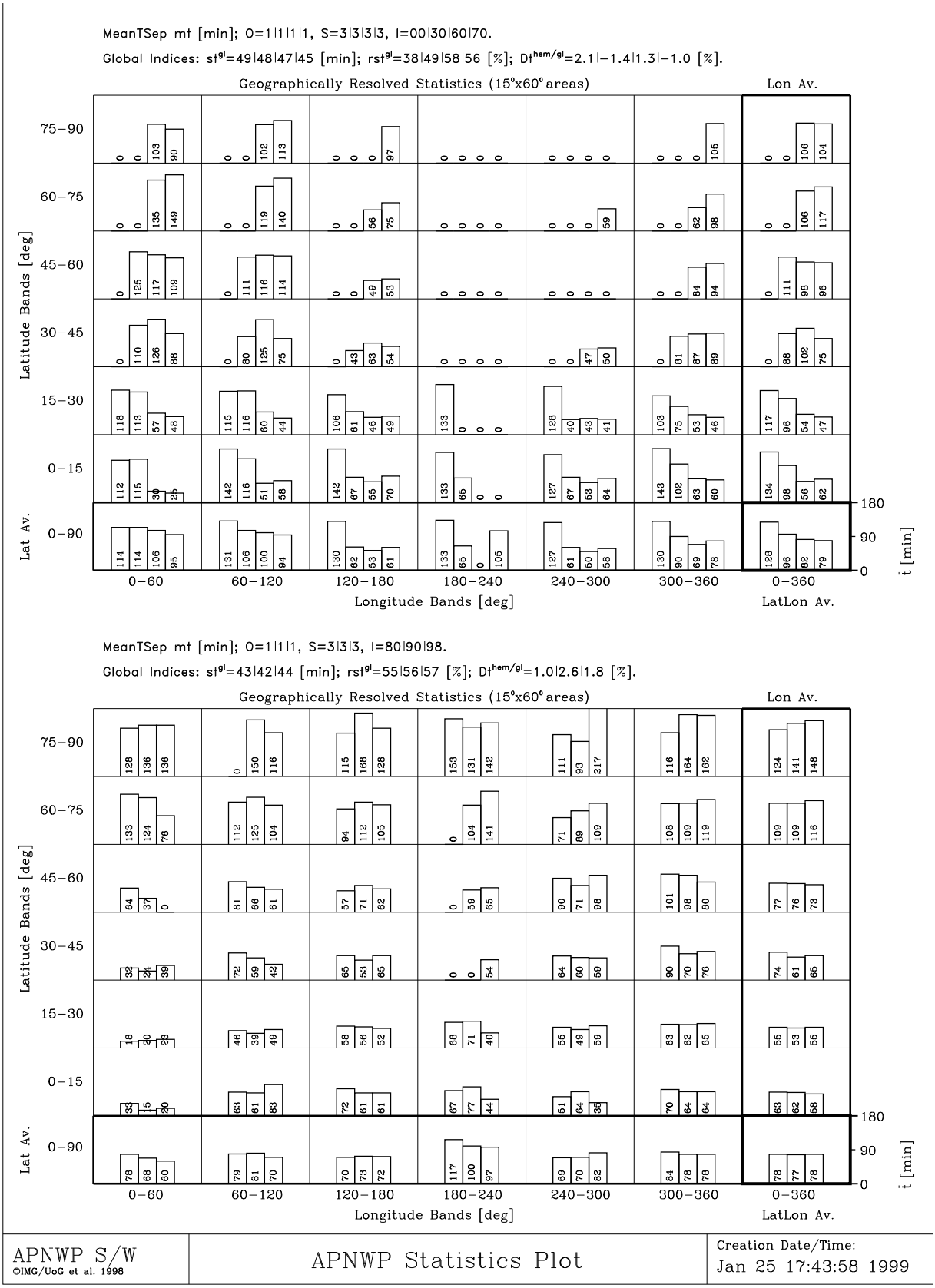

Figure 9: Mean time separation $\bar{t}$ $[min]$.

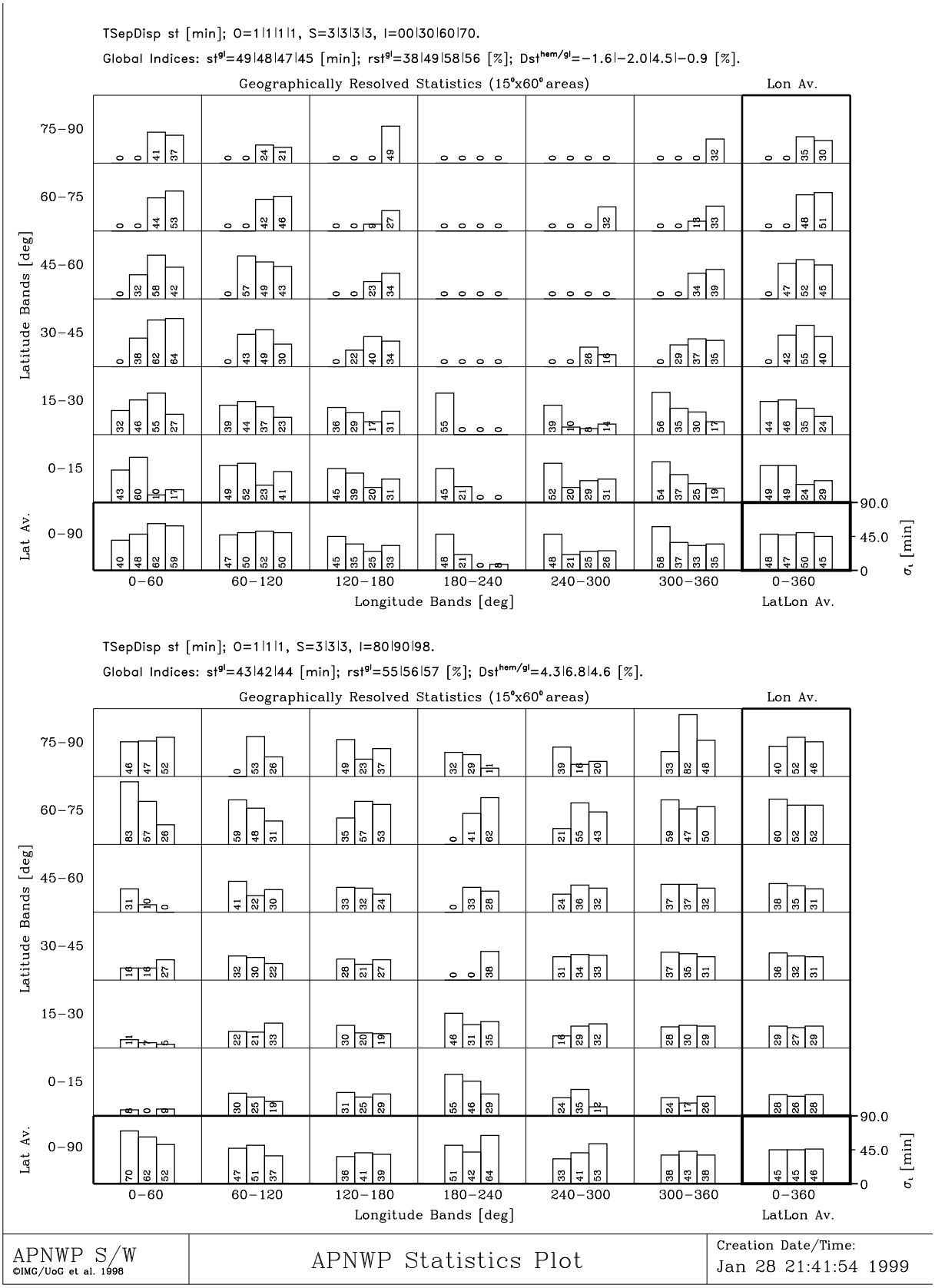

Figure 10: Time separation dispersion σ_t $[min]$.

Figures 11 - 15 contain the full set of results for the right hand column of the basic satellite scenario table shown in section 2.3 (table 2). Though we still deliberately assume only one orbit plane and again have the 7 scenarios differing by inclination, we now check the situation for 6 satellites instead of one or three as before. According to our weak constraints baselined in section 2.2, the 6 satellites are equi-spaced by 60 $\circ$ in the orbit.

A quick look at figure 11 demonstrates that the number of occultation events is, not surprisingly, still very unevenly distributed over the globe. The maximum density has reached now nearly 12 [Mm^{-2}], however. As still well visible, scenarios with low inclination give better densities near the equator, while constellations with higher inclined orbits have a better spreading of the occultation events. As a rough statement one can say that these 6-satellite scenarios are looking promising in several viewed areas but on the other hand there are still large gaps to fill for a more even distribution of occultation events.

Figures 12 and 13 extend the results of figure 11. There are still, in several regions, large fluctuations of the mean distance and the mean horizontal distance dispersion, on the other hand also more smooth areas are now definitely appearing at different places.

The situation for figures 14 and 15 is basically still comparable with that of the predecessors figures (figure 9 and figure 10). However, the mean time separation and the time separation dispersion are now again more smoothly distributed, especially moderate changes in inclination do not change too much. Nevertheless the average time separation and time separation dispersion values are in the still in the same range of magnitude as their predecessors.

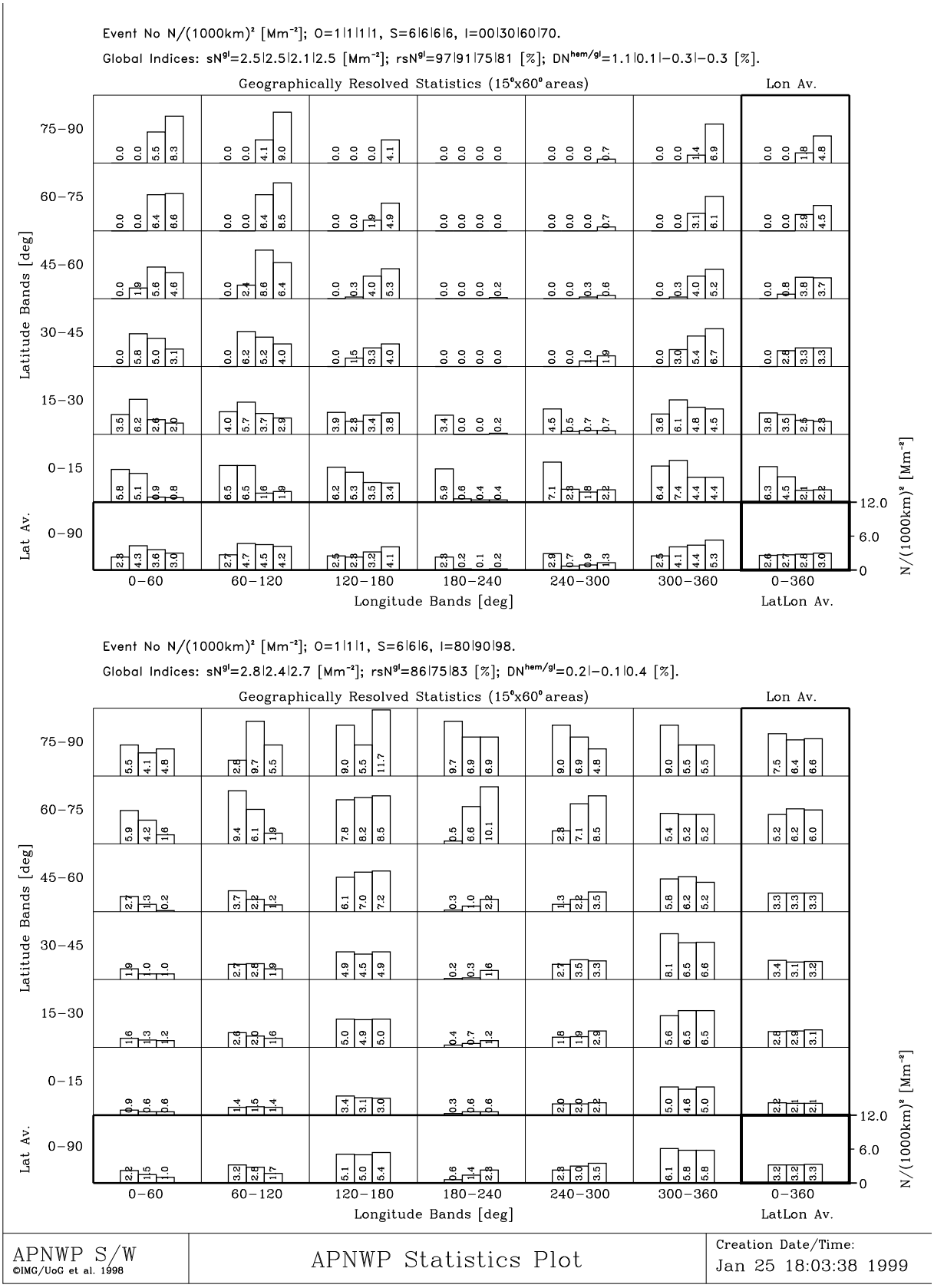

Figure 11: Occultation event number densities $N/(1000km)^2$ $[Mm^{-2}]$.

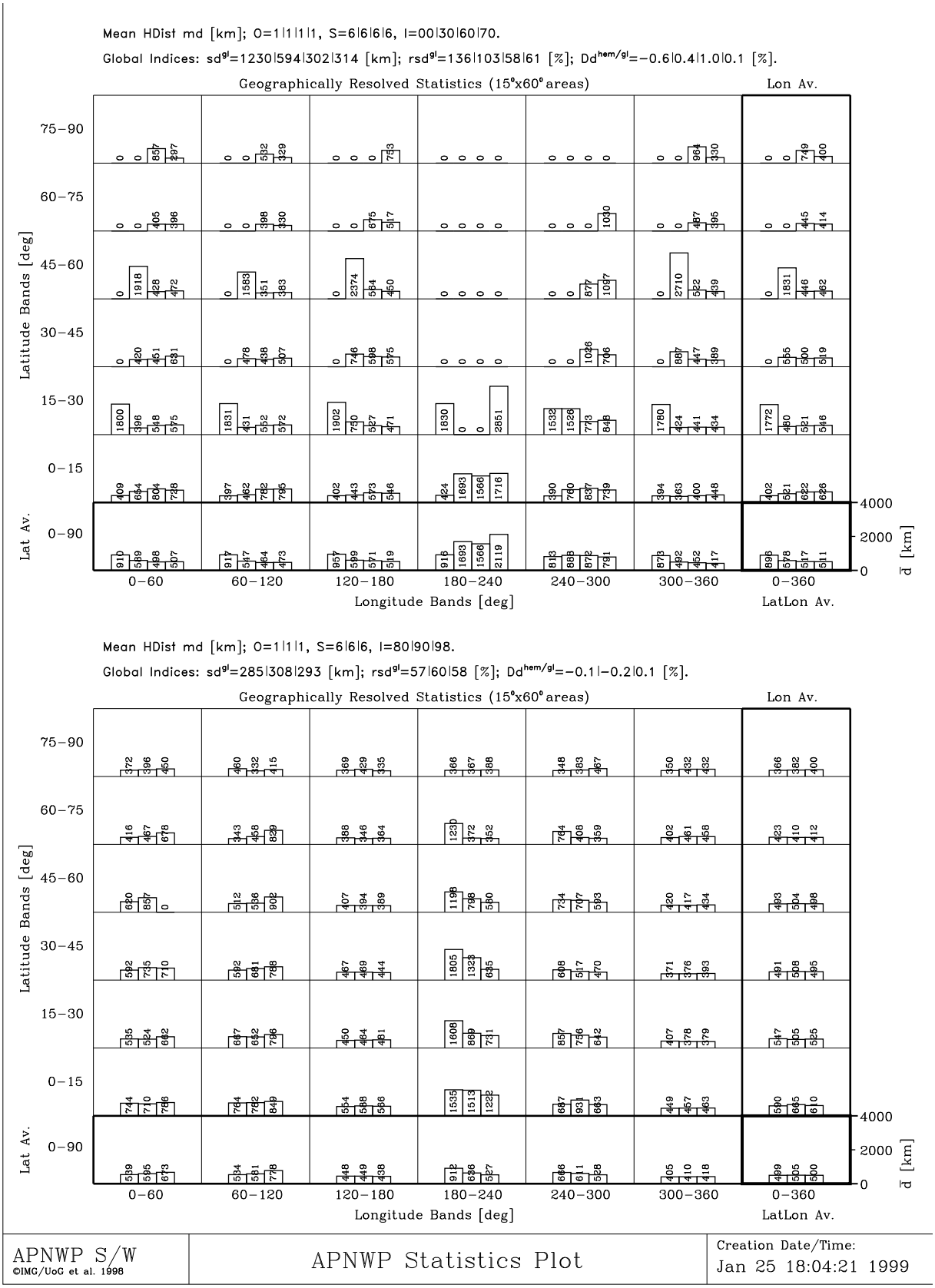

Figure 12: Mean horizontal distances $\overline{d}$ $[km]$.

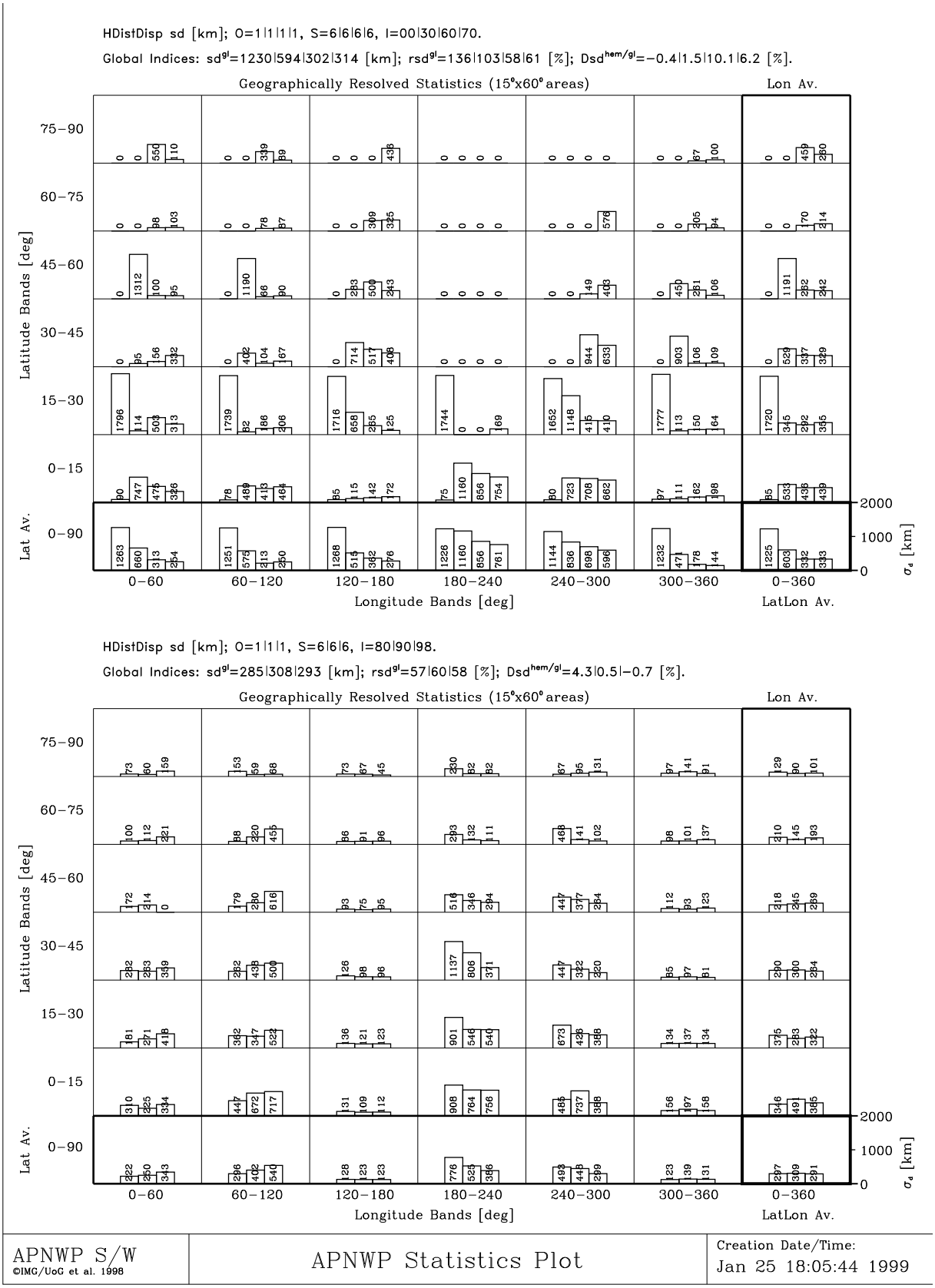

Figure 13: Horizontal distance dispersion σ_d $[km]$.

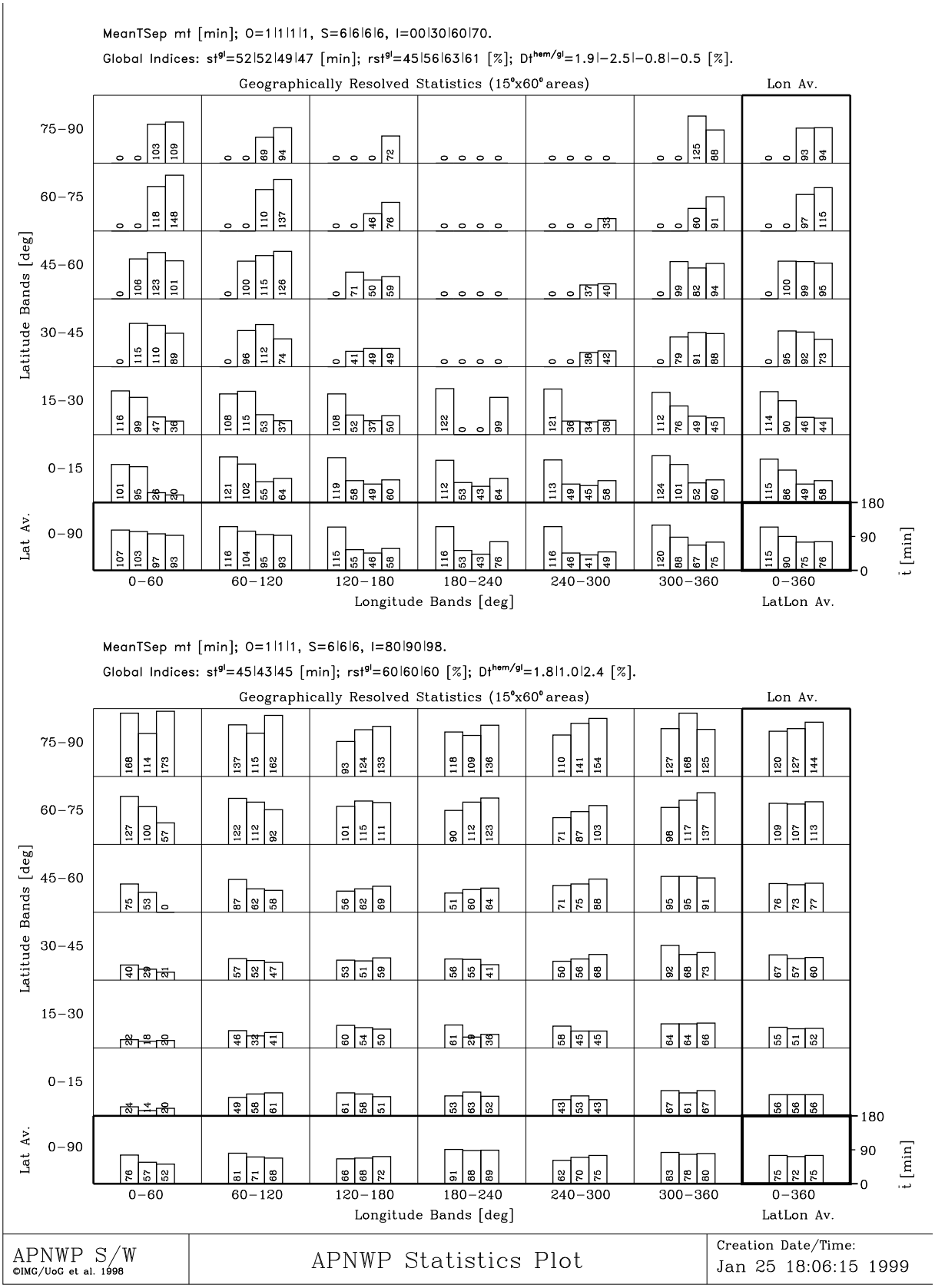

Figure 14: Mean time separation $\overline{t}$ $[min]$.

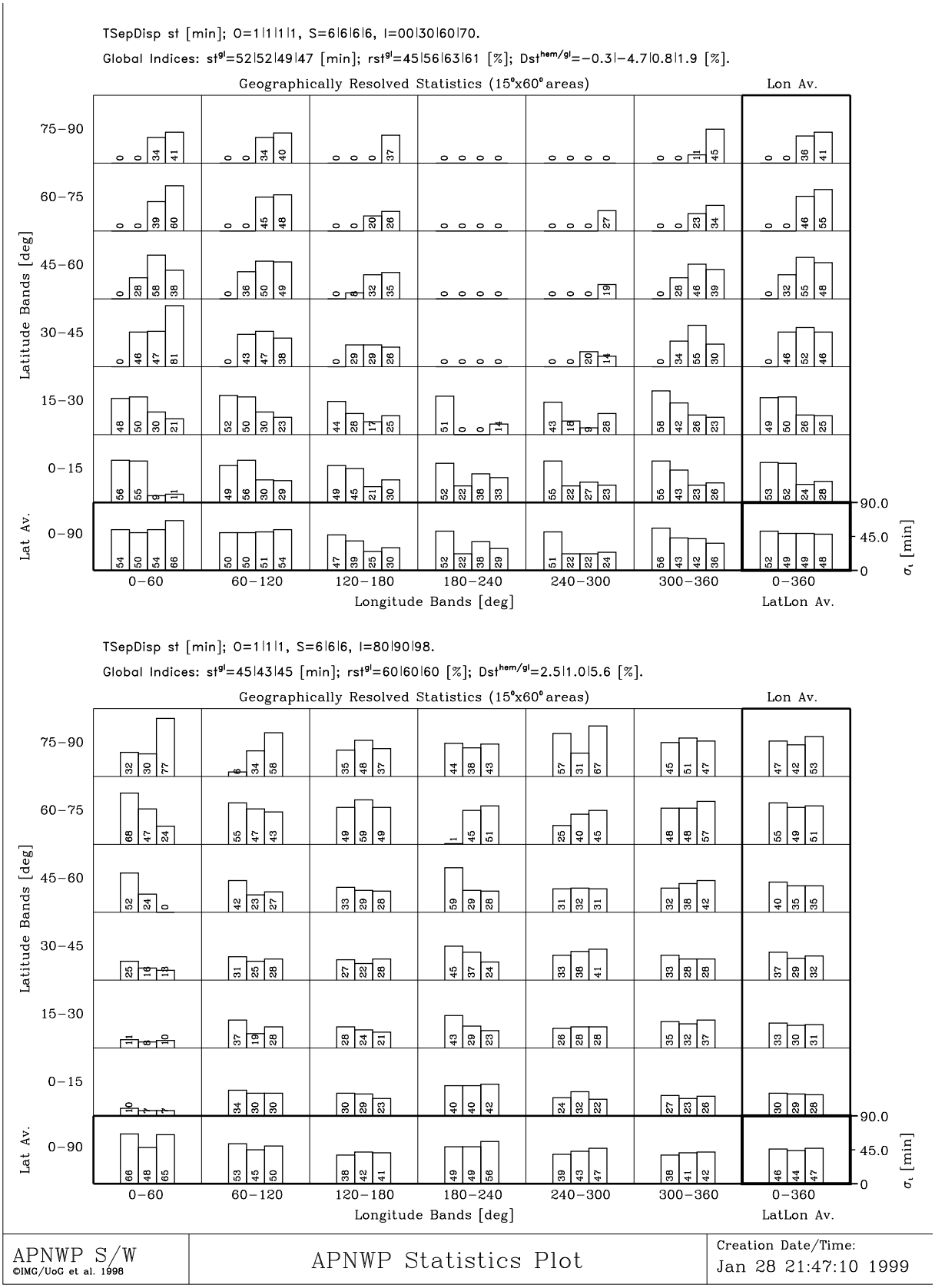

Figure 15: Time separation dispersion σ_t $[min]$.

3 Creating of Realistic Scenarios

After analyzing the different aspects of the basic scenario results, it is clear that more advanced constellations are necessary to head towards a reasonable fulfillment of the requirements for operational meteorology and other needs like climate monitoring. One has to form more advanced mission scenarios without loosing contact to the more practical determinants like system and operating costs, development time, availability of suitable launching services and so on.

One of the primary disadvantages of the single-plane baseline scenarios studied is certainly their very uneven geographical coverage. The best way to overcome this is by introducing a higher number of orbit planes. Thus we use, for realistic scenarios, a minimum number of two orbit planes (O=2), but we analyze also scenarios with four orbit planes (O=4), the latter for larger constellations.

We basically place the planes as symmetric as possible but as noted above nature destroys this favorite situation due to differential orbital drift given different plane inclinations. We decided to study in such cases, for one and the same constellation, both the best case (orthogonal nodes of the planes/maximal separation) and the worst case (aligned nodes of the planes/maximal overlap), respectively. This will give us an idea how the geometrical situation, and with it the statistical measures, are changing periodically in time while the constellation repeatedly undergoes its changes from node alignment to node orthogonality.

Also evident is that a larger satellite constellation can crucially improve the situation. Since we found 6 satellites already to be reasonable in terms of number of events we take, for the real scenarios, the size as the minimum constellation. To proceed further towards indeed be able to meet the requirements of table 1, we inspect, in addition larger constellations made of 12 and 24 satellites, respectively.

Clearly with these numbers of satellites, given that we also consider up to 4 planes, a lot of different configurations could be simulated. We limit the total number of realistic scenarios to a reasonable number by selecting a representative sample as defined below.

In terms of constellation size, we study sizes of 6, 12, and 24 satellites, respectively, as indicated above. In order to get a reasonable sampling going through different numbers of orbital planes and through different numbers of satellites per plane, we use 6 basically different satellite constellations types. 3 of these 6 cases are what we term symmetric configurations, namely for O=2 a S=3-3 (6 sat) and a S=6-6 (12 sat) satellite scenario, and for O=4 a 6-6-6-6 (24 sat) LEO constellation. For the other 3 constellation types, asymmetric configurations were designed, we used for O=2 a S=4-2 (6 sat) and a S=8-4 (12 sat) scenario, and for O=4 a 8-8-4-4 (24 sat) scenario. Such asymmetric orbit filling may be more favorable than a symmetric one: the analysis of the basic scenarios (section 2.8) showed that the more inclined orbits gave a much more even coverage (with a moderate maximum at high latitudes though), therefore most of the satellites should presumably be positioned in higher inclined orbits and fewer into lower inclined ones to optimize towards equal global coverage.

Concerning inclinations and the issue of drifting orbits requiring to look into node orthogonality vs. node alignment of orbit planes we decided to sample these dimensions of basin

O=2	O=2	O=4
$S\epsilon\{3-3, 4-2\}$	$S\epsilon\{6-6, 8-4\}$	$S\epsilon\{6-6-6-6, 8-8-4-4\}$
$I\epsilon\{98-98\}^*$ $\Delta\Omega$=90	$I\epsilon\{98-98\}^*$ $\Delta\Omega$=90	$I\epsilon\{98-98-98-98\}^*$ $\Delta\Omega$=45
$I\epsilon\{80-55\}$ $\Delta\Omega\epsilon\{90,0\}$	$I\epsilon\{80-55\}$ $\Delta\Omega\epsilon\{90,0\}$	$I\epsilon\{\underbrace{80-80}_{\Delta\Omega_h=90}-\underbrace{30-30}_{\Delta\Omega_l=90}\}$ $\Delta\Omega\epsilon\{45,0\}$
$I\epsilon\{80-30\}$ $\Delta\Omega\epsilon\{90,0\}$	$I\epsilon\{80-30\}$ $\Delta\Omega\epsilon\{90,0\}$	$I\epsilon\{\underbrace{98-98}_{\Delta\Omega_h=90}-\underbrace{30-30}_{\Delta\Omega_l=90}\}$ $\Delta\Omega\epsilon\{45,0\}$
$I\epsilon\{98-30\}$ $\Delta\Omega\epsilon\{90,0\}$	$I\epsilon\{98-30\}$ $\Delta\Omega\epsilon\{90,0\}$	$I\epsilon\{\underbrace{80-60-40-20}\}$ $\Delta\Omega\epsilon\{45,0\}$

Table 3: Real Satellite Constellation Scenarios

Notes:

* For pure sun-sync scenarios only symmetric satellite constellations were used.

space by 7 scenarios for each of the three symmetric configurations (including one purely sun-synchronous one) and by 6 scenarios for each of the asymmetric configurations (no purely sun-sync one).

Given this design we end up with 39 scenarios which involve 21 different constellations (the difference between the number of scenarios and of actual constellations derives from the running several scenarios for one and the same constellation to address the node alignment/node orthogonality issue).

With this design we assembled a fair set of promising candidates for heading towards the requirements of table 1 (actually fulfilling them, at least with the 24 sat constellations). For convenience, these 39 realistic scenarios are concisely summarized by table 5.1, the scenarios grouped there into columns representing the three different constellation sizes (6, 12, 24 satellites). As seen, 13 scenarios are to be investigated for each size.

3.1 Description of the Real Satellite Constellation Scenarios

Table 3 contains the main input parameters of our 39 different real satellite mission scenarios which were discussed above in short form and which we shall explain here in a little more detail. Tow thirds of the cases use two different orbit planes for positioning the LEO satellites and the last 13 cases are the constellations with 4 separate orbit planes. For the two orbit plane cases configurations of 6 and of 12 satellites were chosen.

For the symmetric configurations using two different orbit planes (left-hand and middle column of table 3), with 3 or 6 satellites sharing an orbit (orbital spacings of the LEOs 120 or 60 degrees, respectively), scenarios with different orbital plane inclinations were taken (i.e. inclinations of the two plains were 80-55, 80-30, or 98-30 degrees) and one pure sun synchronous scenarios, where both planes had the same inclination of 98 degrees. For cases with different orbit inclinations cases with node orthogonality ($\Delta\Omega = 90°$; best case) and node alignment ($\Delta\Omega = 0°$; worst case) were both considered. (For pure sun-sync scenarios only the $\Delta\Omega = 90°$ case was used because no differential precession of both orbit planes will take place.

The setup for the the asymmetric cases is essentially the same as for the symmetric ones. Here 4 or 8 satellites are occupying the higher inclined orbit plane, whereas 2 or 4 of them are located in the lower inclined orbit. We use no sun-sync only scenarios for asymmetric configurations, however, since an unequal orbit filling for two orbits at indentical inclination does not make too much sense.

The 4 orbit plane cases (O=4) were in principle handled in the same manner as the former two orbit scenarios, but we have been somewhat more restrictive with sampling the inclination dimension of the basin space in order to again limit to 7 symmetric and 6 asymmetric scenarios.

For the purely sun-synchronous orbit scenario only the fully symmetrical case (6 satellites in each of the 4 orbit planes, with $\Delta\Omega = 45°$ separated) were used. For the scenarios with $I\epsilon\{80 - 80 - 30 - 30\}$ & $I\epsilon\{98 - 98 - 30 - 30\}$, the two pairs of equally inclined orbits (i.e., 98-98, 30-30 degrees) were spaced 90 degrees in Ω (this spacing is time-independent due to the identical inclination). The pairs, in turn, were split with 45° and 0° against each other to simulate the two extremes of minimal and maximal overlap of nodes. For the last constellation case 4 different orbital inclinations were used, with an orbit plane separation of 45° (orbit nodes maximally dispersed, best case) and of 0° (all orbit nodes aligned, worst case), respectively.

The calculation and visualization process of the real satellite scenarios is made in the same manner as was documented in section 2.4 for the calculation and in section 2.6 for the visualization of the results of the basic scenario.

The visualization process was also handled in the same manner as before. Small differences can be noticed when inspecting the plots in the first header line of the plot panels. Here, having now more than one orbit plane for each scenario means that the satellite and inclination values for a single scenario were growing longer in order to include all information about the individual satellite numbers per orbital plane and about the different orbital inclinations of these planes. Generally, all characteristics of the plots in this chapter (figures 16 to 45) are as explained in detail in sections 2.6 and 2.7.

Figures 16 - 25 contain the results for the 6 sat/2 orbit symmetric satellite scenario with 3

satellites per orbit (upper panel), as well as the results for its asymmetric complement with 4 satellites in the higher inclined orbit and two in the lower inclined orbit (lower panel).

Figures 16 to 20 show the cases with node alignment ($\Omega = 0°$), while figures 21 to 25 show the cases with node orthogonality ($\Omega = 90°$). As noted before, the pure sun-sync constellation was only calculated for the latter scenario.

A quick look at figure 16 shows that the number of occultation events is quite unevenly distributed over the globe, the maximum number density reached is 7.6 [Mm^{-2}]. A comparison with figure 21 (the $\Omega = 90°$ case) shows immediately the big difference between the optimum node separation and node alignment. Interesting is also that the symmetric satellite constellation (upper panel case of figure 21) gives already reasonably smooth average occultation event distribution.

Figures 17, 18, 22, and 23, showing the mean distances and their dispersion, apear to be consistent with the number density results of figures 16 and 21.

The mean time separations and the time separation dispersions shown in figures 19, 20, 24, and 25 are showing no big difference between the best case and worst case scenarios. At higher latitudes the average time separation is generally greater than in the more equatorward regions.

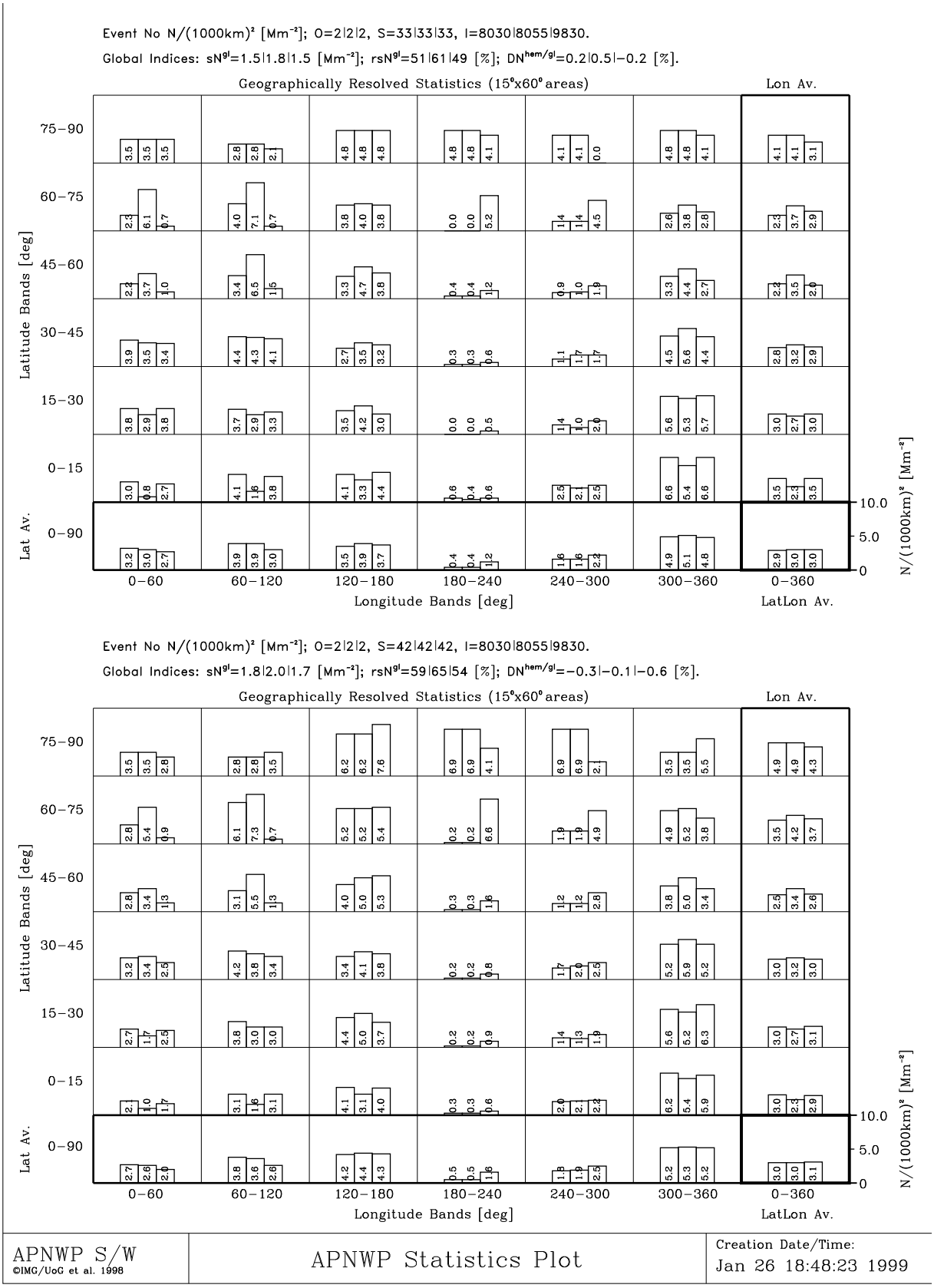

Figure 16: Occultation event number densities $N/(1000km)^2$ $[Mm^{-2}]$.

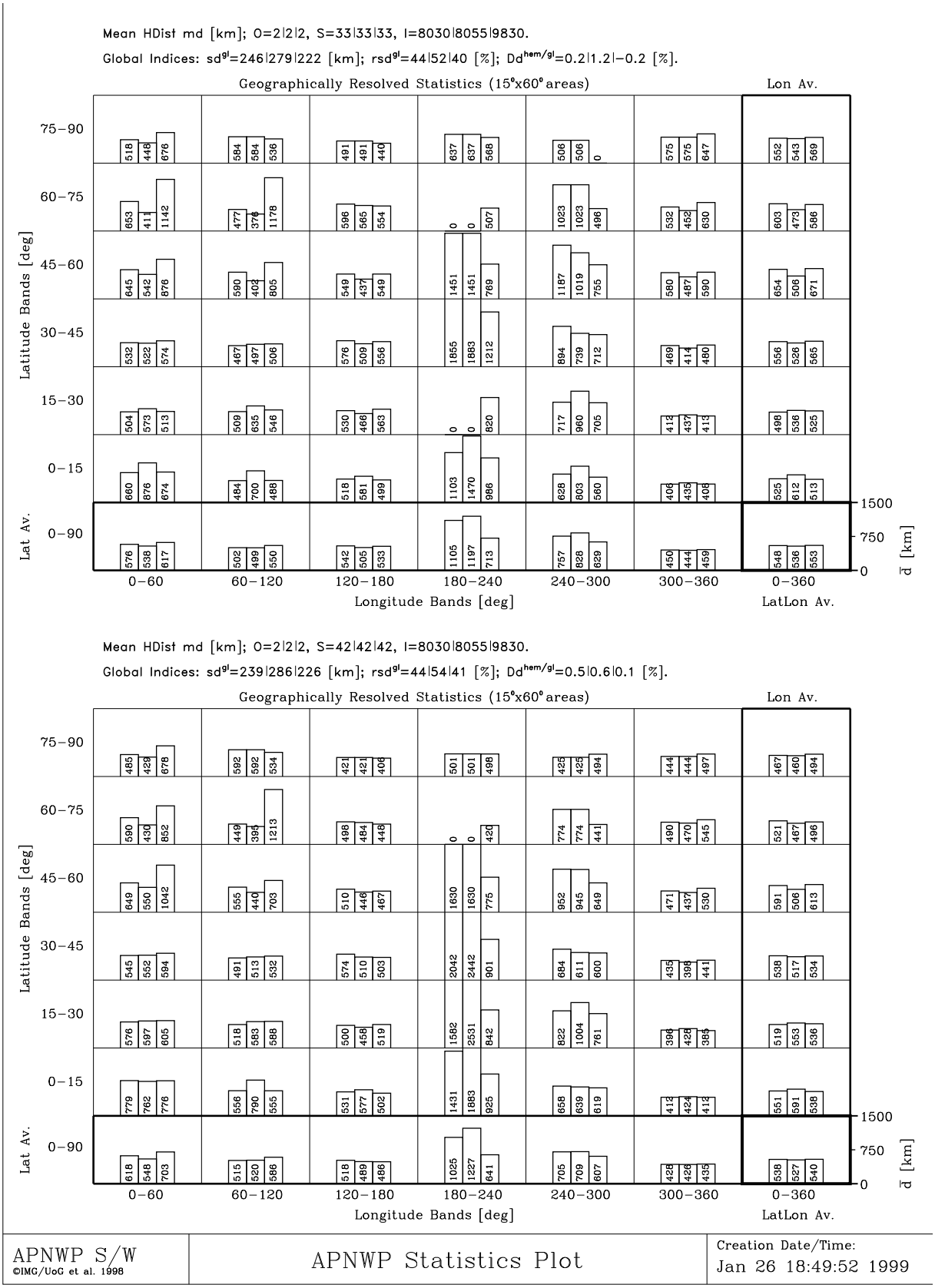

Figure 17: Mean horizontal distances $\overline{d}$ $[km]$.

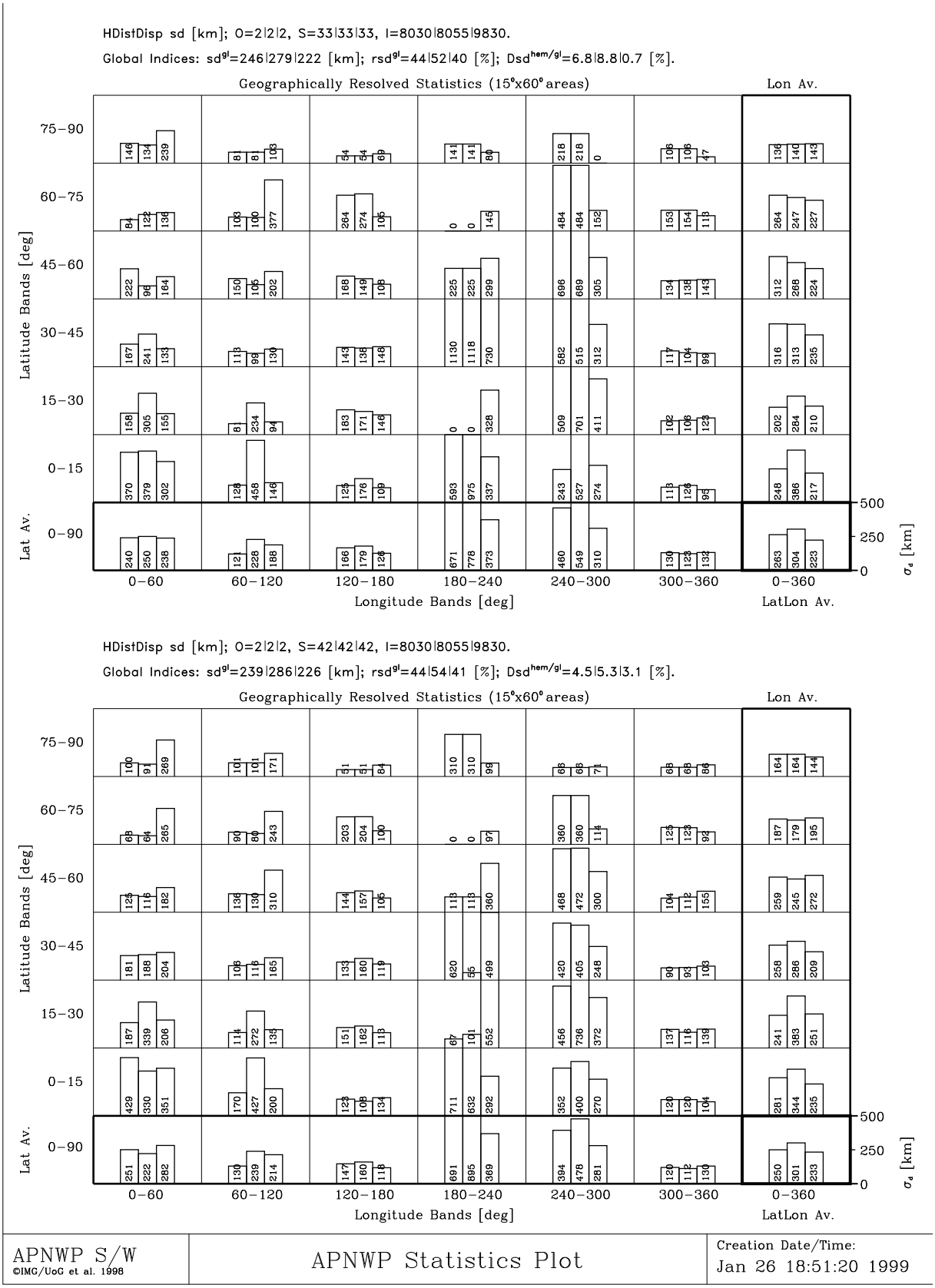

Figure 18: Horizontal distance dispersion σ_d $[km]$.

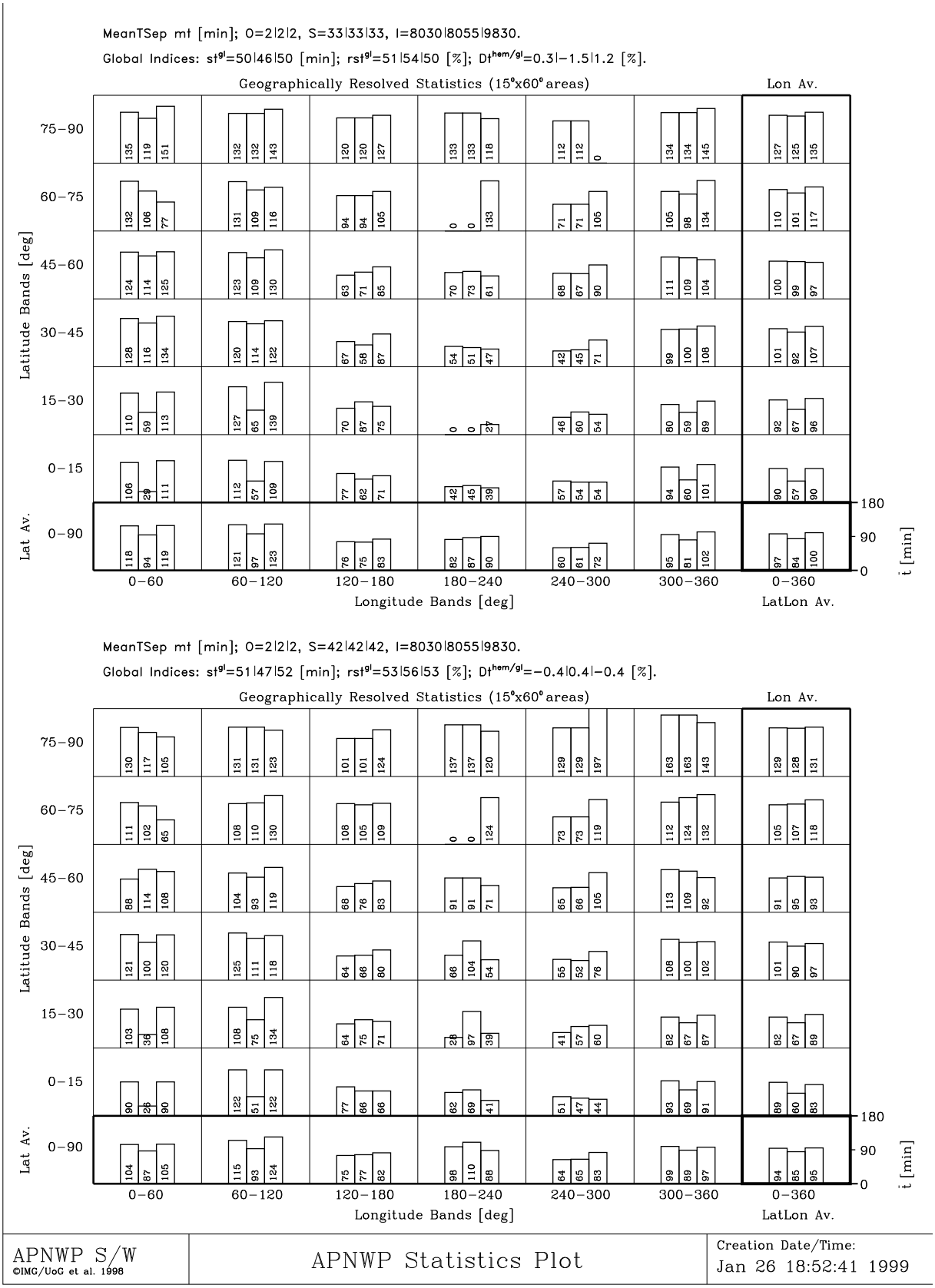

Figure 19: Mean time separation $\overline{t}$ $[min]$.

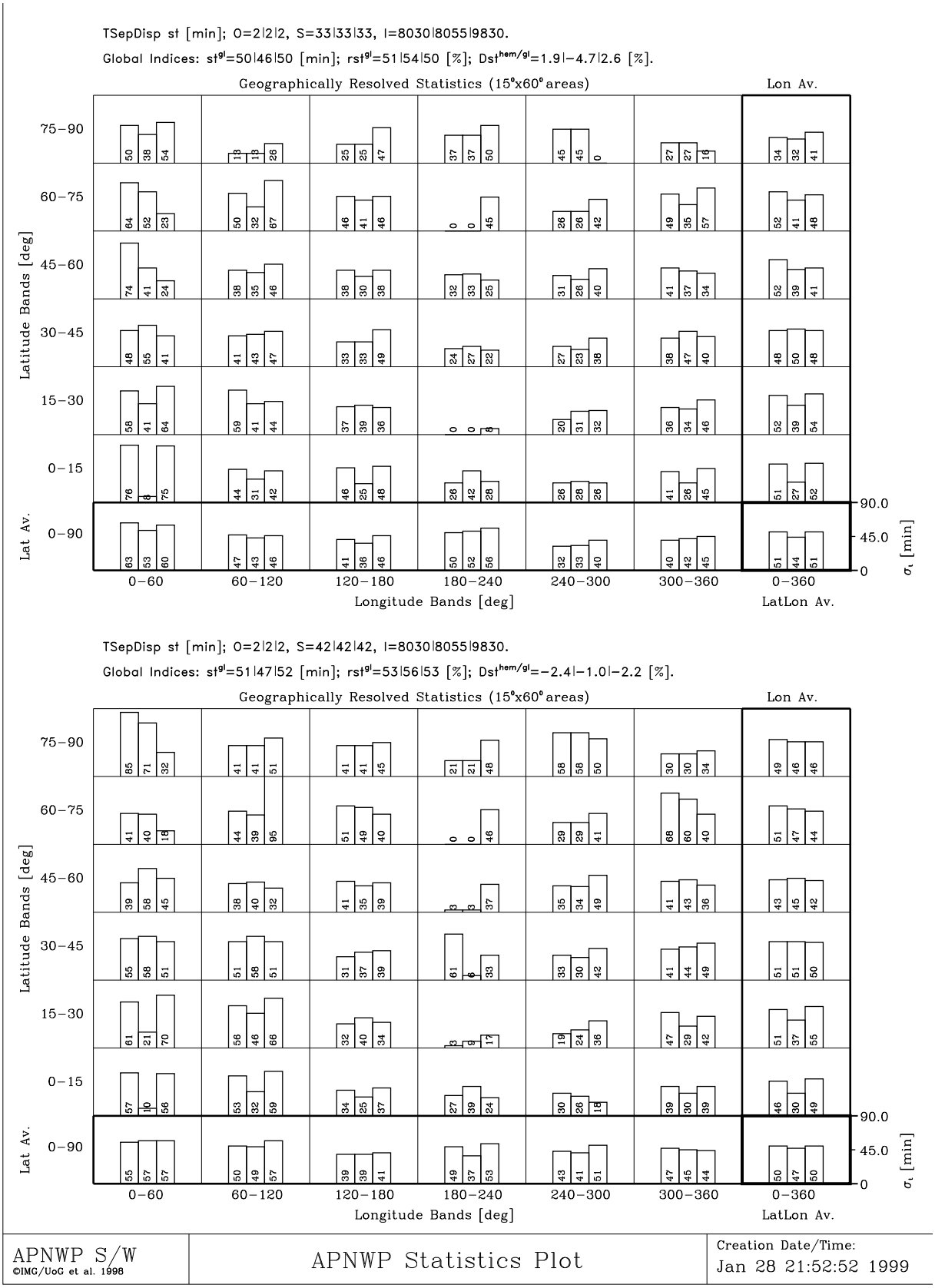

Figure 20: Time separation dispersion σ_t $[min]$.

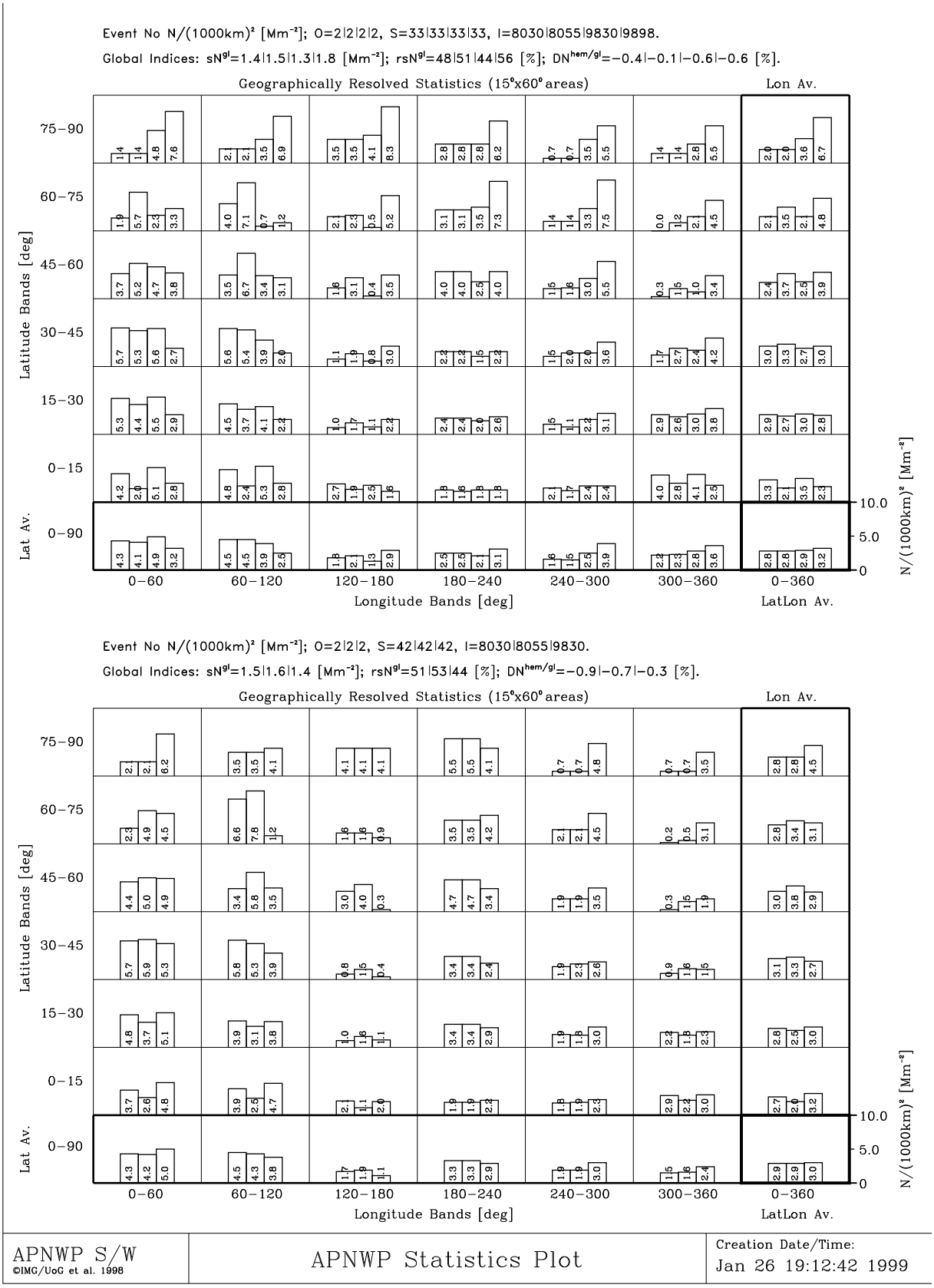

Figure 21: Occultation event number densities $N/(1000km)^2$ $[Mm^{-2}]$.

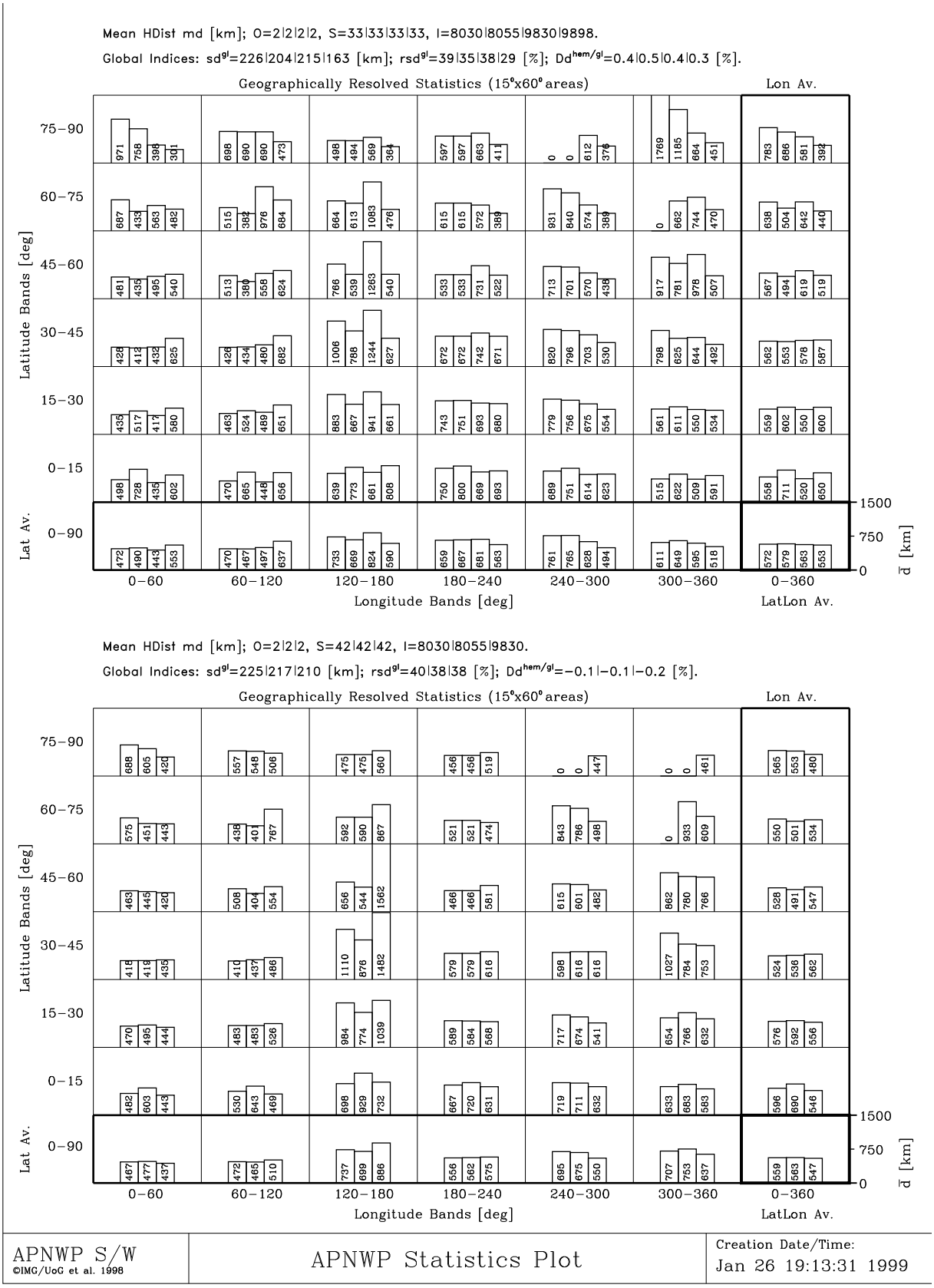

Figure 22: Mean horizontal distances $\overline{d}$ $[km]$.

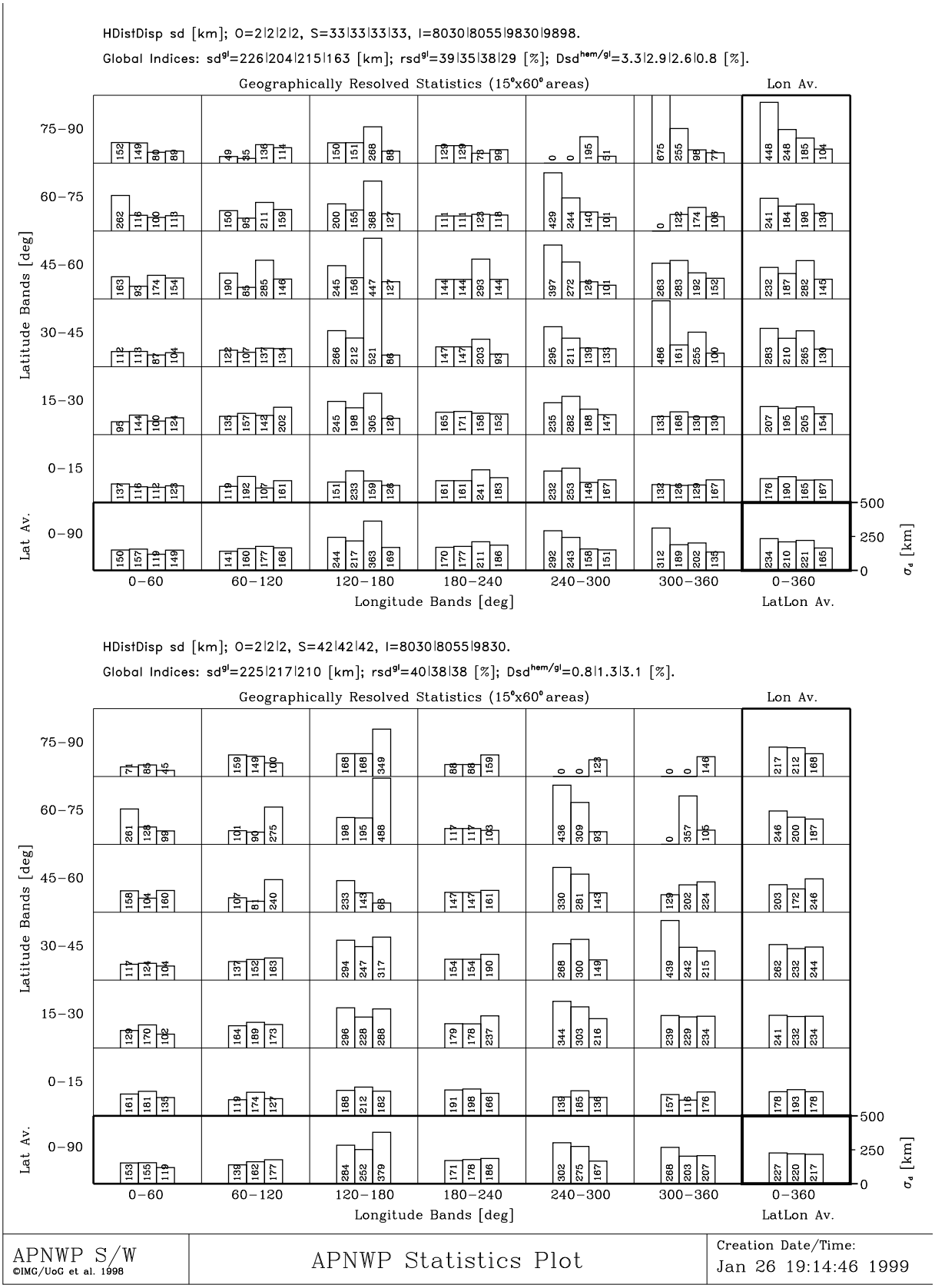

Figure 23: Horizontal distance dispersion σ_d $[km]$.

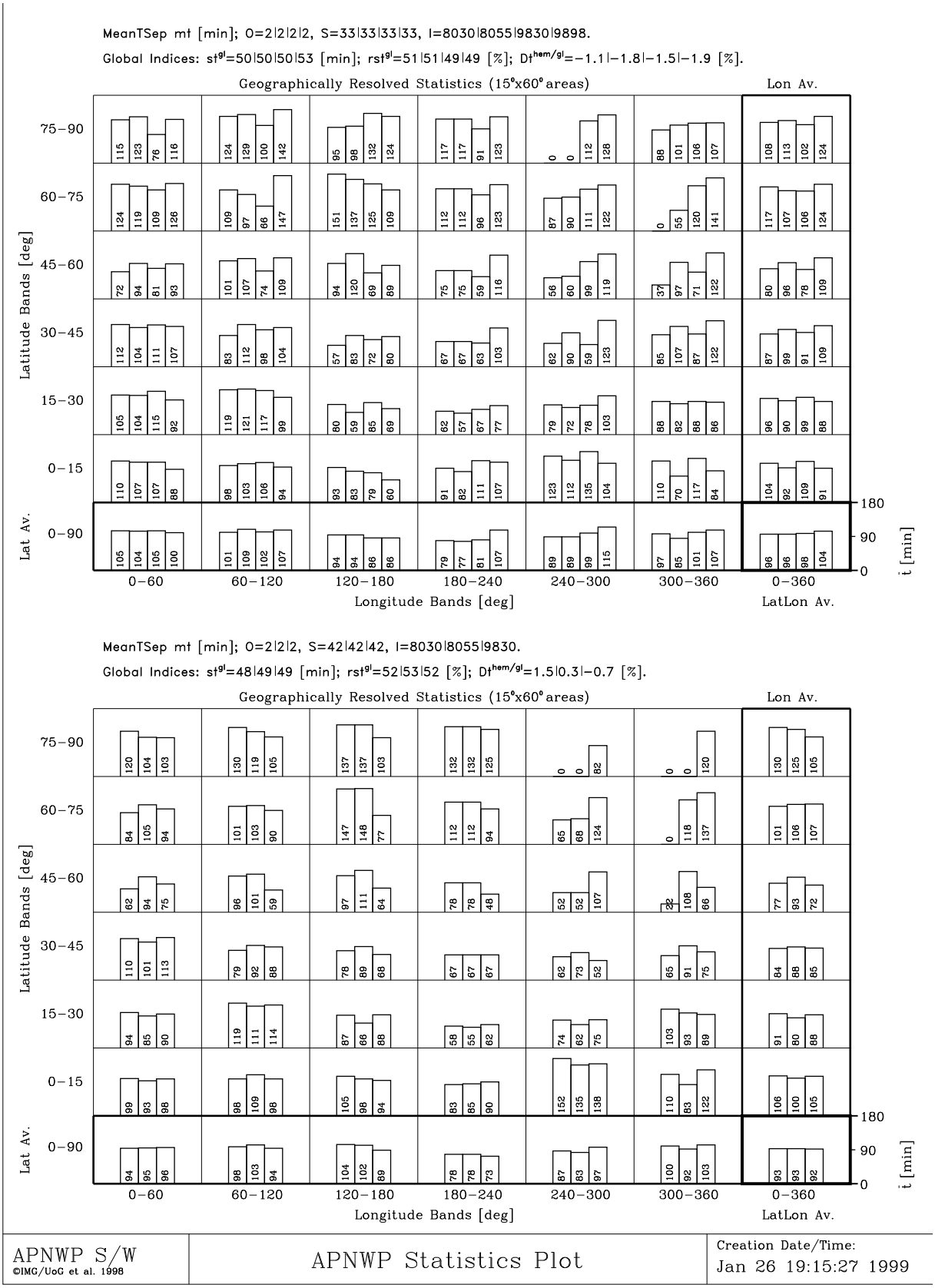

Figure 24: Mean time separation $\overline{t}$ $[min]$.

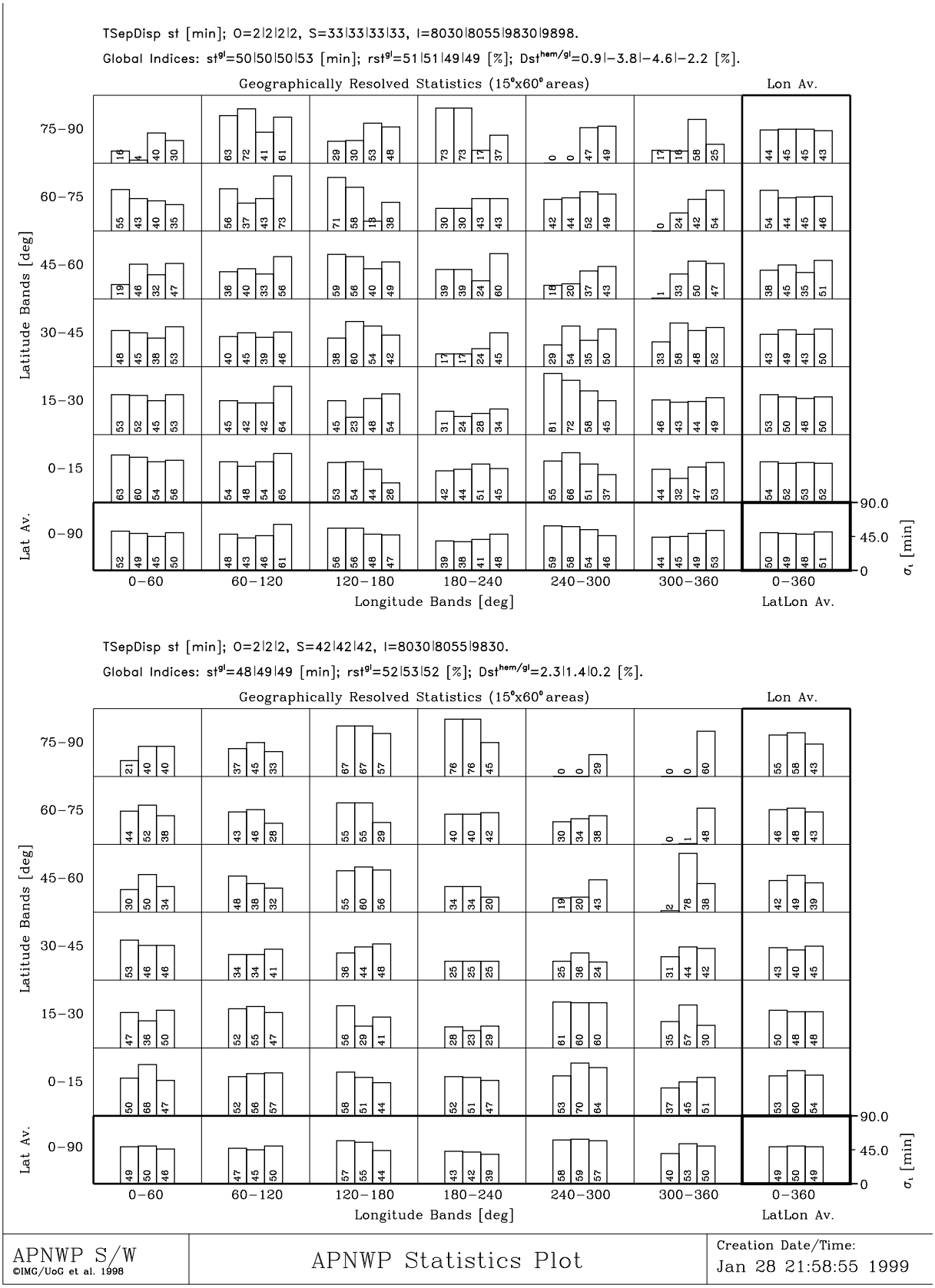

Figure 25: Time separation dispersion σ_t $[min]$.

Figures 26 - 35 contain the results for the 12 sat/2 orbit symmetric satellite scenario with 6 satellites per orbit (upper panel), as well as the results for its asymmetric complement with 8 satellites in the higher inclined orbit and 4 in the lower inclined orbit (lower panel).

Figures 26 to 30 show the cases with node alignment ($\Omega = 0°$), while figures 31 to 35 show the cases with node orthogonality ($\Omega = 90°$). As noted before, the pure sun-sync constellation was only calculated for the latter scenario.

A quick look at figure 26 shows that the number of occultation events still is somewhat uneven distributed over the globe. The maximum occultation event density reaches here 17.2 [Mm^{-2}].

The comparison with figure 31 (the $\Omega = 90°$ case) shows immediately the significant difference between the optimum node separation and no node separation. Some scenarios give already quite smooth average occultation event distribution during the node-orthogonality situation shown in figure 31. What is also clearly seen is that the pure sun-sync scenario yields significantly higher event numbers in the polar regions than the rest of the constellation scenarios.

Figures 27, 28, 32, and 33, illustrating mean distances and distance dispersions, are consistent with the number density results of figures 26 and 31, respectively. The mean distances have been reduced compared to the 6-sat scencarios, as expected. In regions with relatively low event number density the distance dispersion is still relatively high, though.

Like for their predecessors for 6 satellites, the results for the mean time separation (figures 29 and 34) and the time separation dispersion (figures 30 and 35) show no big difference between the best case and worst case scenarios. Also at higher latitudes the average time separation is generally greater than in the more equatorwards regions. In absolute values the time measures seem to possess no significant dependence on constellation size.

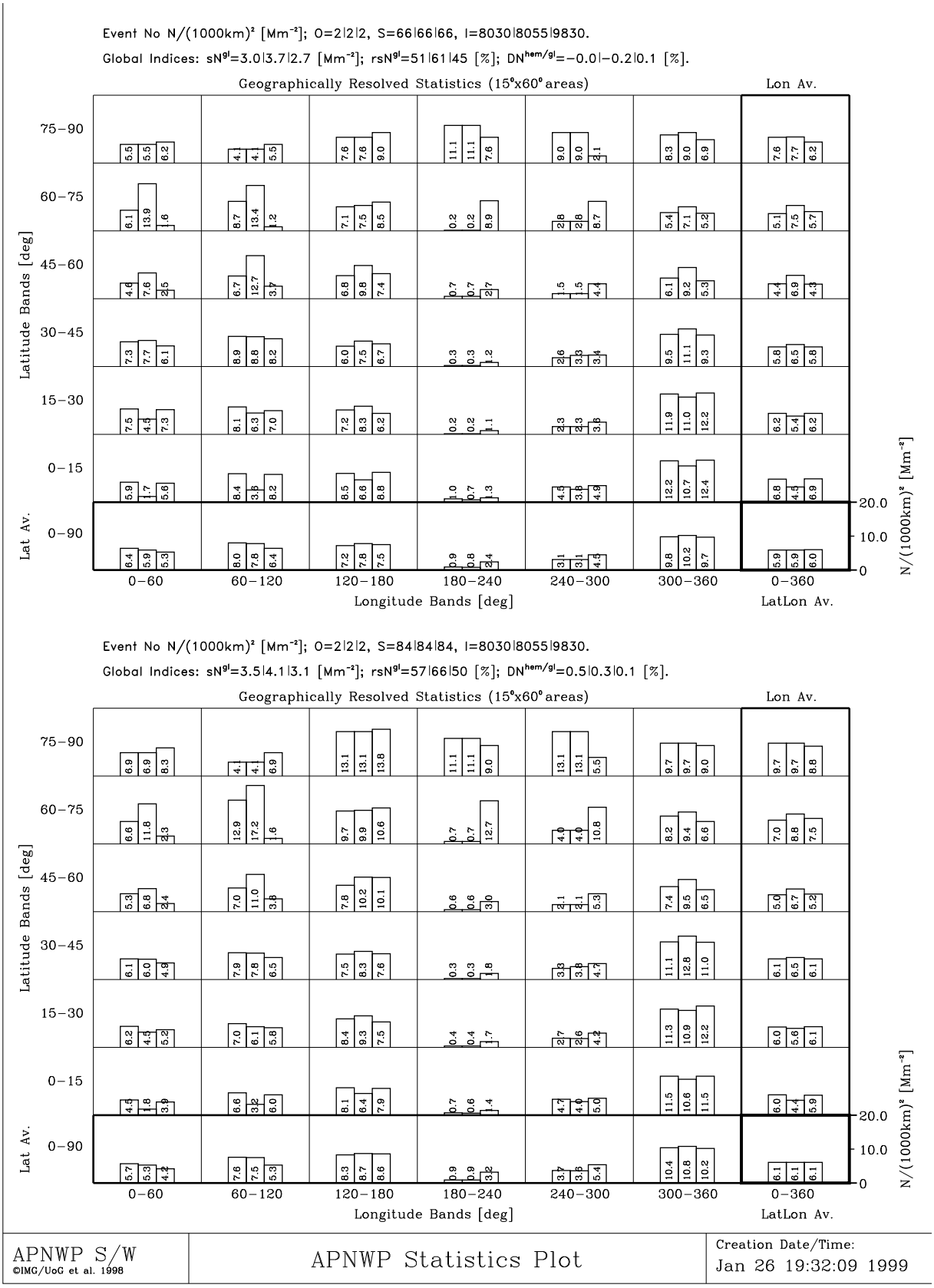

Figure 26: Occultation event number densities $N/(1000km)^2$ $[Mm^{-2}]$.

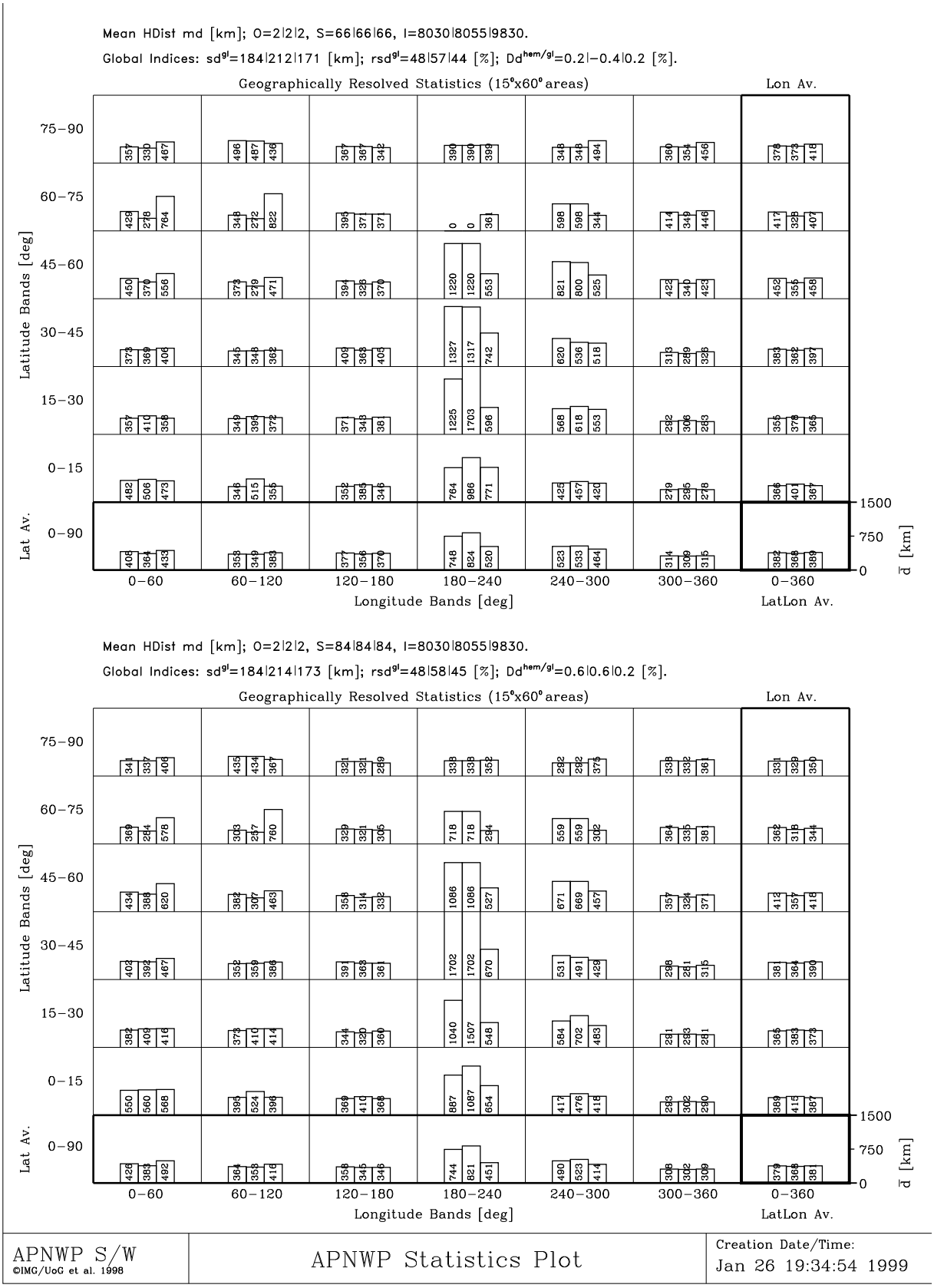

Figure 27: Mean horizontal distances $\overline{d}$ $[km]$.

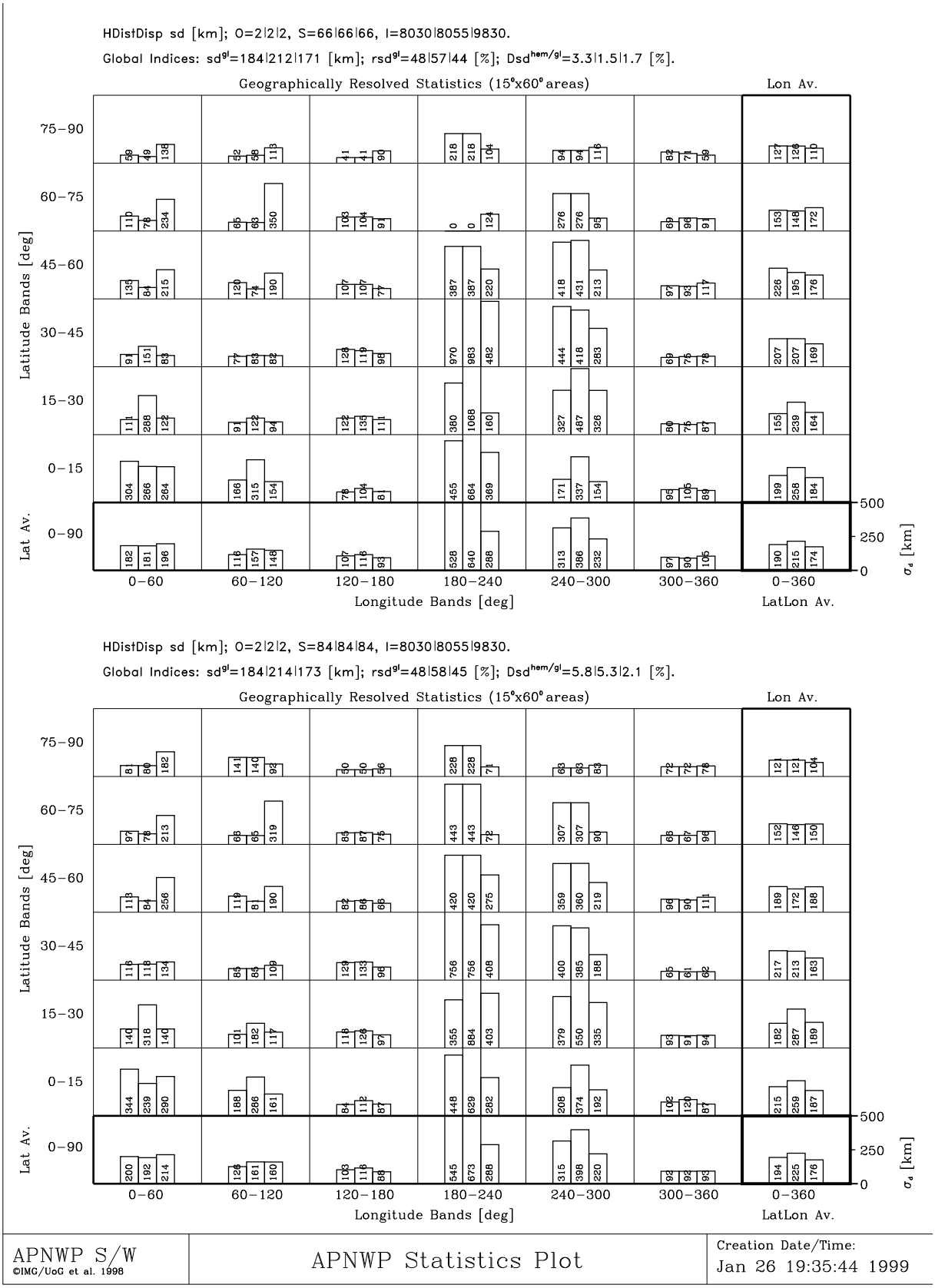

Figure 28: Horizontal distance dispersion σ_d $[km]$.

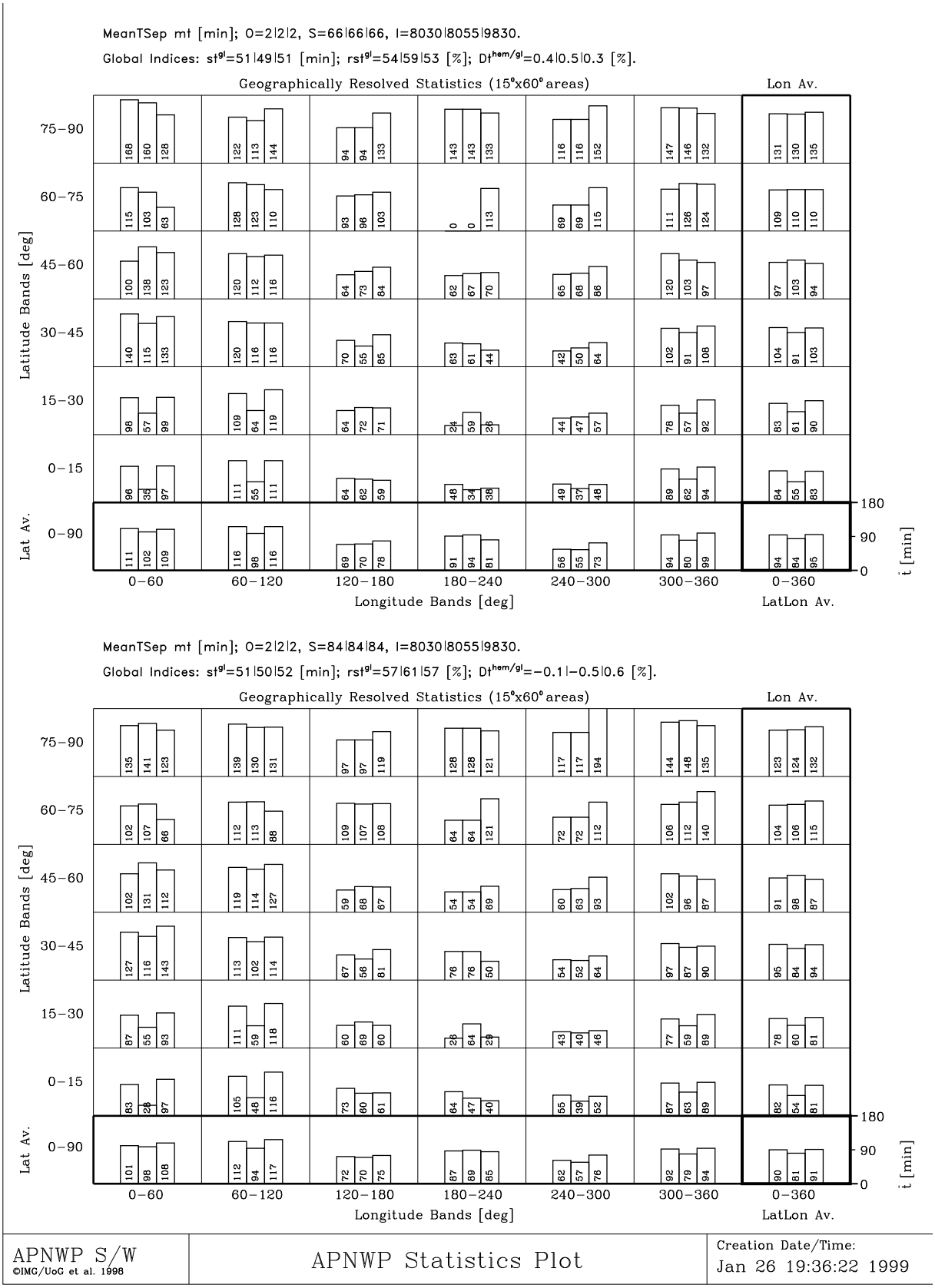

Figure 29: Mean time separation $\overline{t}$ $[min]$.

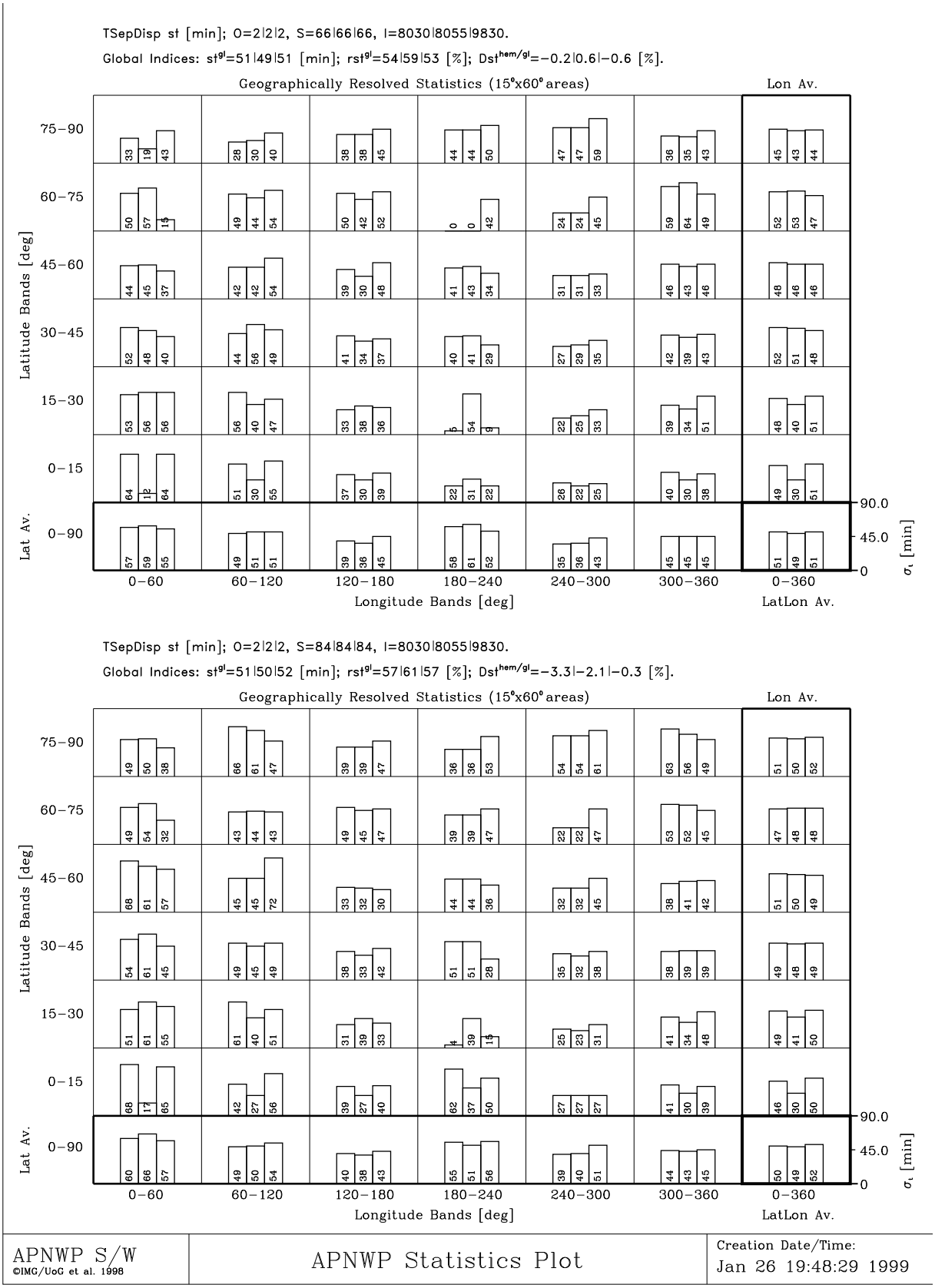

Figure 30: Time separation dispersion σ_t $[min]$.

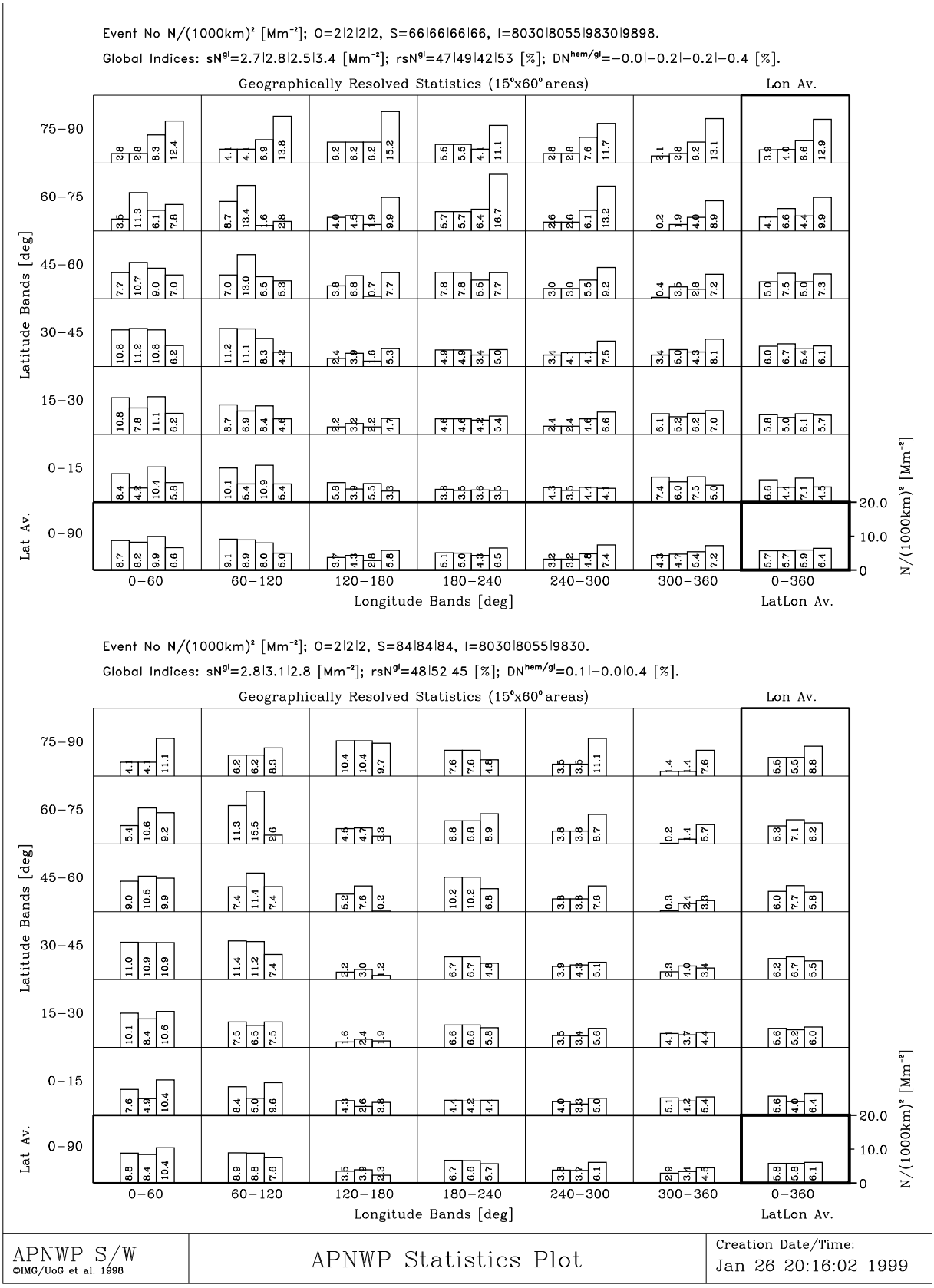

Figure 31: Occultation event number densities $N/(1000km)^2$ $[Mm^{-2}]$.

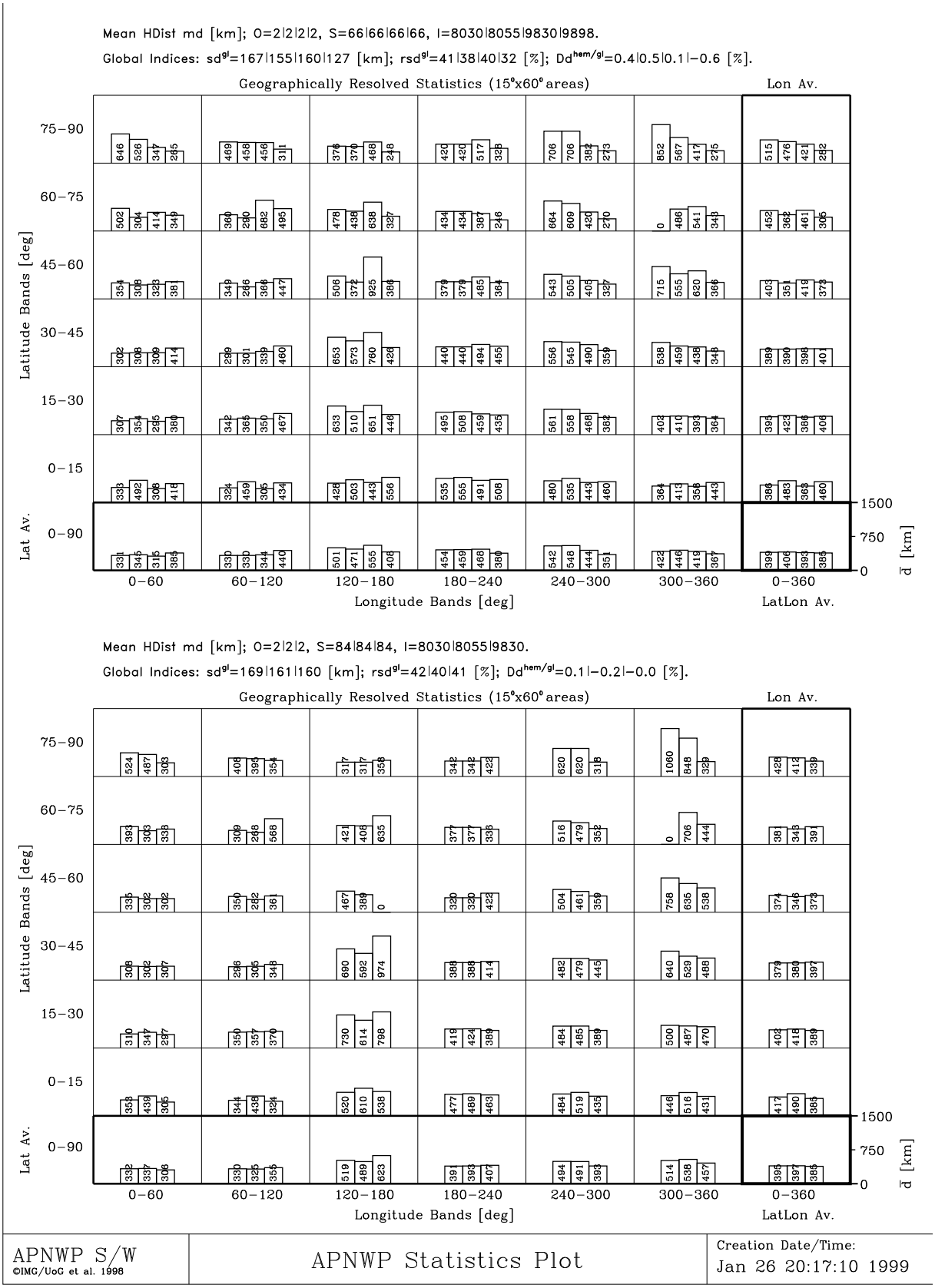

Figure 32: Mean horizontal distances $\overline{d}$ $[km]$.

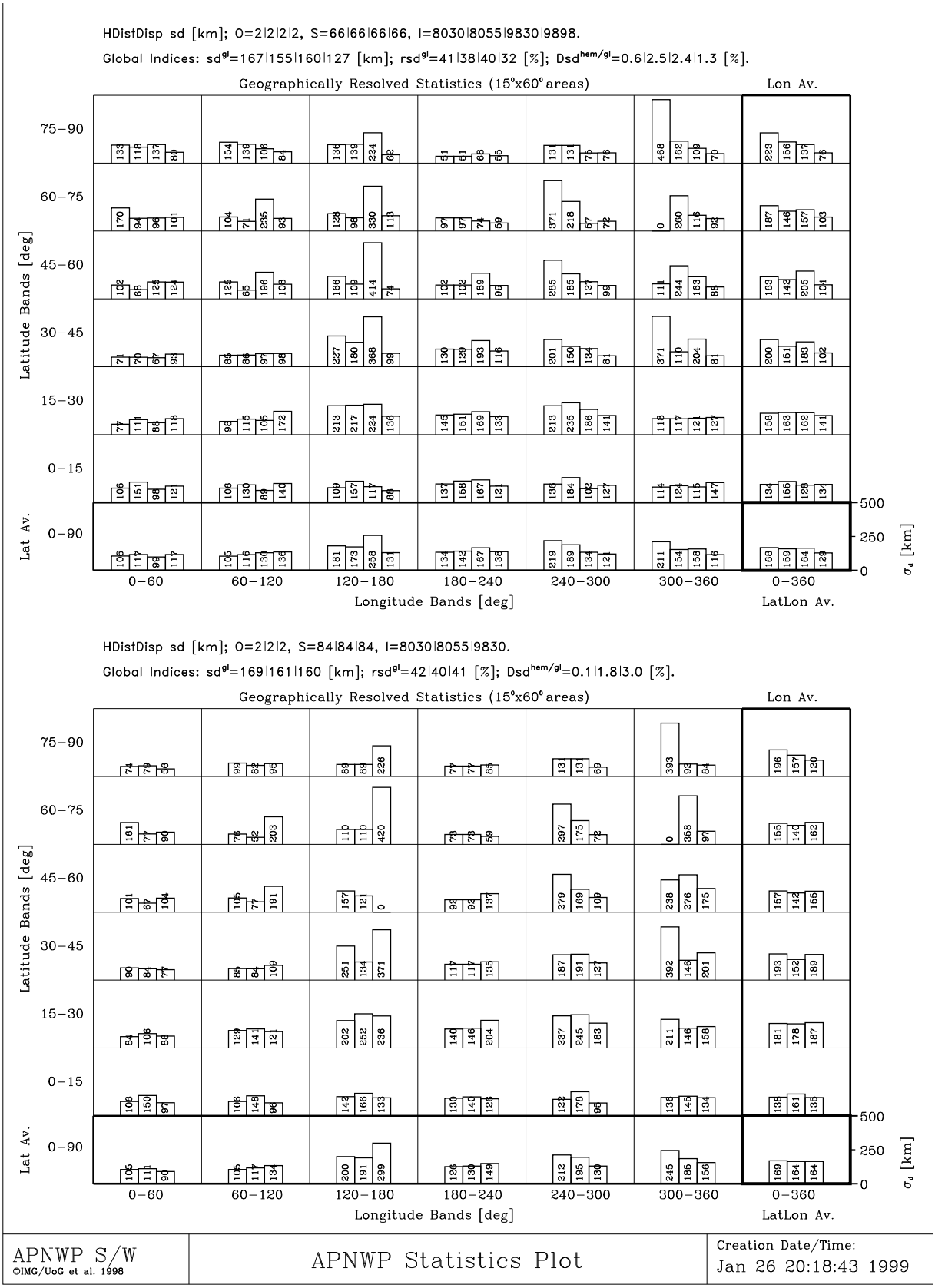

Figure 33: Horizontal distance dispersion σ_d $[km]$.

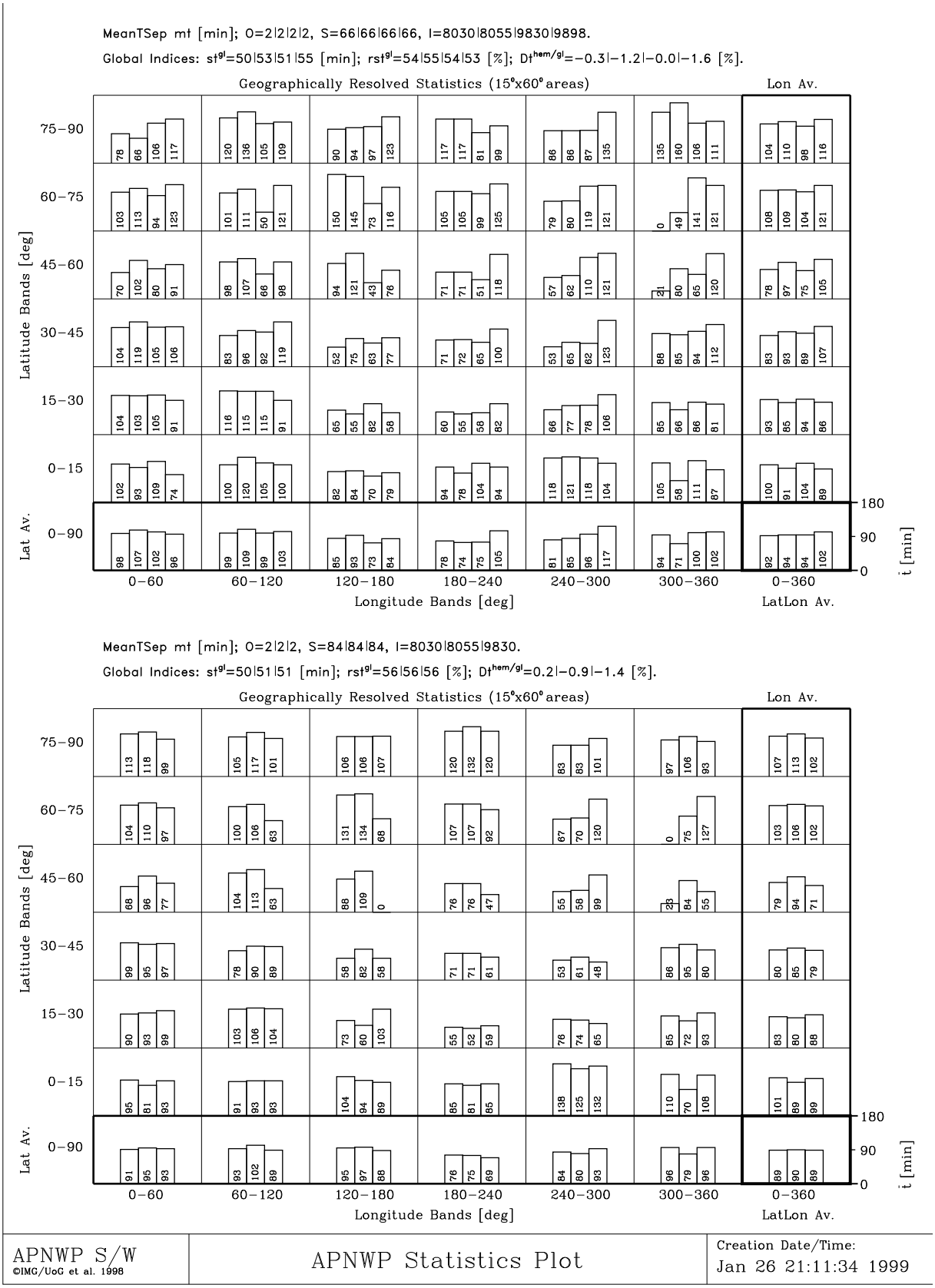

Figure 34: Mean time separation $\overline{t}$ $[min]$.

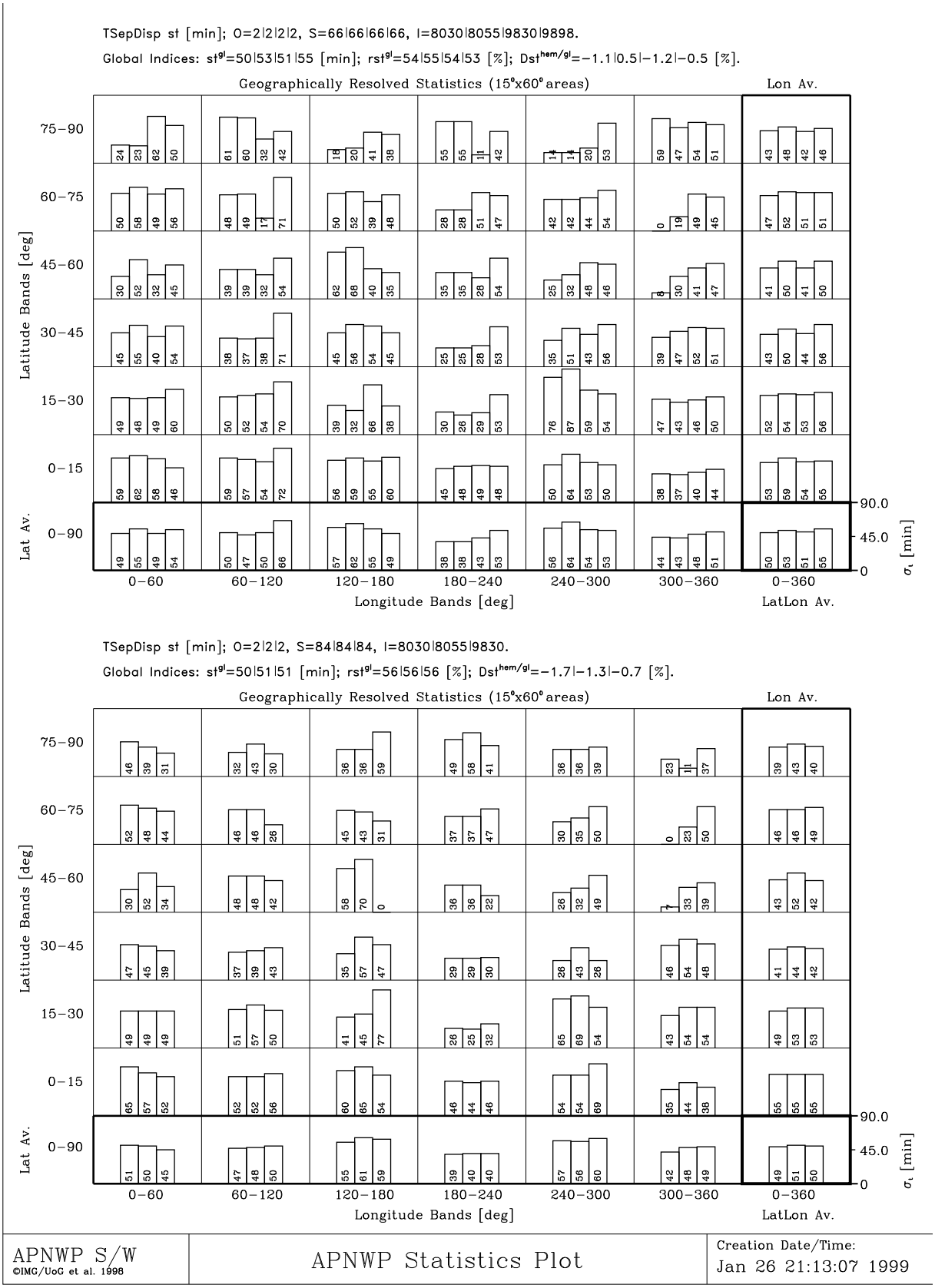

Figure 35: Time separation dispersion σ_t $[min]$.

Figures 36 - 45 contain the results for the 24 sat/4 orbit symmetric satellite scenario with 6 satellites per orbit (upper panel), as well as the results for its asymmetric complement with 8 satellites in the higher inclined orbits and 4 in the lower inclined orbits (lower panel).

Figures 36 to 40 show the cases with node alignment ($\Omega = 0°$), while figures 41 to 45 show the cases with maximal node dispersion ($\Omega = 45°$). As notedbefore, the pure sun-sync constellation was only calculated forthe latter scenario.

A quick look at figure 36 shows that with 24 LEOs in orbit symmetrically sharing 4 different orbit planes with different orbit inclinations the number of occultation events is now quite equally distributed over geographic space. A comparison of figures 36 and 41 shows that the question of node alignment or dispersion begins to play a more minor role for that large, well distributed constellations. The dependence on the state of the nodes is quite reduced already though still some effect is seen. are d as seen before a distinct improvement over the former worst case scenarios. The global situation is quite acceptable.

Figures 37, 38, 42, and 43, showing mean distances and distance dispersions, are again quite consistent with the number density results shown in Figures 36 and 41. We see that this constellation, showing in average mean distances below 300 km, already meets the requirements of table 1.

For the 24 satellite constellations the overview shows that the mean time separation (figure 39 and 44) and the time separation dispersion (figure 40 and 45) are more equally distributed than in the former cases with smaller constellations. Especially in the scenarios with equally separated satellites per orbit, the differences between the individual cells are relatively small (for both variables) with average values for the time separation near 2 hours and average value near 50 minutes for the time dispersion, respectively. Note that the absolute values for the time separation definitely do not decrease with constellation size, they stay roughly constant.

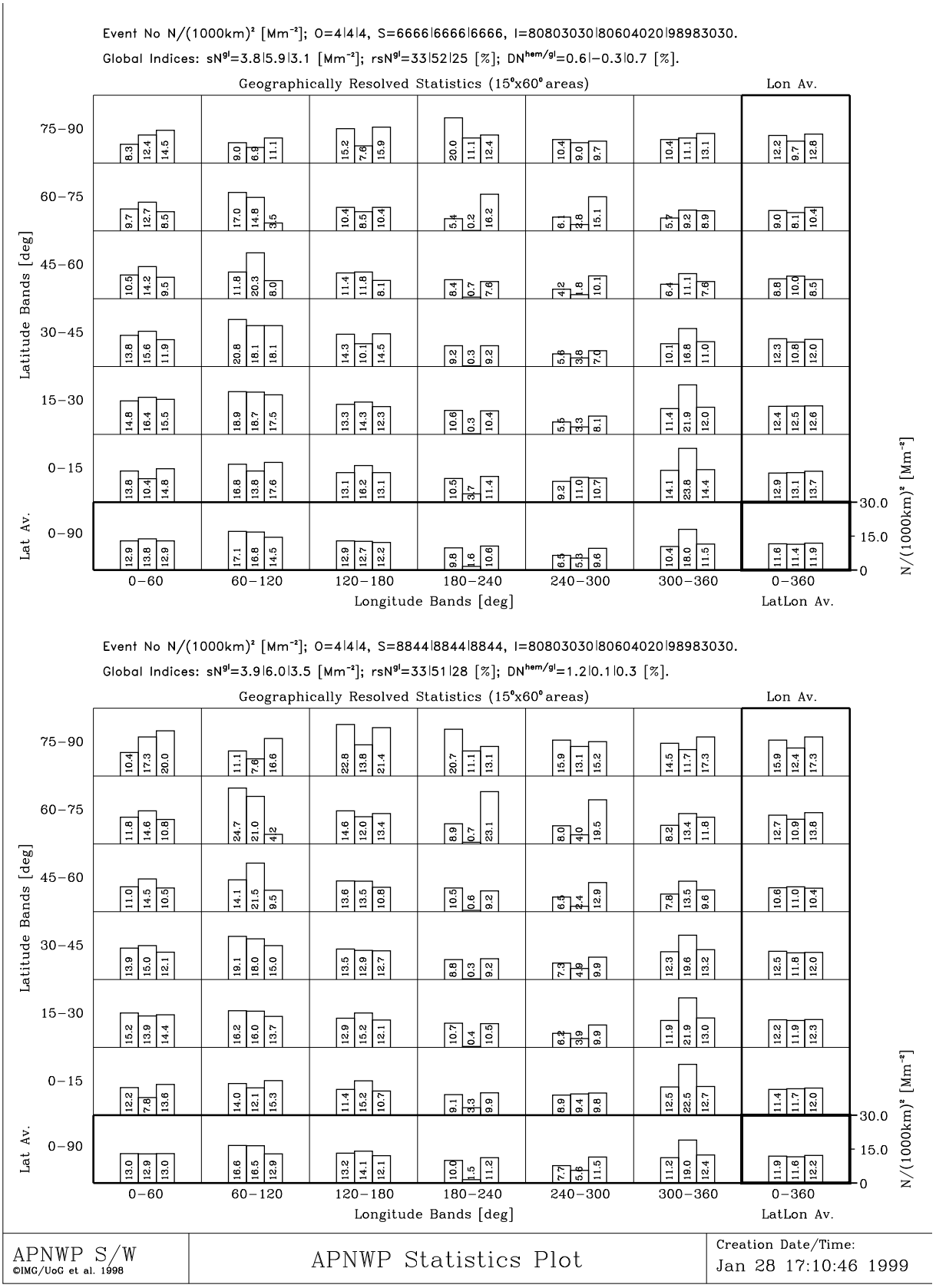

Figure 36: Occultation event number densities $N/(1000km)^2$ $[Mm^{-2}]$.

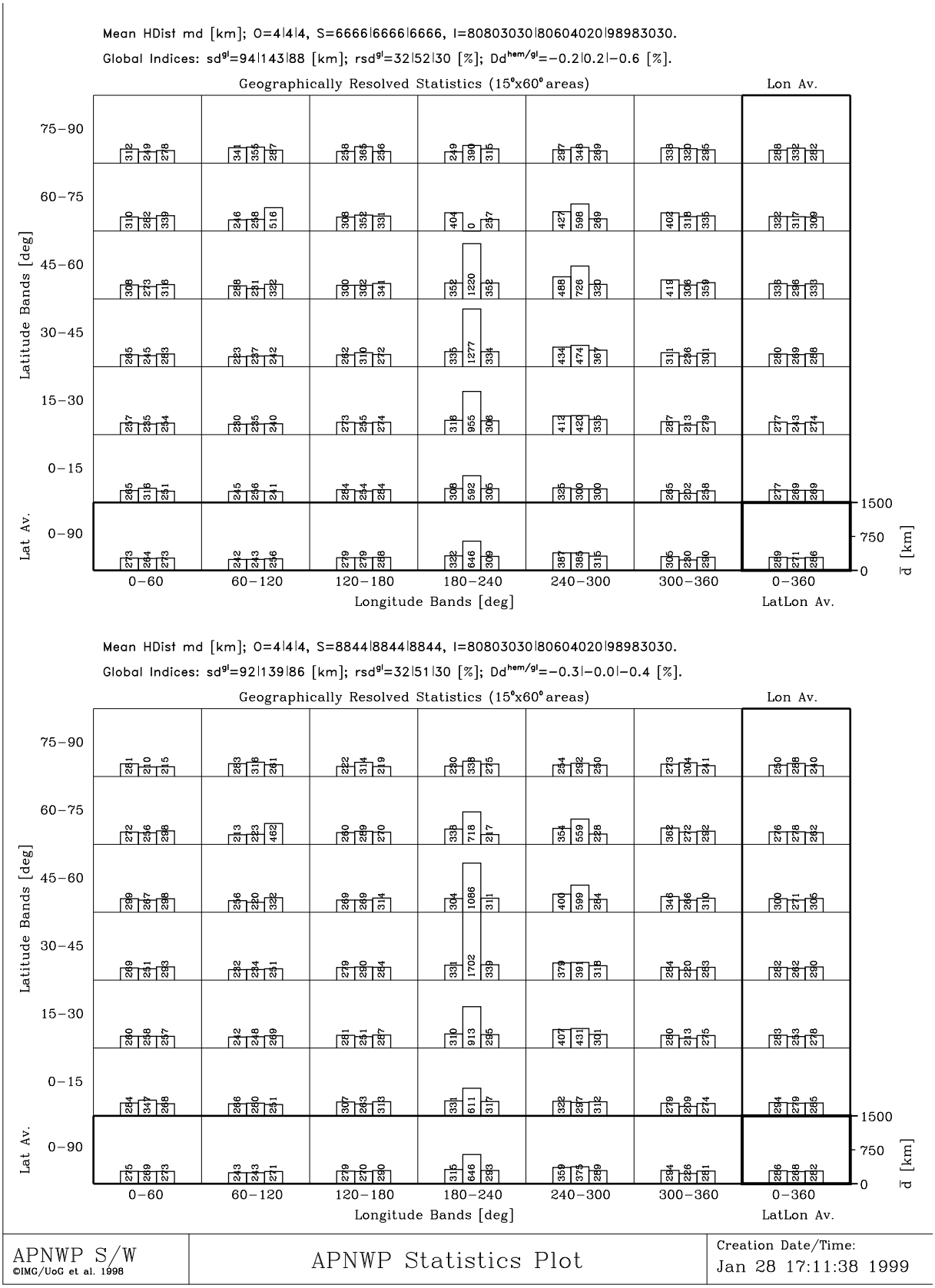

Figure 37: Mean horizontal distance $\overline{d}$ $[km]$.

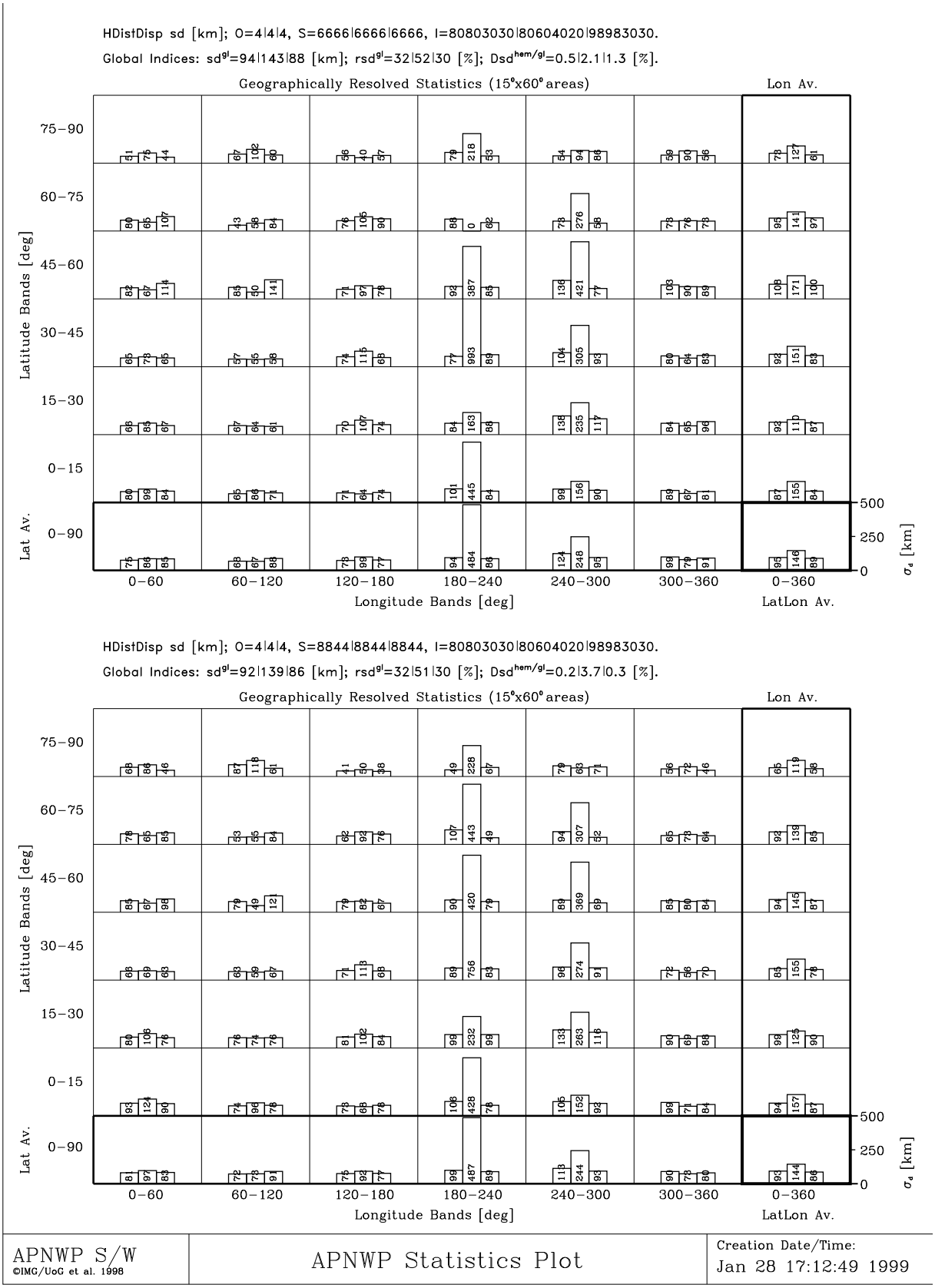

Figure 38: Horizontal distance dispersion σ_d $[km]$.

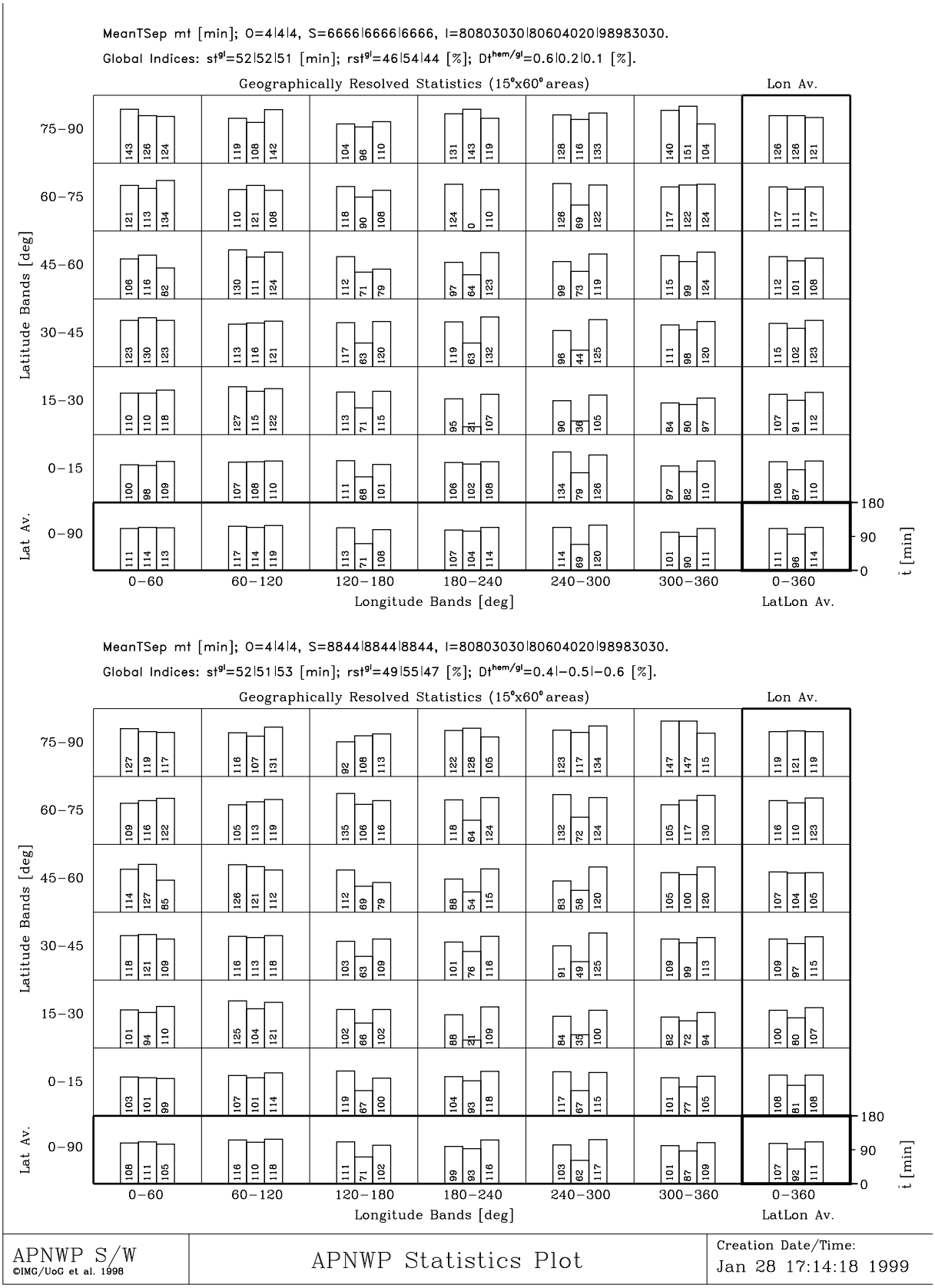

Figure 39: Mean time separation $\overline{t}$ $[min]$.

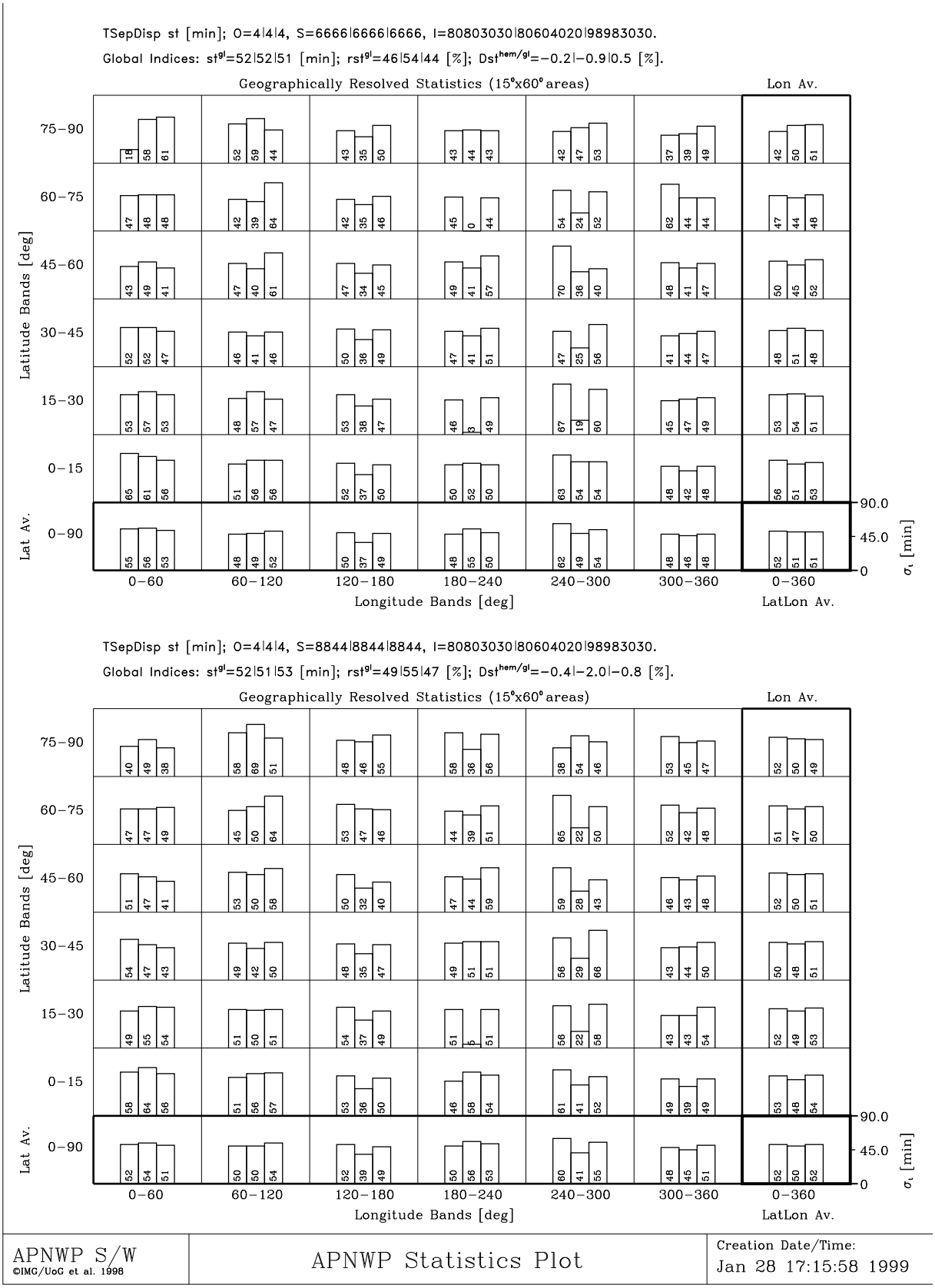

Figure 40: Time separation dispersion σ_t $[min]$.

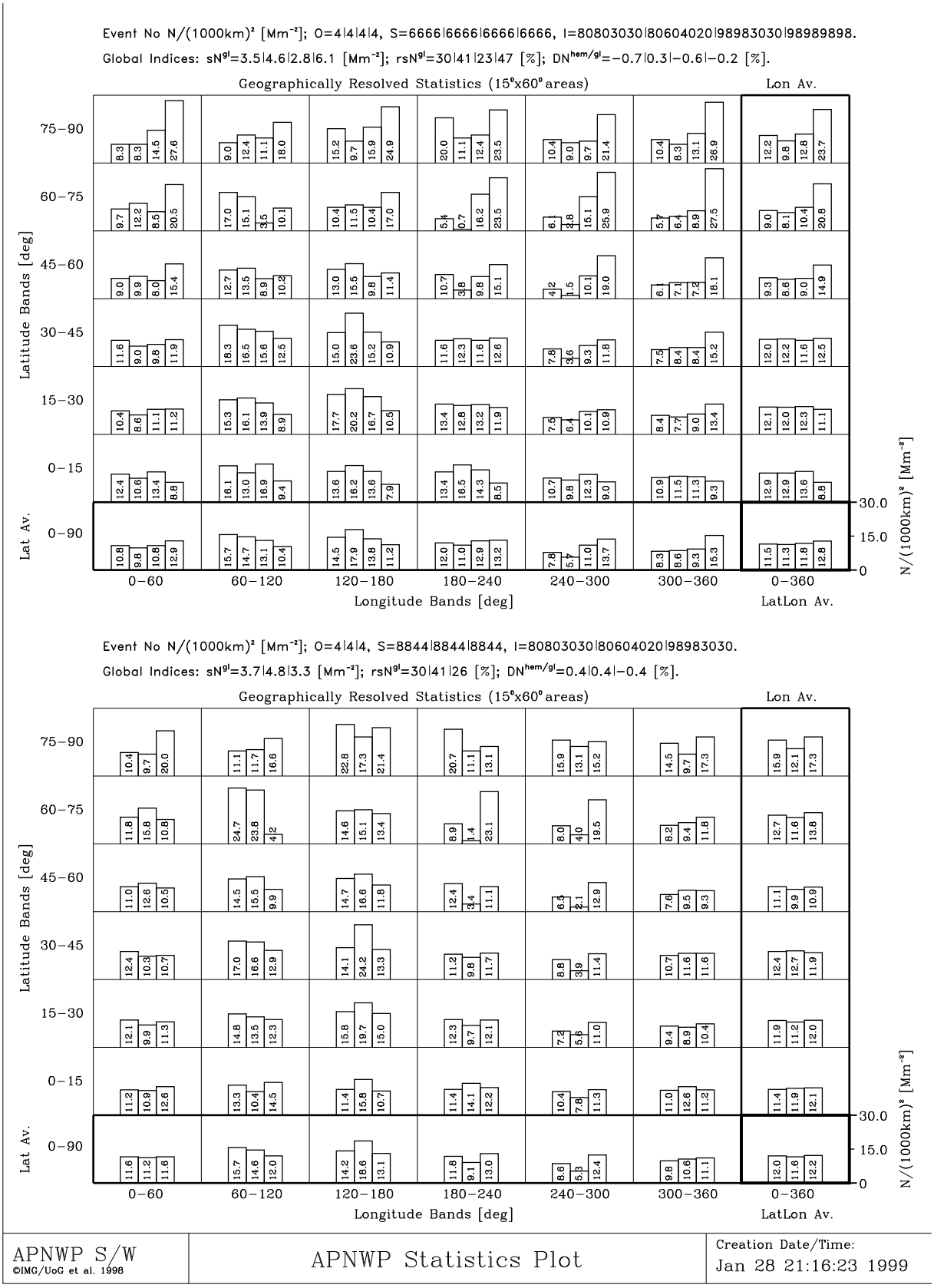

Figure 41: Occultation event number densities $N/(1000km)^2$ $[Mm^{-2}]$.

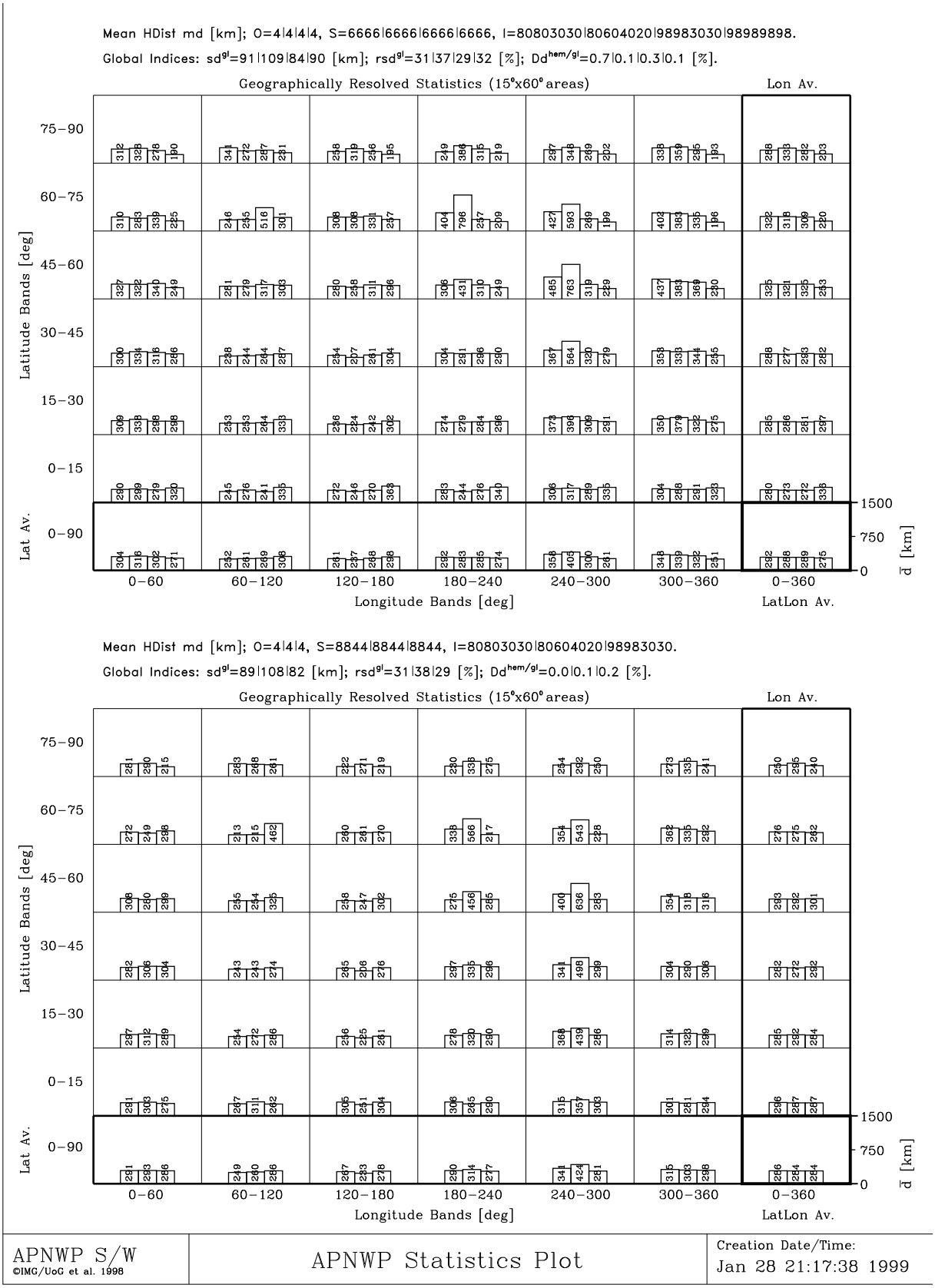

Figure 42: Mean horizontal distances $\overline{d}$ $[km]$.

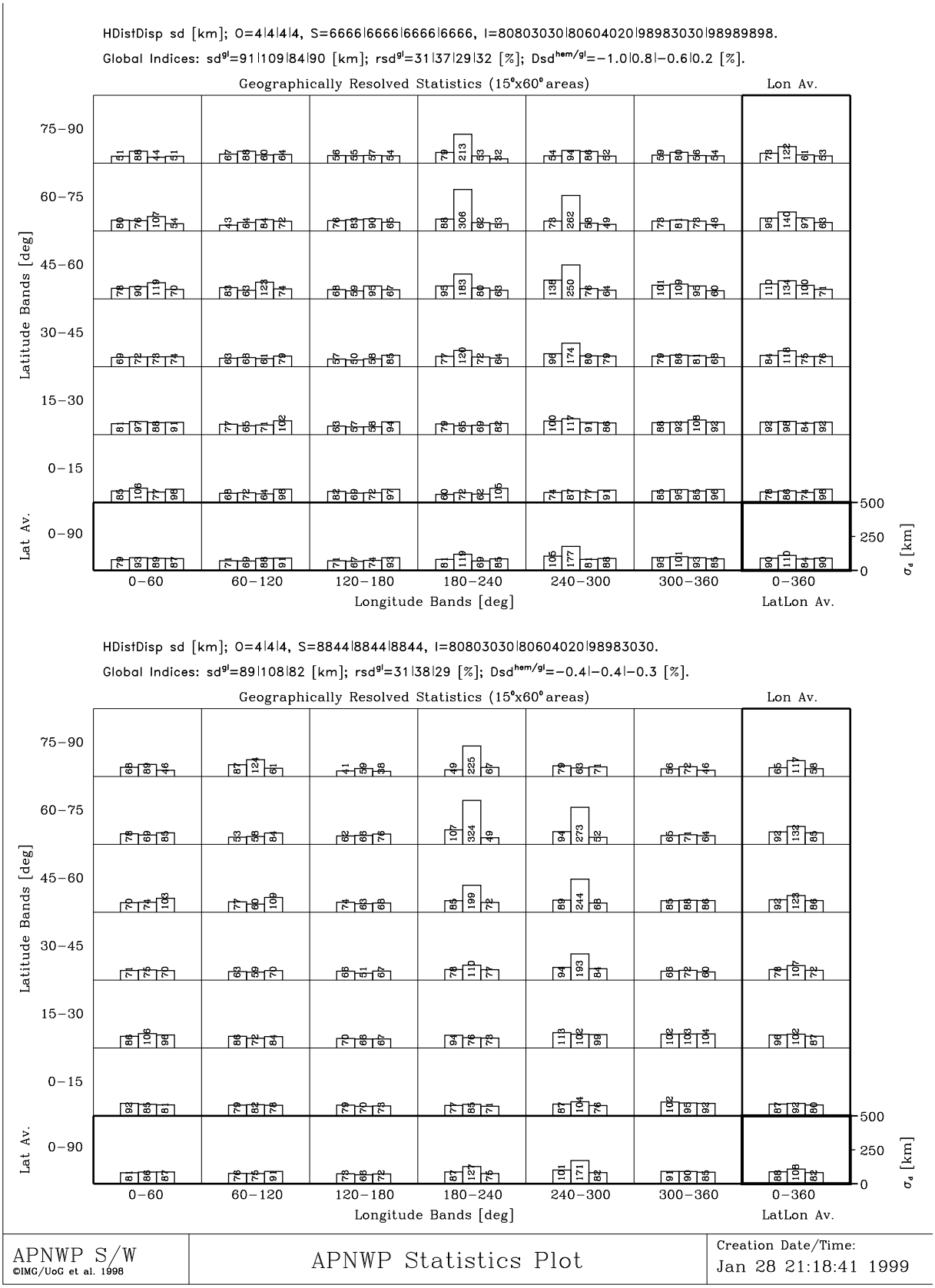

Figure 43: Horizontal distance dispersion σ_d $[km]$.

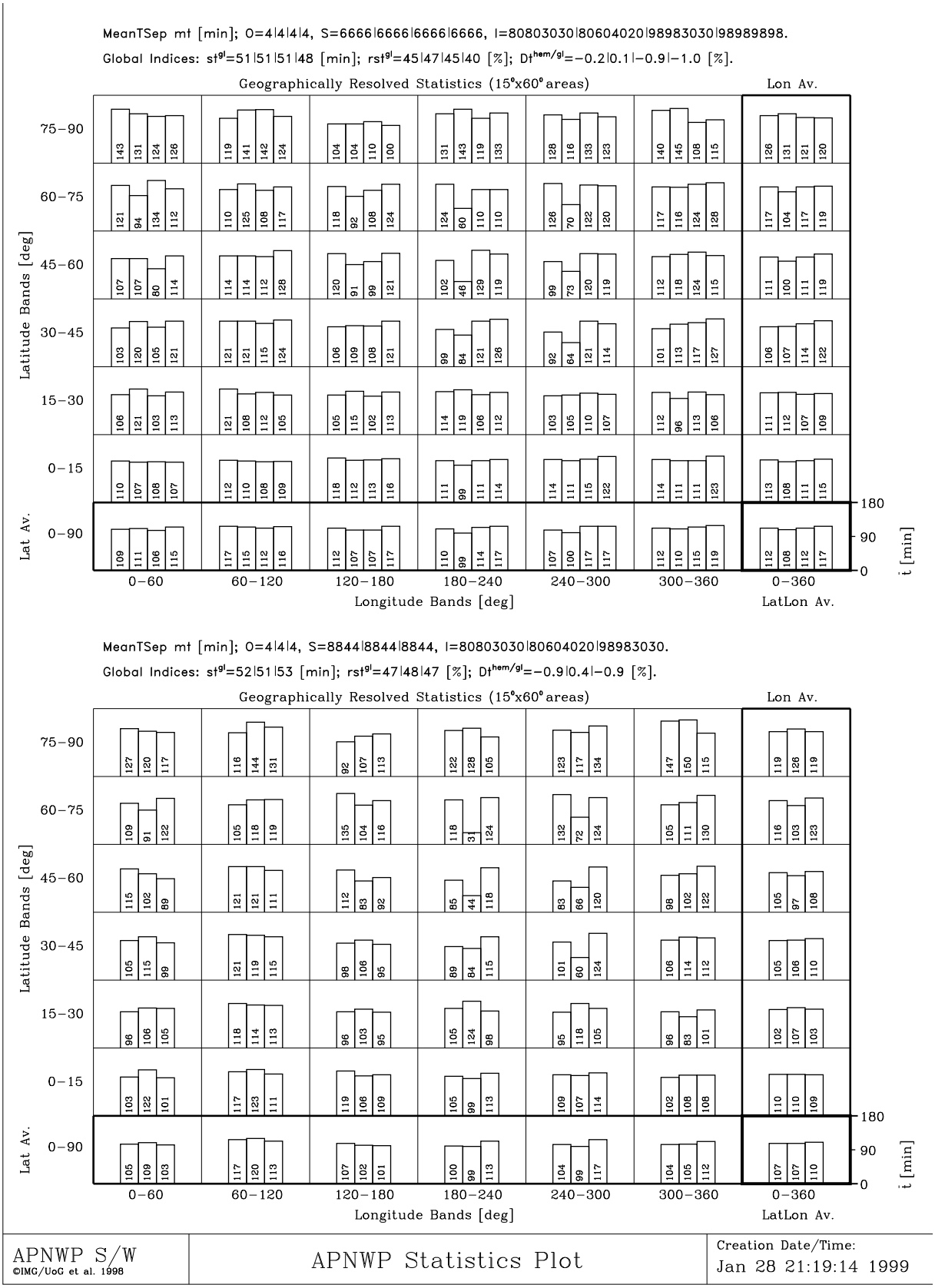

Figure 44: Mean time separation $\overline{t}$ $[min]$.

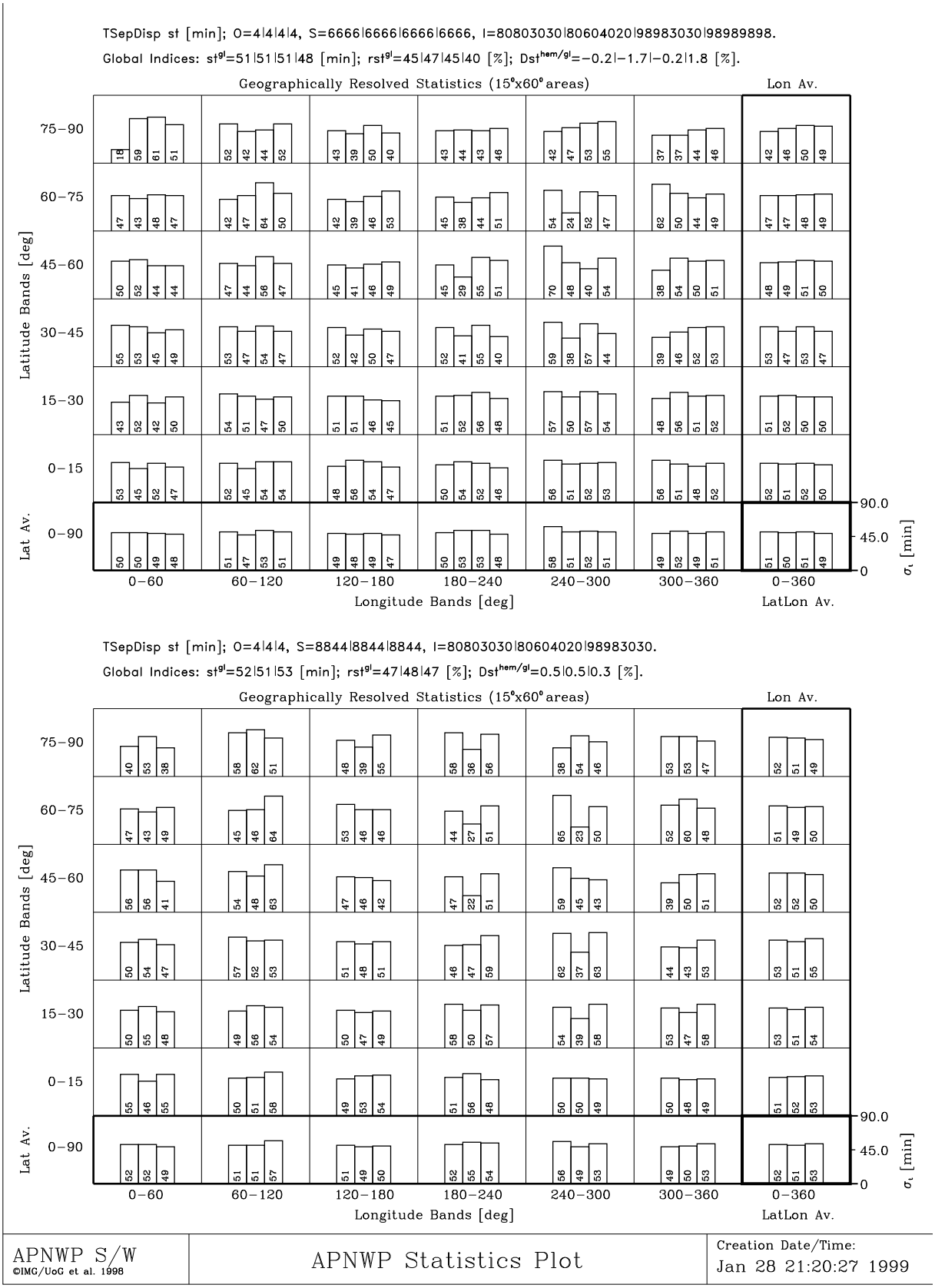

Figure 45: Time separation dispersion σ_t $[min]$.

3.2 Conclusions on Mission Scenarios

We have, after reviewing and defining observational requirements for NWP, described how we designed a GNSS constellation mission scenario study, how we computed about 60 different relevant simulations, and how we analyzed the results of these different scenarios. Beginning with 21 simple satellite constellation scenarios (the so-called basic cases), we increased the complexity of the satellite constellations, in our 39 real scenario simulations, to configurations of up to 24 satellites orbiting simultaneously in 4 different orbital planes with different inclinations and nodes for the orbits.

Before starting with the satellite constellation simulations, relevant statistical performance measures were defined, including the number of occultation events per unit area, the mean distance between neighbor events, the rms dispersion of distances about this mean, the mean time separation of neighbor events, and the rms dispersion of time separations about this mean, respectively. For getting some expertise on the different influences of typical input variables (mainly orbital elements) on performance measures we first investigated so-called basic scenarios. This provided guidance, besides predefined generic requirements and general constraints which we introduced at the beginning of the report, for the design of more realistic scenarios. These were designed to sensibly sample the basin space of LEO constellations in view of preparing good candidate constellations for a subsequent selection of a few constellations to be used as basis for NWP experiments.

We aimed at reasonably sampling the basin space with an as small as possible number of candidate scenarios and finally selected a pool of 39 realistic scenarios spanning a diversity of satellite configurations with satellites spread out over different orbital planes with different inclinations and satellite numbers per orbit and different orbit node geometries. A lot could and can be learned from analyzing and comparing the individual results of the real scenarios: We provide the results in this report in highly visualized form in an atlas-like manner so that the reader can thoroughly inspect and intercompare the results of all scenarios in all statistical measures computed.

A straightforward result of the scenarios was the confirmation that there is a near linear dependence of the average occultation event number density on the size of the constellation. The regional details in number density are highly dependent on constellation layout, though, as is well illustrated by our result figures. Given the number of satellites, the largest single constellation design action to take is using sensibly placed multiple orbital planes for the satellites (also somewhat straightforward). An interesting result was that the mean time separation between neighbor events is roughly independent of constellation size. Concerning mean distance between neighbor events, the largest constellation considered (24 satellites) was definitely able to entirely fulfil the (geographic space/time) observational requirements set out at the beginning of the study.

Another feature of interest in the results is the significant influence of differential orbital drift, in case of orbit planes with different inclinations. It makes quite a difference whether the constellation is in a phase of maximally aligned nodes (event distribution more uneven) relative to a phase of maximally dispersed nodes (event distribution maximally even). These phases are, for typical constellations, periodically passed with a period of around one month. Larger constellations increasingly reduce the dependence on the state of nodes, with 12 satellites it

is still quite well visible, however.

Regarding equal coverage, we should furthermore note that a pure sun-synchronous satellite constellation should be avoided because such a configuration definitely tends to place too many occultation events at higher latitudes - as we clearly see in both the number density and distance measures - while the lower latitudes are underfilled.

As most favorable scenarios from our analyses of different satellite constellations we can tendatively recommend one of our 24 satellite scenarios with two higher inclined orbit planes and two lower inclined ones (all of them as equally separated in their orbital nodes as possible). These scenarios fulfil the requirements set out at the beginning of the report by using still a relatively small fleet of satellites, and already provide quite homogeneous overall coverage as indicated by the different statistical measures.

In a next step we will make the tendative conclusions presented above more firm by a quantitative performance assessment of realistic scenarios studied here. Based on the quantitative results obtained, we will perform an assessment combining all statistical measures computed, complemented by measures reflecting implementation costs, with a weighting scheme. This will be performed in order to select, from all constellations considered here, a sample of 3-4 best constellations as basis for our NWP experiments.

4 Definition of Mission Scenarios for the Assimilation Experiment

In this section the down selection by means of a quantitative assessment based on objective performance descriptors, from the 21 candidate constellations to a small best sample of constellations, which can subsequently be used as representative test missions the for Observation System Simulation Experiments (OSSE) is shown.

Having the significant resource demands required for a realistic OSSE in mind, a maximum of four OSSE test missions can finally be defined. These four test missions should include in any case a single sun-synchronuous satellite mission, as a fixed basic zero-level reference case. This reference case is to mimic the situation of having just a single GNSS receiver for atmospheric sounding (GRAS) available in orbit, e.g. the Metop/GRAS instrument scheduled for launch in 2005 with the Metop-1 satellite of the European Polar System (EPS).

Given these generic constraints, a set of three constellation cases is selected, which we recommend as test missions for the OSSE study.

Section 5 introduces the objective performance descriptors, a penalty function approach, on which the quantitative assessment of 21 candidate constellations is based. The results of the assessment are worked out and discussed in section 6 and in section 7 we finally perform our actual definition of best constellations for the test mission.

5 Mission Scenario Definition Constraints

General Constraints: A set of maximally four OSSE test missions can be performed. This shall include a single sun-synchronuous satellite case as zero-level baseline, leaving three actual constellations to be defined. We impose the further constraint, that at least one 6-satellite, one 12-satellite, and one 24-satellite constellation shall belong to the OSSE test mission sample. Thus we will select a set of three constellations, comprising one 6-sat, one 12-sat, and one 24-sat constellation.

The statistical performance measures of the 39 (3 x 13) scenarios, quantitatively assess them by computing objective performance descriptors – including a single total figure-of-merit – for each of the 21 (3 x 7) candidate constellations, is used. The 3 x 7 constellations based on their descriptors and extract 3 final cases (3 x 1, i.e., one 6-sat, one 12-sat, one 24-sat), or alternative sets of 3 final cases are rated thereafter.

5.1 The Penalty Function Concept

We employed a penalty function concept for defining sensible integral performance descriptors for the candidate constellations, based on the information we have in form of the statistical performance measures given.

This is an attractive concept since it allows, for each of the 39 input scenarios, to sensibly and very effectively collapse the information contained in the extremely high-dimensional parameter space of the statistical performance measures into a low-dimensional penalty function space, i.e. a small number of scalar figures-of-merit, finally even a single figure-of-merit in form of a total penalty value for each given constellation. As well this methode allows for an effective connection of the high number of non-linear dependencies in the orbit setup.

Such a dimension-reduction mapping is highly ambiguous, however, and there exists basically an infinite number of possibilities to define penalty functions as functions of all the statistical measures information available.

It is important to note that the choice below is what we found a sensible penalty definition given our experience in the field. In other words, though the subsequent assessment (section 6) is indeed performed objectively based on the defined performance descriptors, the setup of the objective framework itself (here our penalty function definitions) is always based on (subjective) experience. This should kept in mind when judging the objective assessment results.

5.2 Definition of Penalty Functions

We defined the following seven penalty functions as our basic objective performance descriptors:

- (1) Sampling Requirements Penalty J_d

- (2) Mission Cost Penalty J_c
- (3) Event Number Penalty J_N
- (4) Unequal Coverage Penalty J_{σ_N}
- (5) Geographic Irregularity Penalty J_{σ_d}
- (6) Time Separation Penalty J_t
- (7) Time Irregularity Penalty J_{σ_t}

Furthermore, we defined a Total Penalty, J_{tot}, which shall be a (user-)weighted and normalized sum of the 7 specific penalties (1) – (7).

The names of the penalties were chosen to be suggestive of what aspect of constellation performance they penalize, i.e. a penalty value for a given aspect will be the lower the better this aspect is fulfilled by a constellation scenario. To give one or two examples: An Event Number Penalty will certainly be higher for a 6-sat constellation than for a 24-sat constellation, since the latter, favorably, furnishes much more events per unit area and unit time. For a sensible Mission Cost Penalty it is clearly the other way round.

The quantitative formulation of the penalty functions for the alltogether eight penalties listed above, was chosen as follows:

- (1) Sampling Requirements Penalty J_d:

$$J_d = f_d F_d; \quad F_d = \frac{\overline{d}^{gl}}{(\overline{d}_{ref})}; \quad (\overline{d}_{ref}) = 300 \text{ [km/6hrs]}; \quad f_d = 1 \text{ (baseline)}$$

  The input statistical measure to J_d is $\bar{d}^{gl}$, the global average mean distance between neighbor occultation events per unit time. The factor f_d allows to weigh J_d relative to the other six specific penalties.

- (2) Mission Cost Penalty J_c:

$$J_c = f_c F_c; \quad F_c = g_{sat}(1 - g_{sunsync}\frac{n_{sunsyncsat}}{n_{sat}})\frac{n_{sat}}{(n_{ref})} + g_{orb}\frac{n_{orbplanes}}{(n_{orbref})};$$

$$g_{sat} = 1/4; \quad g_{sunsync} = 1/4; \quad g_{orb} = 1/2;$$

$$(n_{ref}) = 6 \text{ [sats]}; \quad (n_{orbref}) = 2 \text{ [planes]}; \quad f_c = 1 \text{ (baseline)}$$

  The input measures to J_c are the number of sats in the constellation, n_{sat}, the number of sun-synchronuous sats in the constellation, $n_{sunsyncsat}$, and the number of orbital planes involved, $n_{orbplanes}$. The factor f_c allows to weigh J_c relative to the other six specific penalties.

- (3) Event Number Penalty J_N:

$$J_N = f_N F_N; \quad F_N = \frac{(N_{ref})}{N^{gl}}; \quad (N_{ref}) = 5 \ [/(1000\text{km}^2)/6\text{hrs}]; \quad f_N = 1 \ \text{(baseline)}$$

The input statistical measure to J_N is N^{gl}, the global average number of occultation events per unit area and time. The factor f_N allows to weigh J_N relative to the other six specific penalties.

- (4) Unequal Coverage Penalty J_{σ_N}:

$$J_{\sigma_N} = f_{\sigma_N} F_{\sigma_N}; \quad F_{\sigma_N} = \frac{\tilde{\sigma}_N^{gl}}{(\tilde{\sigma}_{N,ref})}; \quad (\tilde{\sigma}_{N,ref}) = 33 \ [\%]; \quad f_{\sigma_N} = 1 \ \text{(baseline)}$$

The input statistical measure to J_{σ_N} is $\tilde{\sigma}_N^{gl}$, the (relative) global coverage inhomogeneity index. The factor f_{σ_N} allows to weigh J_{σ_N} relative to the other six specific penalties.

- (5) Geographic Irregularity Penalty J_{σ_d}:

$$J_{\sigma_d} = f_{\sigma_d} F_{\sigma_d}; \quad F_{\sigma_d} = g_{\tilde{\sigma}_d} \frac{\tilde{\sigma}_d^{gl}}{(\tilde{\sigma}_{d,ref})} + g_{\sigma_d^A} \frac{\sigma_d^{A,gl}}{(\sigma_{d,ref}^A)}; \quad g_{\tilde{\sigma}_d} = 1/2; \quad g_{\sigma_d^A} = 1/2;$$

$$\sigma_d^{A,gl} = \left[\frac{1}{N_A - 1} \sum_{i=1}^{N_A} \left(\sigma_{d,i}^A - \sigma_d^{gl} \right)^2 \right]^{\frac{1}{2}}; \quad (\tilde{\sigma}_{d,ref}) = 33 \ [\%]; \quad (\sigma_{d,ref}^A) = 100 \ [\text{km}];$$

$$f_{\sigma_d} = 1 \ \text{(baseline)}$$

The input statistical measures to J_{σ_d} are σ_d^{gl} and $\tilde{\sigma}_d^{gl}$, respectively, the (absolute and relative) global geographic irregularity indices, and the $\sigma_{d,i}^A$ values, the sampling distance dispersions for the 36 lat x lon cells. The factor f_{σ_d} allows to weigh J_{σ_d} relative to the other six specific penalties.

- (6) Time Separation Penalty J_t:

$$J_t = f_t F_t; \quad F_t = \frac{\overline{t}^{gl}}{(\overline{t}_{ref})}; \quad (\overline{t}_{ref}) = 60 \ [\text{min}/6\text{hrs}]; \quad f_t = 1 \ \text{(baseline)}$$

The input statistical measure to J_t is $\bar{t}^{gl}$, the global average mean time separation between neighbor occultation events per unit time. The factor f_t allows to weigh J_t relative to the other six specific penalties.

- (7) Time Irregularity Penalty J_{σ_t}:

$$J_{\sigma_t} = f_{\sigma_t} F_{\sigma_t}; \quad F_{\sigma_t} = g_{\tilde{\sigma}_t} \frac{\tilde{\sigma}_t^{gl}}{(\tilde{\sigma}_{t,ref})} + g_{\sigma_t^A} \frac{\sigma_t^{A,gl}}{(\sigma_{t,ref}^A)}; \quad g_{\tilde{\sigma}_t} = 1/2; \quad g_{\sigma_t^A} = 1/2;$$

$$\sigma_t^{A,gl} = \left[\frac{1}{N_A - 1} \sum_{i=1}^{N_A} \left(\sigma_{t,i}^A - \sigma_t^{gl} \right)^2 \right]^{\frac{1}{2}}; \quad (\tilde{\sigma}_{t,ref}) = 33 \ [\%]; \quad (\sigma_{t,ref}^A) = 20 \ [\text{min}];$$

$$f_{\sigma_t} = 1 \ \text{(baseline)}$$

The input statistical measures to J_{σ_t} are σ_t^{gl} and $\tilde{\sigma}_t^{gl}$, respectively, the (absolute and relative) global time irregularity indices, and the $\sigma_{t,i}^A$ values, the time separation dispersions for the 36 lat x lon cells. The factor f_{σ_t} allows to weigh J_{σ_t} relative to the other six specific penalties.

- Total Penalty J_{tot}:

$$J_{tot} = \frac{1}{7}\sum_{k=1}^{7} J_k = \frac{1}{7}\sum_{k=1}^{7} f_k F_k, \quad k \in \{d, c, N, \sigma_N, \sigma_d, t, \sigma_t\}$$

or written more explicitely

$$\begin{aligned} J_{tot} &= J_d + J_c + J_N + J_{\sigma_N} + J_{\sigma_d} + J_t + J_{\sigma_t} \\ &= f_d F_d + f_c F_c + f_N F_N + f_{\sigma_N} F_{\sigma_N} + f_{\sigma_d} F_{\sigma_d} + f_t F_t + f_{\sigma_t} F_{\sigma_t} \end{aligned}$$

We have implemented this penalty function formulation in a computational routine (IDL program), with the weighting factors f_k being user-definable input parameters; the baseline setting is unity for all f_k's as indicated above. It is up to the assessment responsible to specify the weighting among the specific penalties; the relative weighting supplied is automatically normalized to unity by enforcing $\frac{1}{7}\sum_{k=1}^{7} f_k = 1$.

5.3 Computation of Performance Descriptors

We computed the eight performance descriptors (penalty values) for all 39 realistic scenarios. In practice, after the weighting factors f_k are defined by the user of the computational routine referred to above, the routine normalizes them and then automatically produces all values for each of the 39 scenarios.

For the assessment results reported below we set the f_k's such that we assigned equal weights of $f_k = 1.15$ to all penalties except the geographic irregularity and time irregularity penalties, J_{σ_d} and J_{σ_t}, respectively. To the latter we assigned roughly half the weight of the others ($f_{\sigma_d} = f_{\sigma_t} = 0.62$). This weighting reflects that we consider the two latter penalties more of 2^{nd} order importance relative to the other five. This is well justified given that these are the two descriptors which are just dispersion measures of the 1^{st} order descriptors J_d and J_t (note that J_{σ_N} is a dispersion measure for the 0^{th} order descriptor J_N, however). We decided not to impose any further more subtle weighting due to lack of convincing rationale.

Using this weighting we computed the eight descriptors, the J_k's and J_{tot}, for the 39 scenarios. The needed input parameters, namely $\bar{d}^{gl}$, n_{sat}, $n_{sunsyncsat}$, $n_{orbplanes}$, N^{gl}, $\tilde{\sigma}_N^{gl}$, σ_d^{gl}, $\tilde{\sigma}_d^{gl}$, $\sigma_{d,i}^A$ ($i = 1, \ldots, N_A$; $N_A = 36$), $\bar{t}^{gl}$, σ_t^{gl}, $\tilde{\sigma}_t^{gl}$, and $\sigma_{t,i}^A$ ($i = 1, \ldots, N_A$; $N_A = 36$), were available from the result files containing the statistical measures and were read in from there.

Based on the descriptors for the 39 (3 x 13) scenarios, the descriptors for the 21 (3 x 7) actual constellations had to be obtained. Recall that for all constellations, except the 3 (3 x 1) pure sun-sync ones, we had different inclinations of orbital planes involved and we thus investigated both maximal node alignment ($\Delta\Omega_{min} = 0\,^\circ$) and maximal node dispersion ($\Delta\Omega_{max} = 90 \text{ or } 45\,^\circ$) scenarios, respectively, for these alltogether 18 (3 x 6) constellations.

We computed the eight descriptors, generically denoted as J_l's, for the 18 constellations as

$$J_l = \frac{1}{2}(J_l^{\Delta\Omega_{max}} + J_l^{\Delta\Omega_{min}}); \quad l \epsilon \{d, c, N, \sigma_N, \sigma_d, t, \sigma_t, tot\},$$

i.e., we simply averaged the results of the two node separation scenarios of each mixed-inclination constellation. No such further treatment was of course needed for the descriptors of the three pure sun-sync constellations as these J_l's directly correspond to single scenario results.

Should the J_l's, most notably the total figure-of-merit J_{tot}, not lead to an unique conclusion on three final constellations, we have the option to proceed with invoking more sophisticated descriptors than the scalar J_l's. To next level in complexity these are vector descriptors, i.e., distributions of statistical measures over some coordinate. We find it sensible, from an observational and user requirements point of view, to consider as vector descriptor of primary relevance the number of occultation events per unit area and unit time vs. geographic latitude, which we denote $N(\varphi)$.

As described in section 6 below, the J_l's indeed are not fully conclusive (section 6.2) and we thus have used $N(\varphi)$ histogram functions for an assessment refinement (section 6.3). The simulations and the visualization of the $N(\varphi)$ histograms have been performed with the Mission Analysis/Planning functionality of the End-to-end GNSS Occultation Simulator (EGOPS) software tool on which more information can be found, e.g., in [KIRC96] and [KIRC98].

6 Assessment Results and Discussion

6.1 Summary of Mission Scenarios

As a convenient reference, we recall in Table 4 below the main characteristics of the 39 realistic mission scenarios. Table 4 is ordered by mission Scenario No. and constellation Case No., respectively, and is naturally partitioned into 3 groups of 13 scenarios / 7 actual constellations, one group for each the 6-sat, the 12-sat, and the 24-sat constellations. For each constellation, the number of orbit planes (2 or 4), the number of satellites per plane (2, 3, 4, 6, or 8; e.g., 3-3 for 3 sats in each of two planes), and the inclinations of the planes (30, 40, 55, 60, 80, or 98 °; e.g., 80-30 for one 80 ° and one 30 ° plane) are indicated. Furthermore, for each scenario, the node separation (0, 45, or 90 °) is given. For details on these mission scenarios, the rationale behind their selection, and the performance statistics results.

6.2 Constellation Performance Assessment

We have produced the assessment results for the 39 scenarios/21 constellations of Table 4, i.e., we computed all defined performance descriptors J_l ($l \epsilon \{d, c, N, \sigma_N, \sigma_d, t, \sigma_t, tot\}$) according to the description in section 5.3 above.

Scenario No.	**Case No.**	**Orbit Planes**	**Satellite No.**	**Inclinations** [°]	**Node Sep.** [°]
1	1	2	3-3	80-30	90
2					0
3	2	2	4-2	80-30	90
4					0
5	3	2	3-3	80-55	90
6					0
7	4	2	4-2	80-55	90
8					0
9	5	2	3-3	98-30	90
10					0
11	6	2	4-2	98-30	90
12					0
13†	7	2	3-3	98-98	90‡
14	8	2	6-6	80-30	90
15					0
16	9	2	8-4	80-30	90
17					0
18	10	2	6-6	80-55	90
19					0
20	11	2	8-4	80-55	90
21					0
22	12	2	6-6	98-30	90
23					0
24	13	2	8-4	98-30	90
25					0
26†	14	2	6-6	98-98	90‡
27	15	4	6-6-6-6	80-80-30-30	45
28					0
29	16	4	8-8-4-4	80-80-30-30	45
30					0
31	17	4	6-6-6-6	80-60-40-20	45
32					0
33	18	4	8-8-4-4	80-60-40-20	45
34					0
35	19	4	6-6-6-6	98-98-30-30	45
36					0
37	20	4	8-8-4-4	98-98-30-30	45
38					0
39†	21	4	6-6-6-6	98-98-98-98	45‡

Table 4: Main characteristics of the realistic scenarios satellite constellations.

Notes: (†) For pure sun-sync cases only one scenario exists (cf. section 5.3).
(‡) For pure sun-sync cases the orbit node separation is always fixed

to maximum spread.

Figure 46 conveniently visualizes the assessment results in a single Satellite Constellations Performance Assessment plot. The left-hand column shows the results for all scenarios, ordered by the Scenario No. of Table 4, the right-hand column for all actual constellations, ordered by the Case No. of Table 4. Each column shows the values of all eight J_l's ($l \in \{d, c, N, \sigma_N = sN, \sigma_d = sd, t, \sigma_t = st, tot\}$), i.e., the seven specific penalties, J_k, and their weighted, normalized sum, J_{tot}. The J_k's themselves are shown for clarity without weighting ($J_k = F_k$) but the weighting factors f_k applied when producing the weighted sum J_{tot}, shown in the bottom subpanels, are indicated in each J_k-subpanel.

A closer inspection of Figure 46 is quite instructive for learning about how the different performance descriptors depend on given scenarios and particularly given constellations, and how the different descriptors add up to the final single figure-of-merit J_{tot}.

The Sampling Requirements Penalty, J_d, and the Event Number Penalty, J_N, respectively, are counteracted by the Mission Cost Penalty, J_c. This is quite expected since all these depend most sensitively on the constellation size, with the Mission Costs depending on it in a reverse manner, i.e., bigger constellations being most heavily penalized.

The Unequal Coverage Penalty, $J_{\sigma_d=sN}$, shows a less straightforward behavior, it is least penalized by constellations with some near-optimal spread in orbital planes and their inclinations.

Interestingly, the Time Separation Penalty, J_t, is roughly unaffected by total constellation size, it even shows a slight penalty increase towards bigger constellations. Apparently bigger constellations tend to slightly more intermingle in UT individual occultation events due to closer packing of satellites in space, which statistically makes neighbor events happen slightly more separated in UT.
A salient feature of the distance and time dispersion penalties, $J_{\sigma_d=sd}$ and $J_{\sigma_t=st}$, is that they are somewhat correlated in their behavior and that they tend, in particular $J_{\sigma_d=sd}$, to put relatively high penalty to constellations with most unfavorable differences between maximal node alignment and maximal node dispersion situations.

The Total Penalty, J_{tot}, exhibits comparatively flat dependence on the constellation cases, which is perhaps somewhat surprising at first glance. In other words, this single figure-of-merit does not sharply separate at a glance specific best constellations from other much worse constellations. This is not too surprising, however, considering that J_{tot} is a sum of a series of competing and mutually counteracting aspects and that we have selected a sample of 21 constellations which are already fairly good compared to arbitrary selections from the basin space of constellation options. The histogram $J_{tot}(Case\ No.)$ should basically behave rather flat if not high unequal weighting is applied to stress one or very few specfic aspects J_k, which we did not consider appropriate for lack of convincing rationales.

It is nevertheless sensible, and the correct way to go based on such a quantitative assessment, to take the indication of least-penalty in $J_{tot}(Case\ No.)$ as pointing to the most favorable constellations in the candidate sample. It is the bottom-right subpanel of Figure 46 giving this information. As we have, according to the constraints set out in section 5, to select

one case from group 1–7 (6 sats), one from 8–14 (12 sats), and one from 15-21 (24 sats), respectively, the least-penalty criterion suggests a first downselection to cases 5-7 (6 sats), 12–14 (12 sats), and 16 & 19–20 (24 sats), respectively. This were a downselection to nine cases and we can go back to Table 4 to see which constellations have been drawn.

It is important to note that somewhat different weighting might lead to a somewhat different downselection so this result on its own is certainly not sufficient decision support for a firm and final selection. More generally speaking it seems sensible to conclude from Figure 46 that, for each of the 3 groups (6, 12, or 24 sats), the last three cases (5–7, 12–14, 19–21) and the second case (2, 9, 16) are cases of interest for the final sample.

Since Figure 46, however, definitely does not lead to an unique conclusion on three constellations, we proceed, as outlined at the end of section 5 above, with invoking a performance descriptor at the next level of complexity, i.e., the vector descriptor $N(\varphi)$. We use $N(\varphi)$ histogram functions for an assessment refinement.

6.3 Assessment Refinement by Latitudinal Statistics

The half-way downselection to three to four cases per group performed above suggests, via checking with Table 4, that the cases of interest are those with 80 ° and 30 ° inclined planes and fewer satellites in the lower-inclined plane(s) (2, 9, 16), or with 98 ° (sun-sync) and 30 ° inclined planes (5, 6, 12, 13, 19, 20), or pure sun-sync cases (7, 14, 21).

We shall study these cases here closer in terms of the vector descriptor $N(\varphi)$, which we ideally expect to show independence of N on φ (equal coverage). We will discuss only the results for the medium group with the 12-sat constellations (cases 9, 12–14), the $N(\varphi)$ behavior of which is well representative for the other two groups with 6-sats and 24-sats.

Figures 47 and 48 illustrate the $N(\varphi)$ histogram functions for the cases of interest of the 12-sat group. The header of each panel is indicating which case/scenario is shown. Figure 47 shows case 9 (top panels) and case 14 (bottom panel), respectively, while Figure 48 shows case 12 (top panels) and case 13 (bottom panels).

Explained in more detail, the $N(\varphi)$ shown is the number of events per unit area vs. 5 °-latitude bins as accumulated globally over 12 hours assuming that setting and rising occultations from a nominal GPS and GLONASS transmitter constellation (together 48 satellites) were collected with receiver antennae field-of-views spanning approximately ± 45 ° about the LEO orbit plane.

From Figures 47 and 48 it is obvious that $N(\varphi)$ of case 14 is the most unfavorable of all four cases. Thus we can consider this pure sun-sync case definitely less attractive than the other three cases. Furthermore, from Figure 48 it is seen that $N(\varphi)$ of case 12, the 98 °/30 ° inclination case with an equal number of satellites in both planes, is less favorable than that of case 13, the 98 °/30 ° inclination case with fewer satellites in the lower inclined plane. Thus case 12 is less attractive than case 13. Comparing, in turn, case 13 with case 9, the 80 °/30 ° inclination case with fewer satellites in the lower inclined plane, indicates that $N(\varphi)$ of case 9 is the most favorable one of all cases considered.

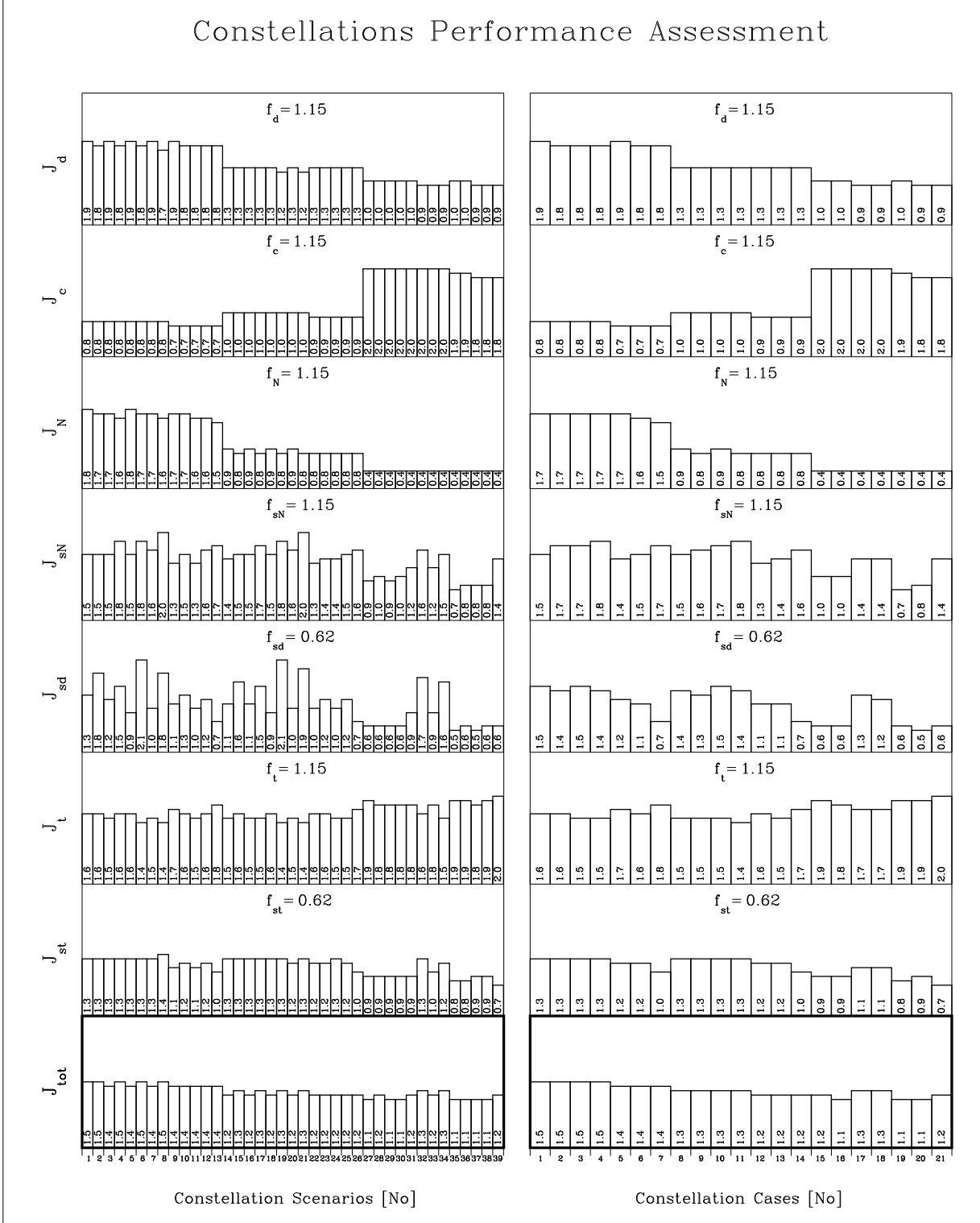

Figure 46: Satellite Constellations Performance Assessment.

We can summarize that, in terms of the vector descriptor $N(\varphi)$, the most attractive 12-sat constellation is represented by case 9 and the second best by case 13. Since the $N(\varphi)$ behavior is essentially invariant under changes in constellation size, it is justified to generalize this result by stating that the descriptor $N(\varphi)$ suggests that the final sample of constellations should either contain the 80 °/30 ° cases 2, 9, and 16 (best choice), or the 98 °/30 ° cases 6, 13, and 20 (second best choice). Note that both choices have one-third of all satellites in the 30 °-plane(s).

Turning back to Figure 46, with now focusing on cases 2/9/16 and cases 6/13/20, we see that the total performance descriptor J_{tot} suggests another order for the two choices than $N(\varphi)$: J_{tot} indicates cases 6/13/20 to be the better choice compared with cases 2/9/16. Being aware of the general limitations inherent in this quantitative assessment as decision support instrument, it seems reasonable to take this ambiguity as indication to keep both sets of cases for recommendation as alternative options.

7 Definition of an OSSE Study Test Mission Set

7.1 Recommendation of Two Test Mission Options

We recall that the general constraints discussed in section 4 and particularly section 5 asked for finally recommending a set, or alternative sets, of four constellations, where a set shall include one Metop/GRAS-like single-satellite case as zero-level baseline, one 6-sat constellation, one 12-sat constellation, and one 24-sat constellation. Given these constraints, we found via the quantitative assessement discussed in section 6 that, in the notion of Table 4, either the set of constellation cases 2/9/16 or the one of cases 6/13/20 should join the single-satellite case in the final sample.

Based on these results we finally recommend as OSSE study test mission set one of the two options summarized respectively in Table 5 and Table 6 below (table format as for Table 4). We close below with a brief discussion of Tables 5 and 6 and conclude that option 1, summarized by Table 5, should be defined as OSSE test mission set. Nevertheless, we recommend that a final decision on which mission set is definitely selected should be taken by group agreement in the OSSE study team at its Simulation Plan Review meeting (scheduled April 1999).

7.2 Discussion of Options and Preferred Mission Set

It is useful to discuss the relative merits of options 1 and 2 from an observational requirements point of view, as, eg., set out in form of the Generic GRAS Observational Requirements in chapter 4 of [GRASSAG98]. Since the OSSE study is directly related to the NWP impact of GNSS occultations one may put distinct emphasis on the Operational Meteorology requirements (as found useful when setting the scene for the study).

A somewhat different perspective were to explicitly also take care of requirements for other purposes, most importantly those of Climate Monitoring and Prediction. We like to take the

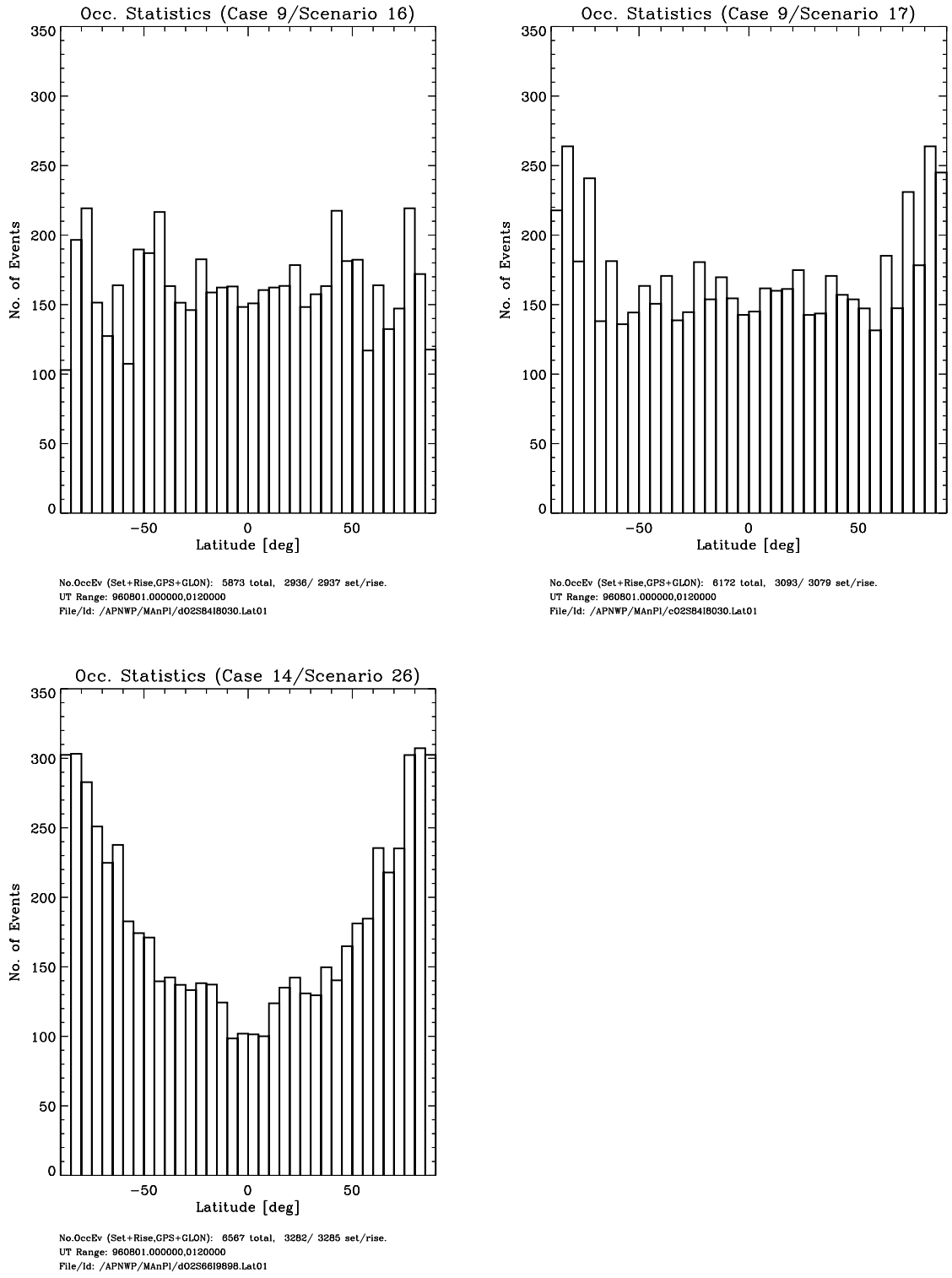

Figure 47: $N(\varphi)$ histograms for constellation cases 9 and 14.

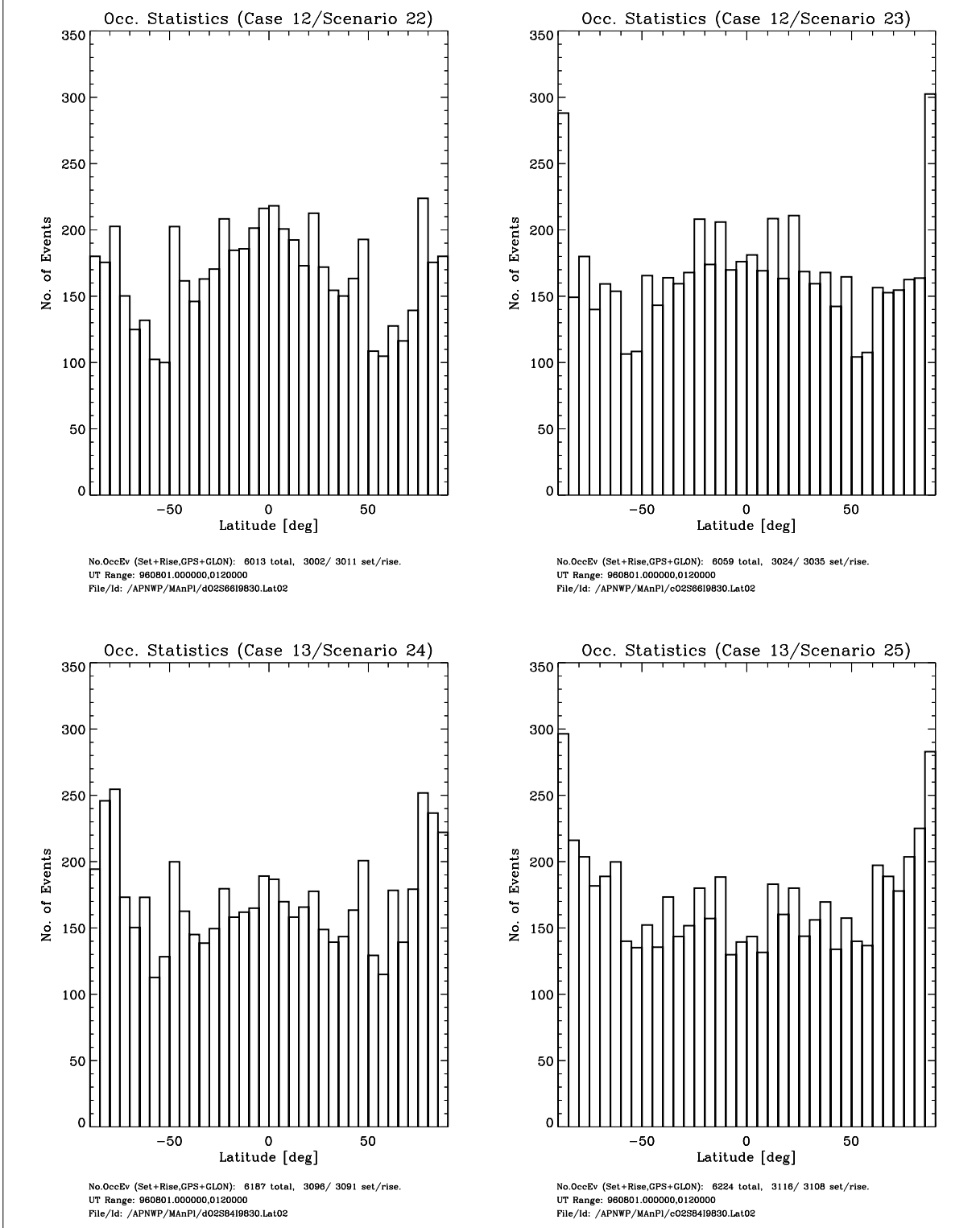

Figure 48: $N(\varphi)$ histograms for constellation cases 12 and 13.

Scenario No.	**Case No.**	**Orbit Planes**	**Satellite No.**	**Inclination(s)** [°]	**Node Sep.** [°]
n/a	lev0†	1	1	98	n/a
3	**2**	2	4-2	80-30	90
4					0
16	**9**	2	8-4	80-30	90
17					0
29	**16**	4	8-8-4-4	80-80-30-30	45
30					0

Table 5: *OSSE test mission set, Option 1* – Baseline case & Constellations with 80 ° / 30 ° inclined orbit planes, one-third of all satellites in 30 ° plane(s).

Notes:

(†) Metop-like sun-sync satellite (zero-level single-sat baseline).

Scenario No.	**Case No.**	**Orbit Planes**	**Satellite No.**	**Inclination(s)** [°]	**Node Sep.** [°]
n/a	lev0†	1	1	98	n/a
11	**6**	2	4-2	98-30	90
12					0
24	**13**	2	8-4	98-30	90
25					0
37	**20**	4	8-8-4-4	98-98-30-30	45
38					0

Table 6: *OSSE test mission set, Option 2* – Baseline case & Constellations with 98 ° / 30 ° inclined orbit planes, one-third of all satellites in 30 ° plane(s).

Notes:

(†) Metop-like sun-sync satellite (zero-level single-sat baseline).

latter perspective since any practical implementation will certainly be one single constellation in space, which shall fulfil multiple-purpose requirements. Thus, even though we seek here an OSSE test mission set, it seems not sensible to discuss constellation options solely on the grounds of Operational Meteorology requirements.

Turning to discussing the two options now, it is clear that they are fairly similar in orbital layout; the difference is just that the high-inclination planes of the constellations are prograde (80 °) and drifting in local time for option 1, while they are retrograde and sun-sync (∼ 98 °) for option 2. Given this similarity it is not too surprising that our quantitative performance descriptors had difficulties to clearly favor one of these options.

One implication of the difference, though, is about 2 °/day more differential drift between high-inclination and low-inclination planes for option 2 compared to option 1. In other words, while option 1 will take about 3 weeks (1.5 weeks for case 16) to change from maximal node alignment to maximal node dispersion, option 2 will take only about 2 weeks (1 week for case 20). Though this is interesting, it seems difficult, from the requirements point of view, to derive from this implication significantly different merits of the options.

Another implication of the difference is that the high-inclination planes are drifting in local

time for option 1 while they reside at fixed local time for option 2. This implies that all high-latitude occultation events (beyond about ± 50–60 °) of option 2 occur at fixed local times throughout the mission, which is of particular significance for the 6-sat and 12-sat cases furnishing a single high-inclination plane. For option 1 it would take about 5 months to sample all local times at high latitudes by a single high-inclination plane, providing full local time sampling about 2.3 times a year. From the requirements point of view we see a clear advantage for option 1 from this implication, particularly in case of the 6-sat and 12-sat constellations, since all requirement classes summarized in [GRASSAG98] prefer sampling of events through different local times at all latitudes. This preference is tendatively least important for operational meteorology, but very important for climate monitoring, prediction, and climatology, and crucially important for ionosphere and space weather applications. This is a strong argument clearly favoring option 1.

A non-scientific advantage of option 2 seems that the majority of the satellites are sun-sync ones which significantly reduces their costs (more simple power supply due to fixed sun angles, etc.). This were a relevant economic argument in favor of option 2. On the other hand, option 1 allows to built all satellites with an identical design – while option 2 would need both a sun-sync and a non-sun-sync type – which also is a cost reduction factor. Without further more detailed cost assessment we cannot decide on this economic question here. Since we take a requirement-oriented point of view, this is not a primary point in this context anyway, however.

From this brief discussion of the relative merits of the two options considered we conclude that we clearly prefer option 1, summarized by Table 5, to be the final set of OSSE study test missions.

A detailed coverage with observations of GRAS data only by the different satellite setups per assimilation day is given in the following figures 49 – 52. It is evident that even the one satellite case show an overall good coverage of the globe. It should be necessary to remind that this observations contain as well rising as setting events and GPS and GLONASS occultations. In the worst case only GPS satellites are available and the number of occultations is only half of the one shown here. For the multi satellite cases this mean a redesign of orbits. Due to the defined extensive procedure given, this is a straight foreward task.

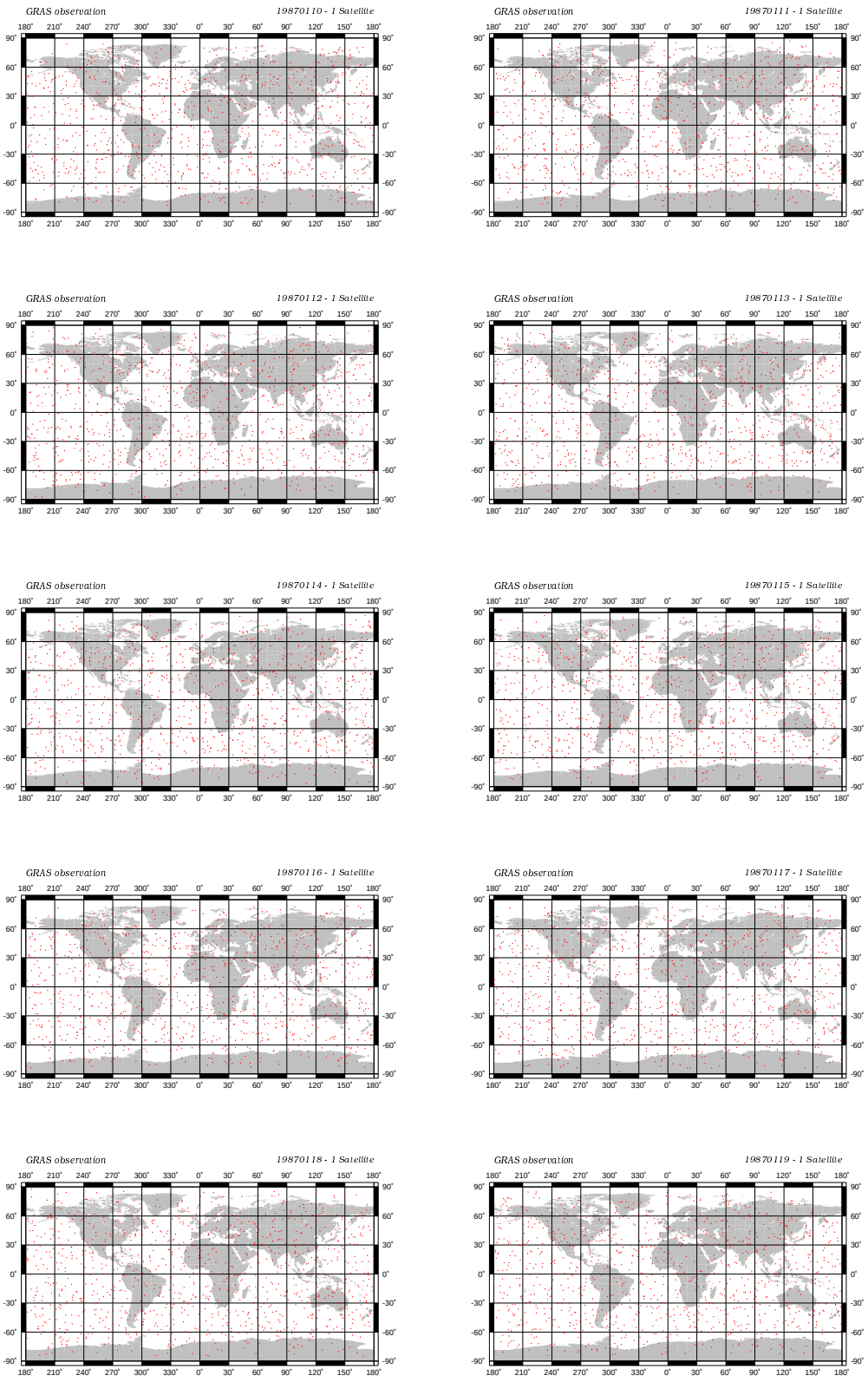

Figure 49: Observation coverage for 24 hour periods during the assimilation periode with 1 satellite

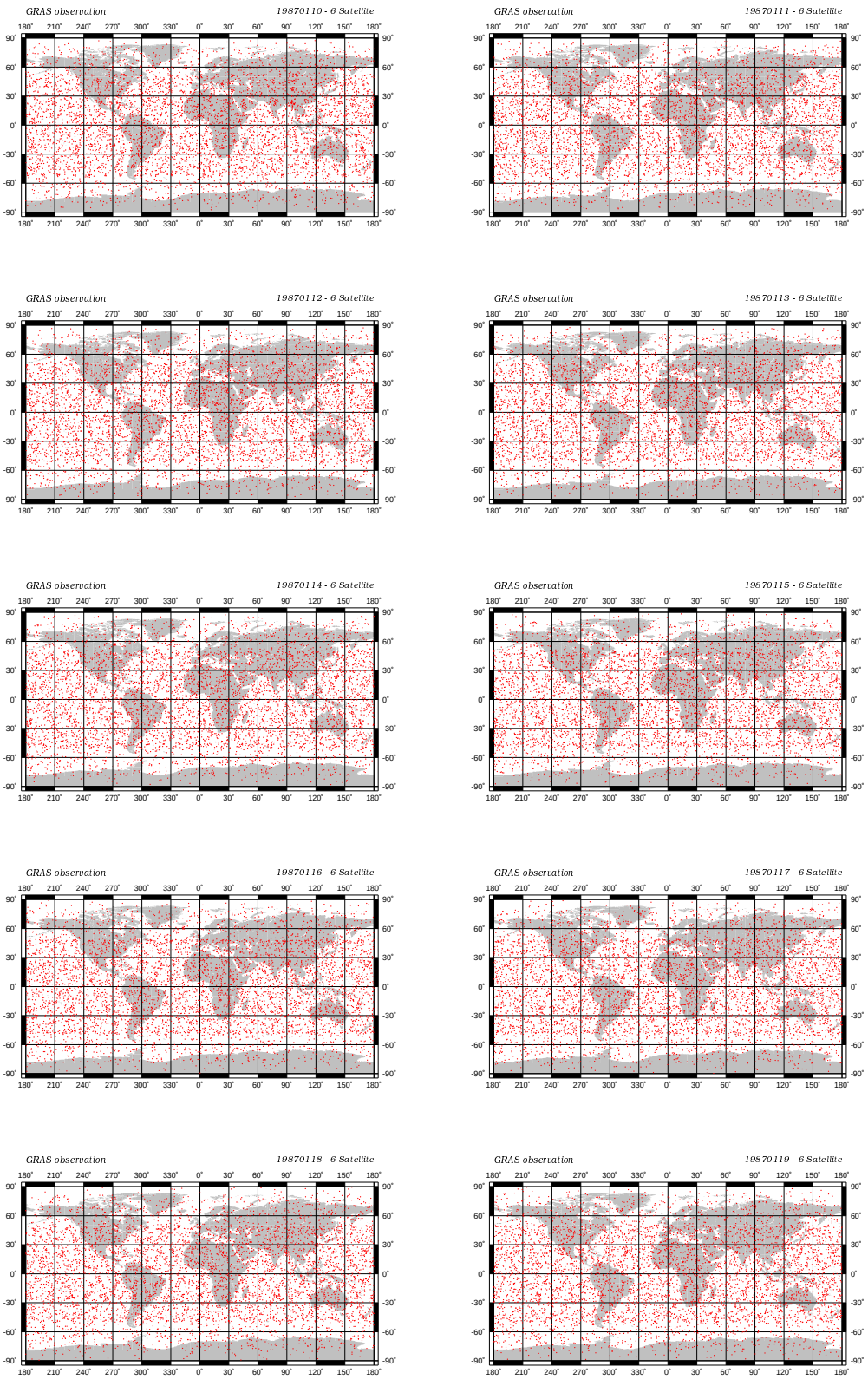

Figure 50: Observation coverage for 24 hour periods during the assimilation periode with 6 satellites

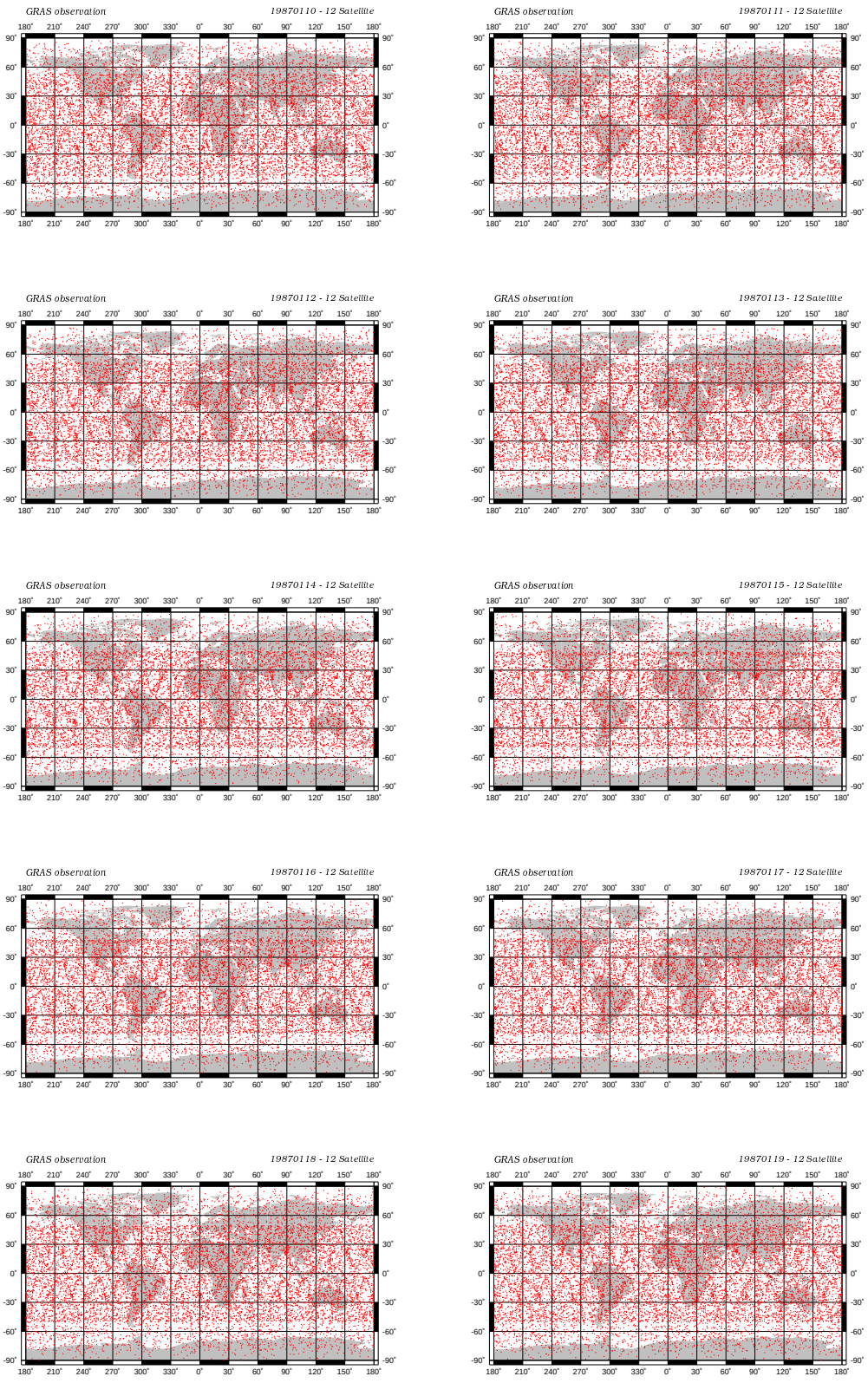

Figure 51: Observation coverage for 24 hour periods during the assimilation periode with 12 satellites

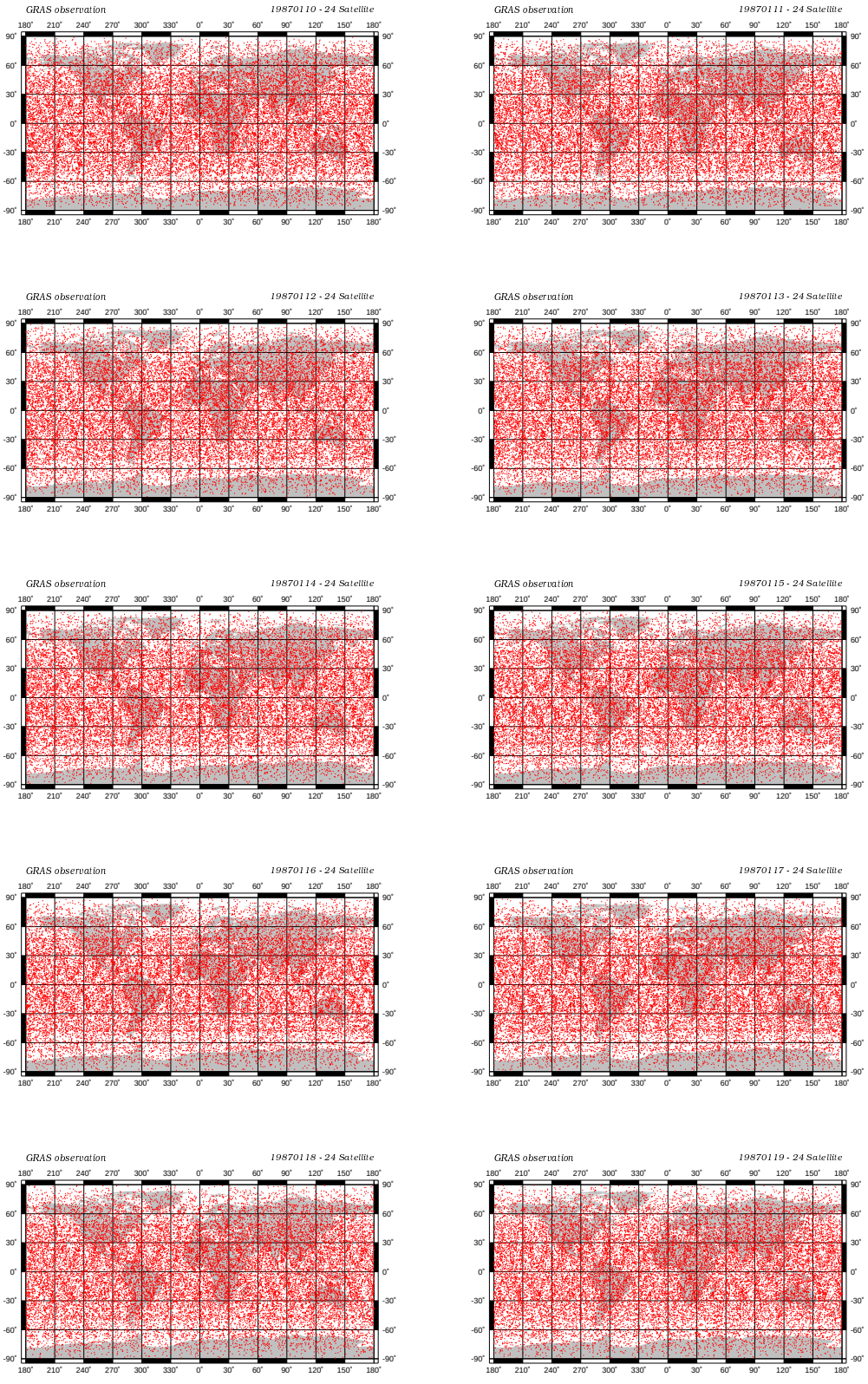

Figure 52: Observation coverage for 24 hour periods during the assimilation periode with 24 satellites

8 Assimilation preparation

Defining the satellite constellation is a very important task in the framework of this study. This has been shown to be very successfull. The occultations are very well distributed in space and time. Major task in the following section is the preparation of the GRAS observations by using the determined satellite constellations and atmospheric fields of the ECMWF Reanalysis. Overall giving a large set of additional observations (see table 7).

Date	1 satellite	6 satellites	12 satellites	24 satellites
10.1.1987	1040	5698	11371	23112
11.1.1987	1059	5693	11399	23242
12.1.1987	1055	5698	11368	23298
13.1.1987	1055	5639	11286	23315
14.1.1987	1061	5595	11248	23296
15.1.1987	1056	5602	11231	23273
16.1.1987	1051	5626	11224	23311
17.1.1987	1044	5638	11239	23316
18.1.1987	1046	5615	11238	23362
19.1.1987	1047	5625	11243	23439

Table 7: Number of occultations per day

This are supposed to be processed by the EGOPS foreward simulation system. We have been evaluating the processing times of the different forward operator (timing given in table 8). Our original plan to do the calculations on the vector supercomputer of DMI failed due to the very poor performance of EGOPS on vectorbased systems.

Ionosphere type	SignPropSimF3D	SignPropSimQ3D	WaveOpticsPropagator
NoIon	4000	460	600-1200
RefIon_UoG	10300	1300	—
Iono3D_UoG	11000	1620	—

Table 8: Computation time in [s] for the different choices/components of the EGOPS forward modelling system

Estimating the computation time for processing the artificial observations shows that to fullfil the time limits of this study we had to parallelize the EGOPS forward modelling system and use the Wave Optics Propagator of EGOPS because the overall computation time is minimized only in this case.

Fortunately the forward modelling system is a well posed parallelization problem. Each occultation can be treated independently. One scheduler can distribute the work to several computing processes. A description of the program structure is given in figure 53.

A substantial amount of time for producing the occultations has been finally provided on the CRAY T3E of the Max-Planck Computing Centre in Garching, about 40 Suns at MPI, and all available Linux PCs. The final code will be incorporated in the EGOPS development version for future studies.

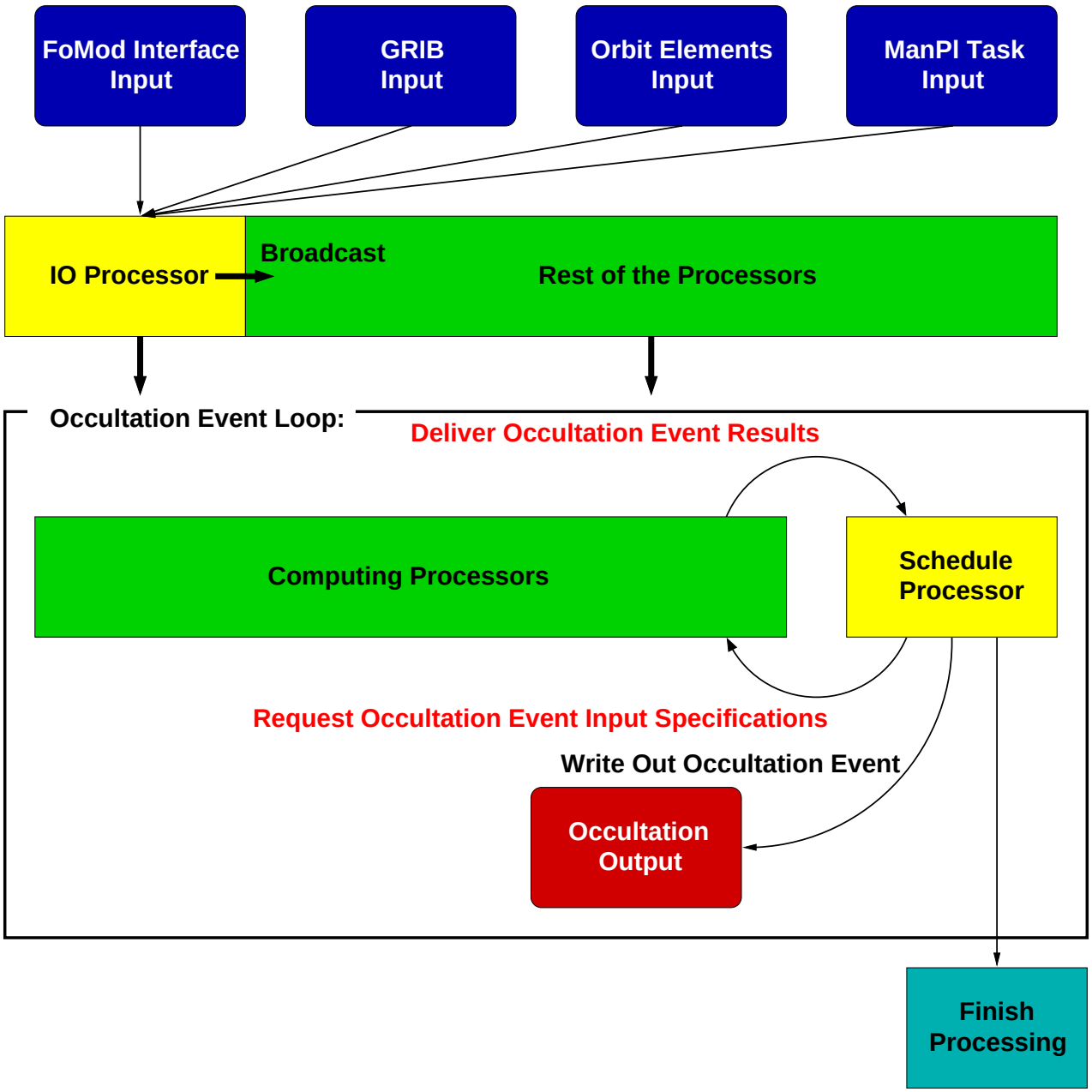

Figure 53: Parallelization strategy for the EGOPS forward modelling system

To justify the decision to use the wave optics propagator we show the results (figure 54) of an intercomparison of two processed data sets. One is the real observed data from a prime time of GPSMET and the second one is the wave optics propagator generated data set. To allow for the ease of comparision both are processed the same way to dry temperature.

Beside the necessary GRAS observations and the conventional observations used (quality checked and blacklisted) by the ECMWF Reanalysis, the initial atmospheric state of ECHAM4 has to be as close as possible to the Reanalysis. The procedure to obtain this state is given in the next section.

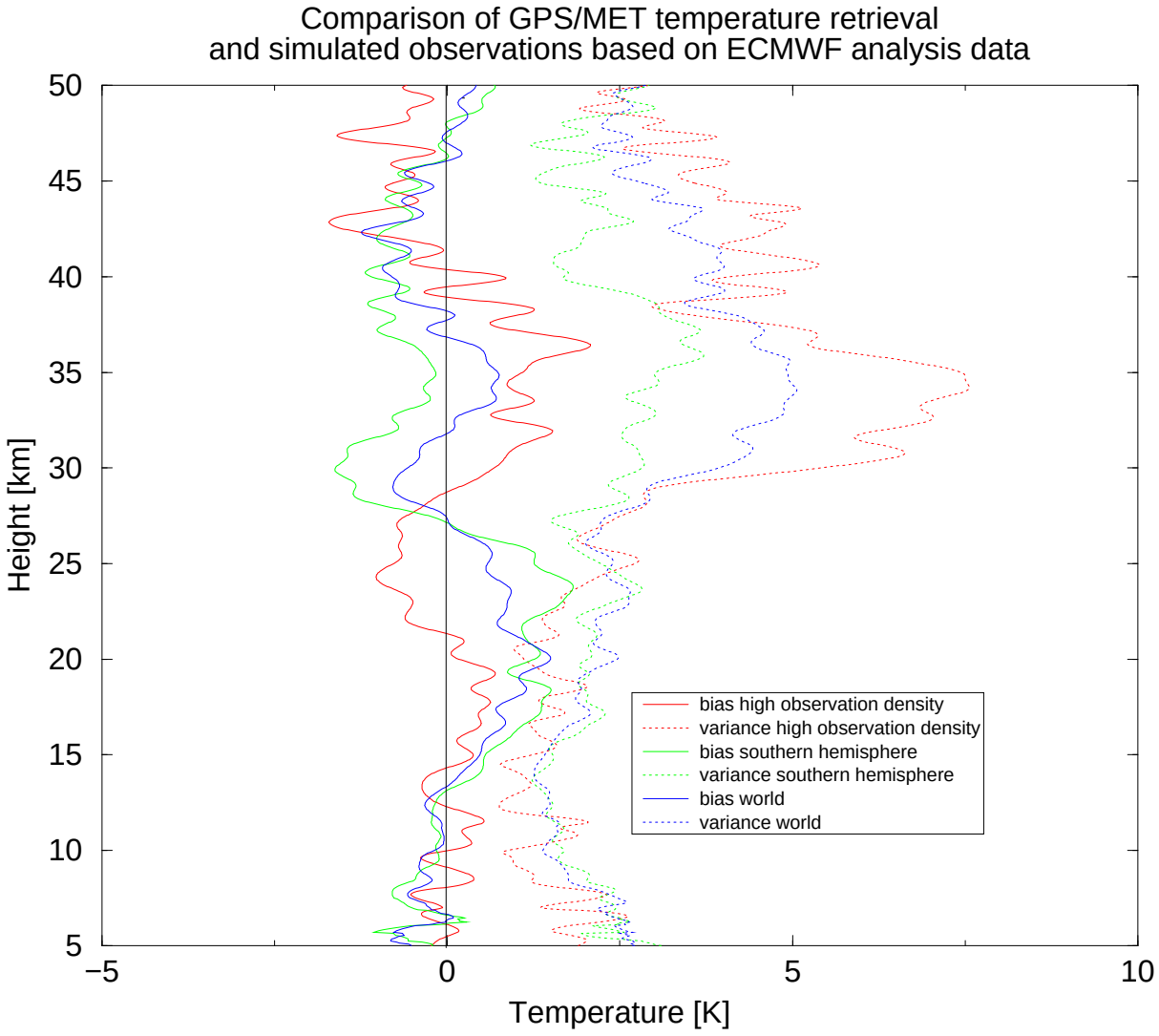

Figure 54: Intercomparison of the performance of the wave optics propagator (ECMWF based fields used) with the GPSMET observations.

9 Preparing the models state - a nudging application

To force the model trajectory as close as possible to the real atmospheric state at the beginning of the assimilation time periode we use the nudging technique.

Adding an additional non-physical relaxation term to the prognostic model equations relaxes the models state of the atmosphere during the preparation period to the observational data.

A general model equation is for example:

$$\frac{\partial X}{\partial t} = F_M(X) + G(X_{obs} - X)$$

X represents any of the prognostic model variables which should be relaxed towards observations, F_M is the model forcing, and $G(X_{obs} - X)$ the nudging term. G in $[s^{-1}]$ is the relaxation coefficient. Due to the fact that former ECMWF Reanalysis data are used as artificial observations no small scale perturbations are included. Because *observation* data are only available every 6 hours, the nudging data for the time steps inbetween will be calculated by linear interpolation.

Selecting a reasonable value for the nudging coefficient G forms the main difficulty of the Newtonian relaxation (Stauffer and Bao, 1993). For a large G the nudging term dominates the model forcing. This can lead to possible dynamical imbalance amplifications. If G is chosen to small the observations will not have any influence on the model solution. Various considerations can be found in literature (Zou et al., 1992; Stauffer and Bao, 1993). The used values in this study are set to an appropriate value to force the model as close as possible to the ECMWF Reanalysis state to prevent any spin-up problem during the assimilation phase. Temperature, divergence and vorticity are used. Because of the fact that the vorticity represents the slow manifold of the quasi-geostrophic motion, this is describing mainly the evolution of the Rossby type waves for a time-scale of some days. Adjusting the vorticity is therefore a very efficient way to adjust the large scale flow at least in the extra-tropics.

The influence on the model physics can be explained most simple by the thermodynamic energy equation:

$$\frac{dT}{dt} = \frac{Q}{c_p} + \omega\frac{\kappa T}{p} + G(T_{obs} - T)$$

The diabatic heating Q is determined by the release of latent heat, the sensible heat flux at the surface, and the radiative heating. So the relaxation does not modify the diabatic heating only, but the large-scale dynamical quantities as well. Without nudging the balance between the dynamical and parameterized quantities is physically consistent. This changes with the relaxation. The modelled temperature is forced towards the observation and the parameterized values are hindered to reach a balanced state. Similar discussions are valid for the other model equations. The relaxation is introducing a permanent spin-up phenomena into the model, forcing it into the nudging data state space.

The implementation of the nudging technique into ECHAM is straight forward. An integration step is solved by an semi-implicit finite difference scheme in two time steps. The model forcing F_M is calculated providing new values for the prognostic variables $X^m_{t+\Delta t}$. Thereafter the relaxation term is calculated:

$$\frac{X_{t+\Delta t} - X^m_{t+\Delta t}}{2\Delta t} = G(X)[X^{an}_{t+\Delta t} - X_{t+\Delta t}]$$

$X^{an}_{t+\Delta t}$ is the ECMWF Reanalysis which are used as true state estimation.

The observation data in our experiments are ECMWF Reanalysis Data. As input data for the nudging we used spectral ECMWF first guess data, which is a 6 hour forecast of vorticity, divergence and temperature. The model runs have been started from the 1st January 1986 state and integrated for one year and 10 days to adjust to the start date, *real* state, denoted by the ECMWF Reanalysis Data. It has been taken care on the different representation of the orography in both models. No truncation is necessary because the same resolution of T106 has been used. The sequance of preparational steps is given by figure 55.

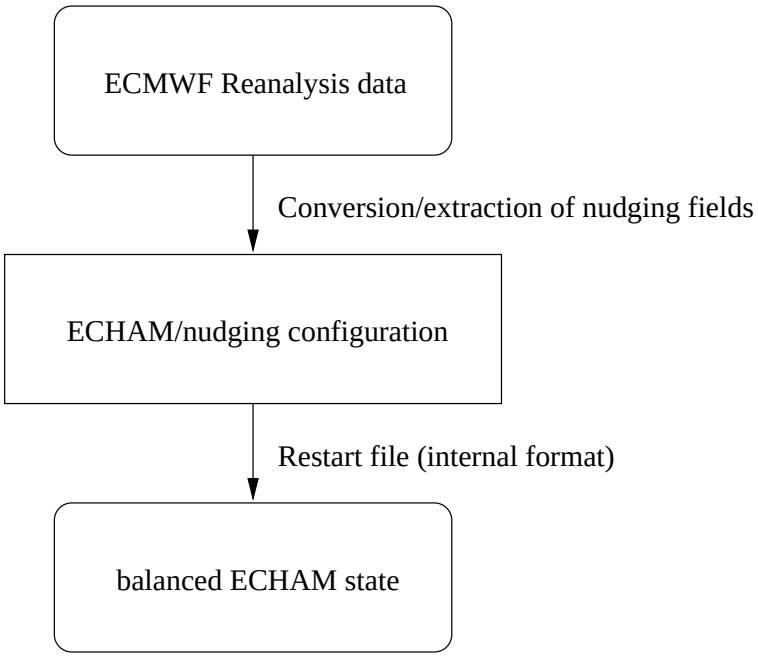

Figure 55: ECHAM state preparations.

At this state we have available all input to perform the assimilation study itself.

10 Assimilation Procedure

To describe the assimilation cycle in detail a flow chart of the system is given in figure 56. It describes top down the sequence of processing.

The first set is already done. The satellite setup is eplained extensively and the forward modeling is performed based on the ECMWF Reanalysis first guess fields. Missing is the modeling of the receiver system. Again, this is done using EGOPS. The assumptions describing the assumed errors is given in table 9.

At this stage of processing we have available the data as they are expected to be delivered by future satellite system. As well available are all observations originaly used by the ECMWF Reanalysis; quality controled and blacklisted. An overview of the coverage with conventionl data is given in figure 57. Remarkable is the quite uneven coverage.

Receiver Sampling Rates	
GPS Sampling Rates	10.0 10.0 [Hz]
GLON Sampling Rates	10.0 10.0 [Hz]
POD Error Modeling/Specifications	
PODErrorModelChoice	Kinematic POD Error Model
ErrApplicationType	Randomly (as rms)
RadialPositionErrorGNSS	0.20 [m]
RadialPositionErrorLEOs	0.40 [m]
AlongRayVelocityError	0.05 [mm/s]
AlongRayAccelError	0.05 [um/s2]
GRAS Antennae Specifications	
-V AntennnaChoice	Used
-V BoresightElevation	27.0 [deg]
-V BoresightAzimuth	180.0 [deg]
-V FOVChoice	Ell_Cartes
-V HPBW Vertical	60.0 [deg]
-V HPBW Horizontal	90.0 [deg]
-V AntennaGain/Boresight	11.0 [dB]
+V AntennaChoice	Used
+V BoresightElevation	27.0 [deg]
+V BoresightAzimuth	0.0 [deg]
+V FOVChoice	Ell_Cartes
+V HPBW Vertical	60.0 [deg]
+V HPBW Horizontal	90.0 [deg]
+V AntennaGain/Boresight	11.0 [dB]
Receiver Performance Modeling	
RecPerfModelChoice	Realistic Perf./Noise Model
LoopBandwidth/singleside	10.0 [Hz]
LEOAntennaeNoiseTemp	150.0 [K]
QuantLevelsADConversion	4
Local Multipath Modeling	
LocalMultipModelChoice	Sinusoidal Multipath Model
MultiPhaseErrPeriod	100.0 [sec]
MultiPhaseErrAmplitude	2.0 [mm]
MultiPhaseErrAmplTopRay	0.0 [mm]
Differencing Treatment/Clocks Modeling	
DiffTreatmentChoice	Ground-based Single Diff.
RelStabilityofWorstClock	1.0E-13 [1secAllan]
AtmNoise per Groundlink	1.0E-13 [1secAllan]

Table 9: Used error characteristics for the receiver system

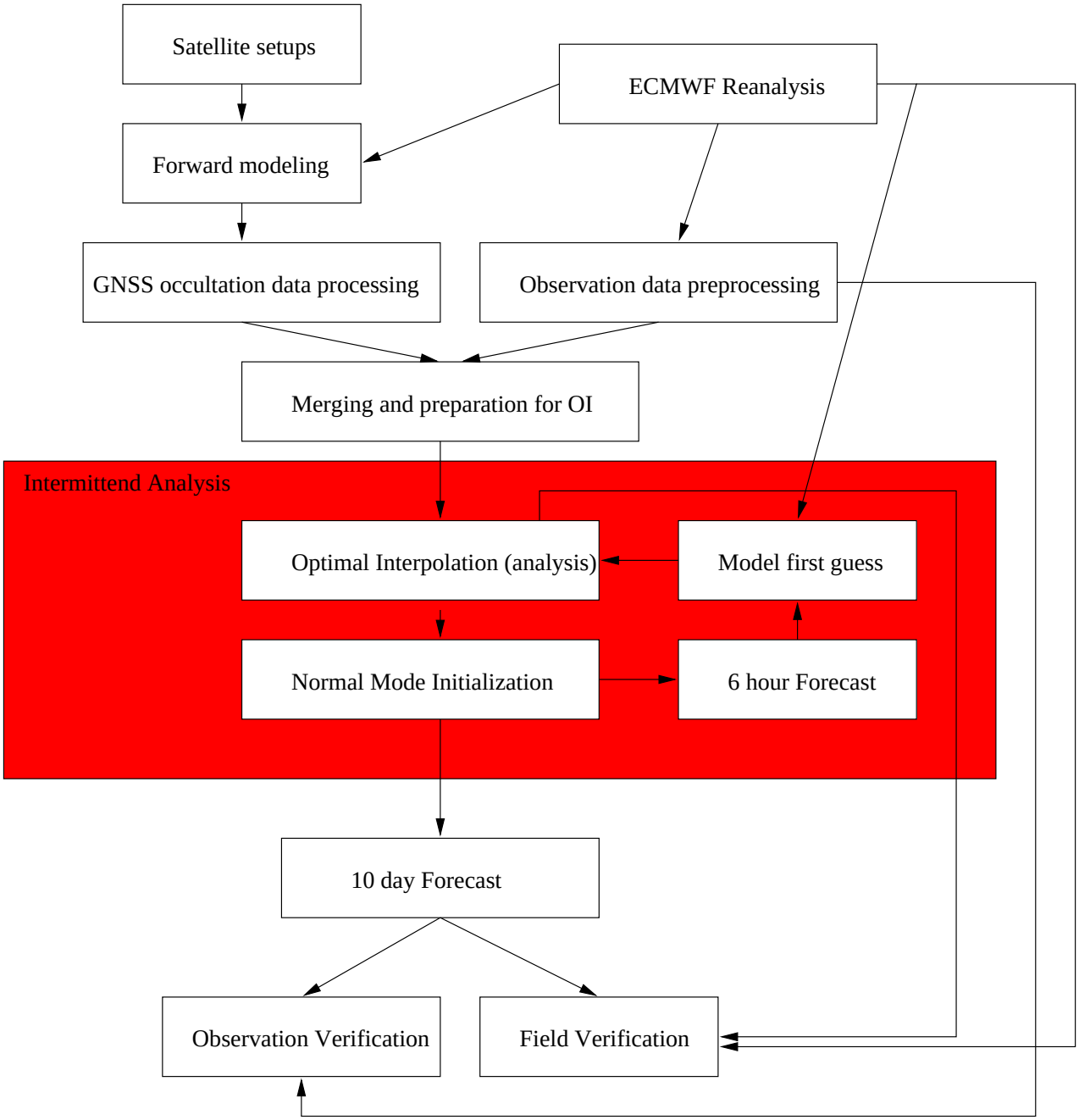

Figure 56: General experiment setup.

10.1 Optimal Interpolation (OI)

Before going on describing the experiment setup the optimal Interpolation (OI) is introduced. The major reason for this is to describe the restricted use of this assimilation scheme to linear observation operators. Optimal interpolation (or statistical interpolation) is based on a statistical approach. A coefficient matrix $\mathbf{K}$ is selected by the following aspects. Given are a covariance matrix of errors $\mathbf{R}$ of the observations and a covariance matrix of errors of a forecast $\mathbf{B}$. $\mathbf{K}$ is selected so that the variance $\mathbf{A}$ of an analysis is minimized:

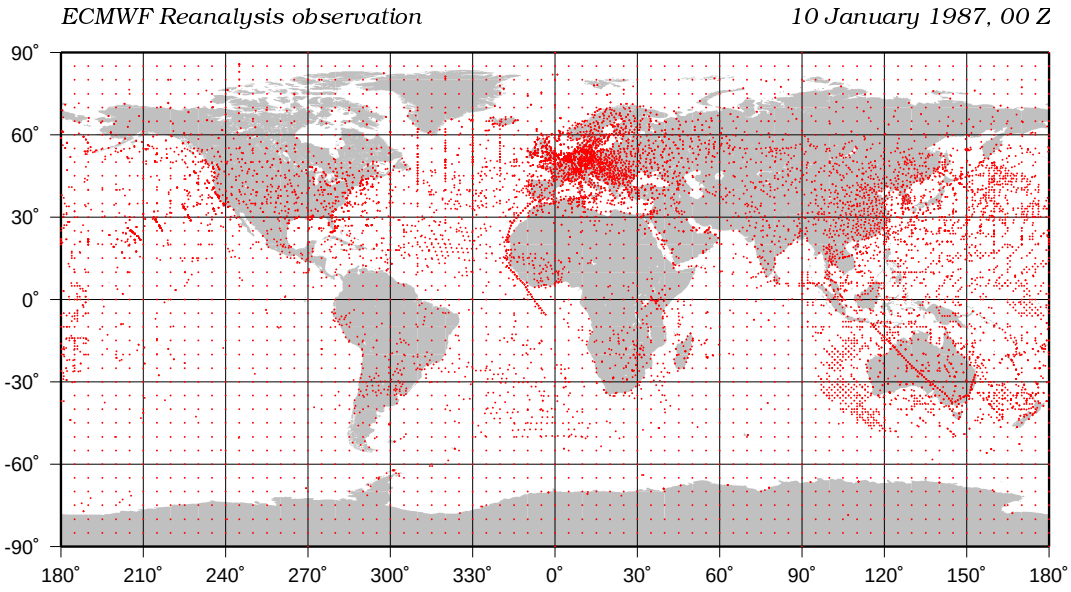

Figure 57: Conventional data coverage.

$$\mathbf{K} = \mathbf{B}\mathbf{H}^{\mathrm{T}}(\mathbf{R} + \mathbf{H}\mathbf{B}\mathbf{H}^{\mathrm{T}})^{-1}$$

$$\mathbf{A} = (\mathbf{I} - \mathbf{K}\mathbf{H})\mathbf{B} = (\mathbf{B}^{-1} + \mathbf{H}^{-1}\mathbf{R}^{-1}\mathbf{H})^{-1}$$

H is the linear interpolation operator projecting the model variables onto the observations which, in general, are not available on the models grid.

Missing link between the available occultation observations and the observation types usable in this setup is the preprocessing of the occultation data to refractivity allowing for a one dimensional variational processing (1DVAR) to derive temperature and humidity profiles.

10.2 GNSS RO preprocessing

First step in processing is based of the algorithms provided by DMI for EGOPS. The DMI-derived enhanced-EGOPS bending angle retrieval tool will be used for bending angle retrieval. It performs statistical optimization and bending angle correction. The DMI-derived Abel

Bending Angle Retrieval Specifications	
BendAngleRetToolChoice	DMI Enhanced Ion.Corr. & Bend.Angle Retrieval
IonoCorrectionType	Bend.Angle Correction
StatOptimizationType	Optimize using m+z BenA Search
Refractivity Profiles Retrieval Specifications	
RefProfRetToolChoice	DMI Abel Transform Refr.Profiles Retrieval
Atmospheric Profiles Retrieval Specifications	
AtmProfRetToolChoice	No Atm. Profiles Retrieval

Table 10: Input for retrieval of refractivity with EGOPS.

Transform tool will be used for refractivity retrieval. This setup is consistent with the assumptions made in the refractivity covariance matrix formulation for the assimilation. To allow for an overview, the specifications are given in table 10.

For a detailed description of the used algorithms we refer to the EGOPS Manual.

To derive temperature and humidity profiles from refractivity the model is given by

$$N = k_1 \frac{p}{T} + k_3 \frac{p_w}{T^2} - C \frac{N_e}{f^2}$$

with k_1, k_2, and C being constants, p the pressure, p_w the water vapour partial pressure, and T the temperature, f the signal frequency, N_e the ionospheric electron density. This model is ambigous regarding temperature and humidity. Therefor we use a variational scheme to resolve this.

In 1DVAR a analyzed column $\mathbf{x}$ of control variables is retrieved by minimizing the cost function J, which penalizes the deviations both from the first guess and from the observations:

$$J = \frac{1}{2}[(\mathbf{x}-\mathbf{x}_f)^{\mathrm{T}}\mathbf{B}^{-1}(\mathbf{x}-\mathbf{x}_f) + (\mathbf{y}_o - \mathcal{H}\mathbf{x})^{\mathrm{T}}\mathbf{R}^{-1}(\mathbf{y}_o - \mathcal{H}\mathbf{x})] \quad \text{with} \quad \begin{array}{ll} \mathbf{x}_a & \text{analysis} \\ \mathbf{x}_f & \text{forecast (first guess)} \\ \mathbf{y}_o & \text{observation} \end{array}$$

$\mathcal{H}$ is the operator which calculates the observed quantities from the model variables. In case of classical observations $\mathcal{H}$ is a simple (linear) interpolation operator. In this case 1DVAR is equivalent to OI. In general $\mathcal{H}$ is a nonlinear operator, for instance the $\mathbf{y}_o$ are the refractivity derived by an occultation.

The error covariance matrix of the observation is derived from the work by Syndergaard in Syndergaard (1999). As background error a variation of the background error for radiosondes is used. The assumptions on the quality below 3-5 km (latitude dependend) is changed because of unknown error behaviour in the lower troposphere, the error of the model is there reduced - trusting more the models results. As well the error of the model is increased by a factor of 2.5 to improve the assumed higher reliability by the GNSS RO derived profiles higher up -

trusting more the observations. For a proper background error covariance matrix retrieval a longer periode of real data is needed.

Summarizing the errors taken into account:

- the background error of the model itself (part of the OI)
- the observation error of the instrument (part of the OI)
- a statistical introduced error in the simulated observations (part of EGOPS)
- a random error introduced by using the ERA 15 analysis data from a different model

The derived GNSS RO data are now converted into variables used by the model and can be incorporated into the standard input format for the OI (see 58).

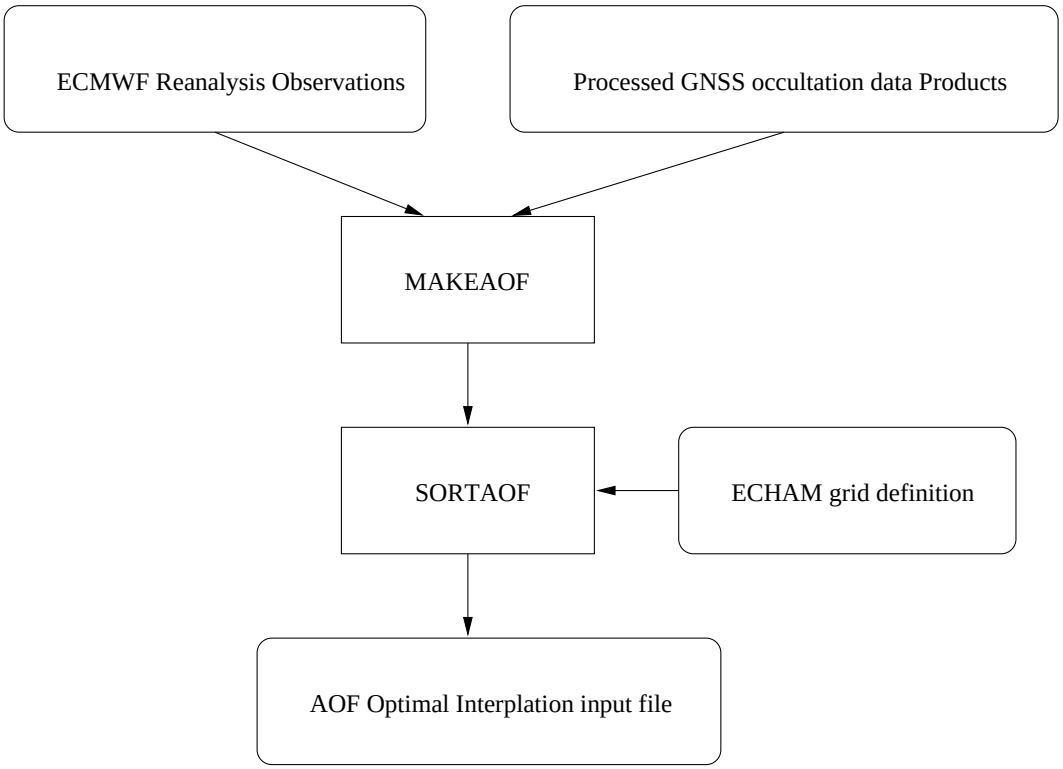

Figure 58: Observation preprocessing.

This part contains as well the split of the observations into several areas to keep the matrix inversions in the OI in a proper size. This may contain the setup of superobservations. A description of this grid is given in figure 59.

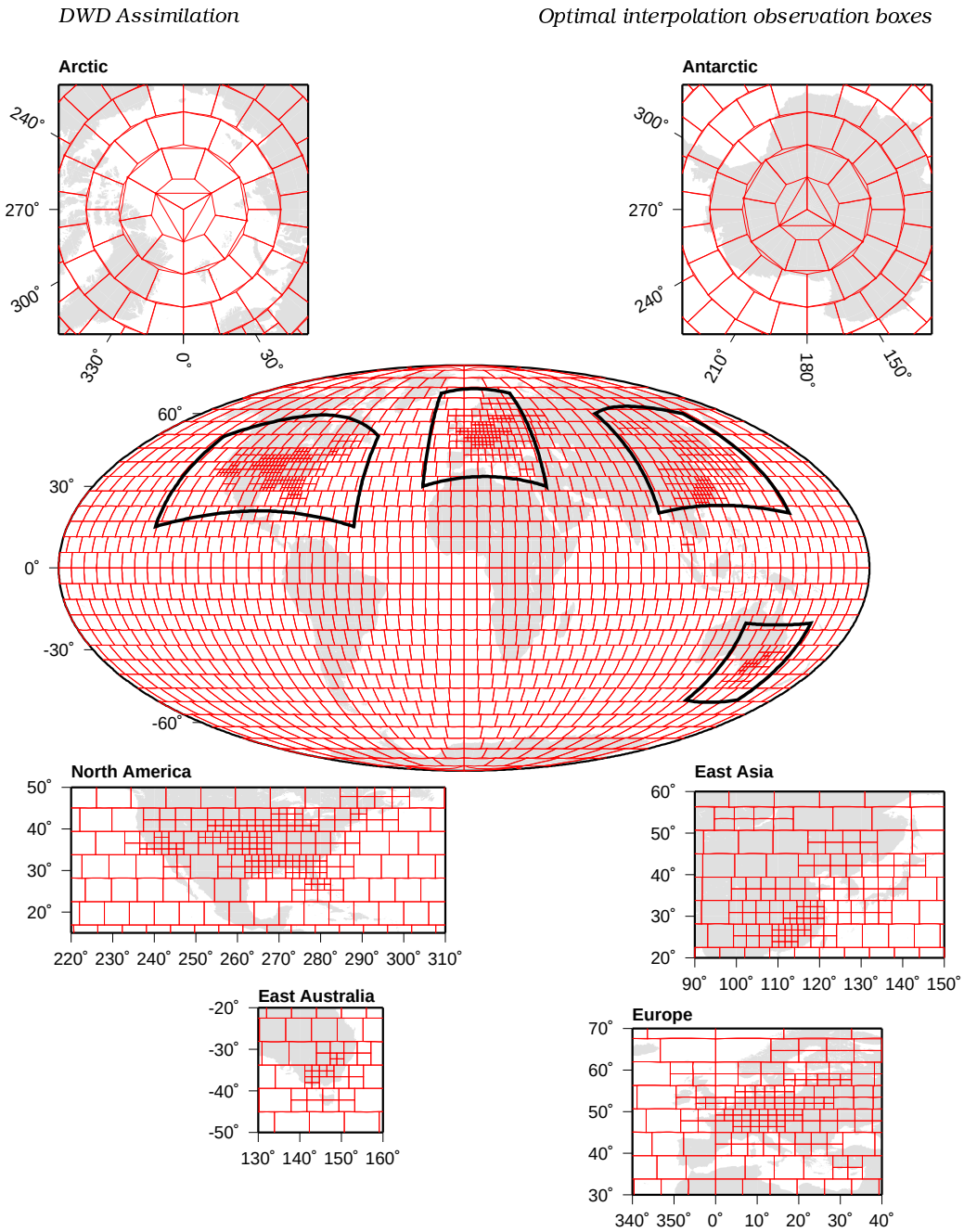

Figure 59: Structure of the single OI areas and subdivision of the original boxes in areas with high observation density.

10.3 Assimilation

The assimilation procedure itself is best described by the following figure 60. The basic is that at one time a analysis is performed, reseting the trajectory of the model back on the real trajectory of the current state of the atmosphere. This is done consecutively. Doing that for some time (6 hour windows) the analysis will get a more reliable trajectory. Once a while a 10 day forecast is started while the usual intermittend analysis is ongoing.

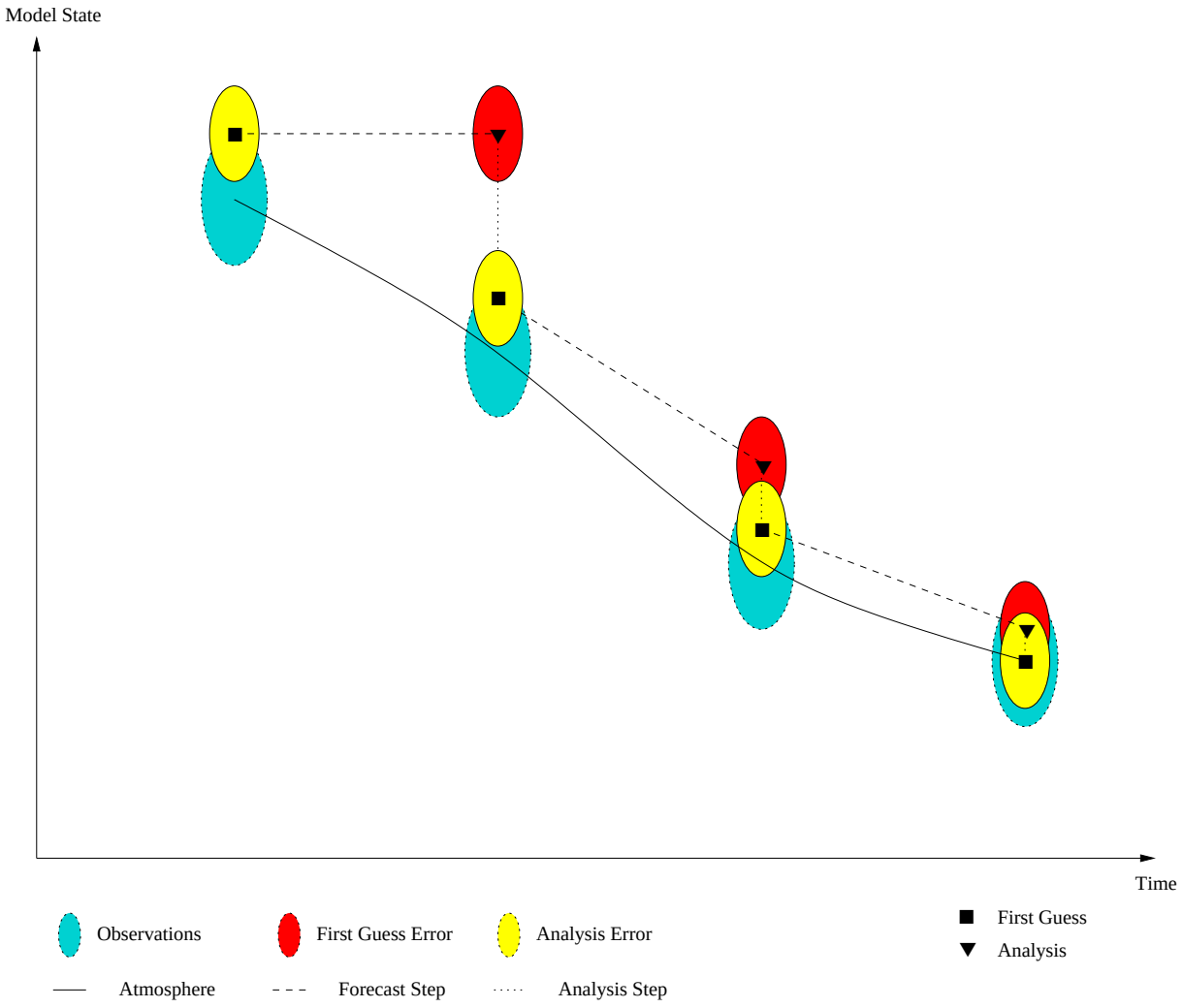

Figure 60: Processing structure of the intermittend data assimilation scheme.

In detail (figure 61) this is outlined in terms of the model integrations. This is the implementation used in this study. Due to the large amount of occultation to be produced the assimilation experiment has been set for one 10 day periode.

Before showing the results several possible measures of the performance will be discussed to select the most meaningful measure.

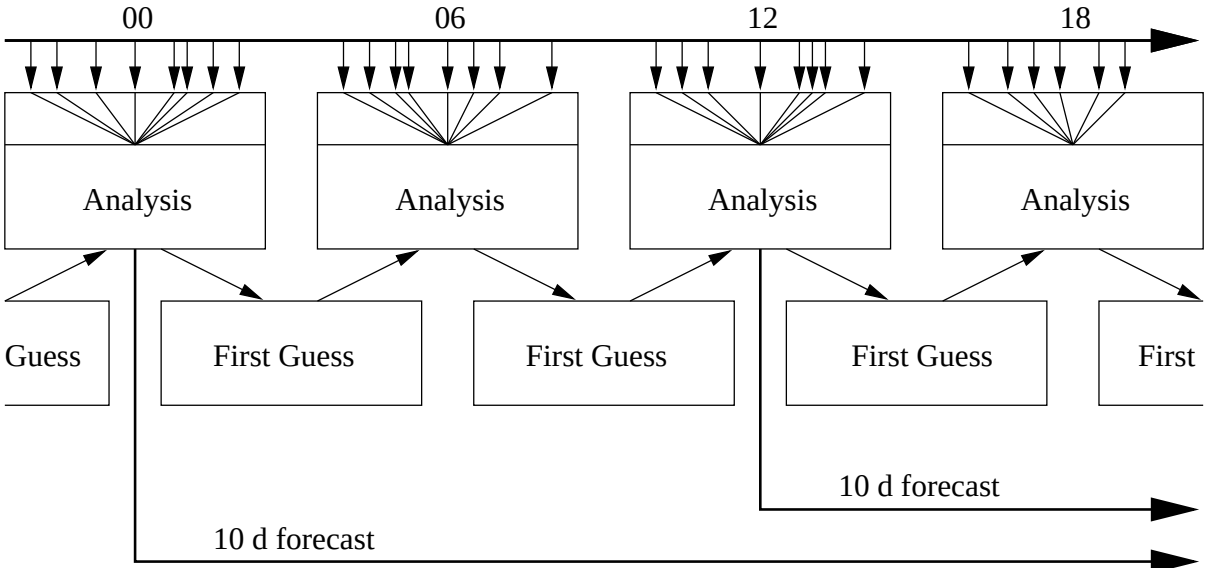

Figure 61: Processing structure of the real application of the intermittend data assimilation.

10.4 Statistical Measures

Selecting a single measure to compare the performance of the different selected test cases is an important task. Therefore we provide a description of the standard measures used. The same time this are describing the information content of the selected measure which is the anomaly correlation.

- Error is the simple difference of forecast minus verifying analysis or observation equals error between scalar quantities which can be arithmetically-averaged in area and time. The difference (error) field provides a quick look at a model's forecast performance or bias. Bias or tendency describes whether a synoptic field or feature is under or over-forecast.

  Operational: a series of error graphics for one or more levels, at least SLP and 500 mb spanning several forecast intervals, is very helpful in determining the intensity and movement (position and direction) forecast errors of synoptic, and sub-synoptic scale features.

  Advantages: simple error fields are very helpful in displaying discrepancies in the intensity and position of synoptic, and sub-synoptic scale features. The basic difference fields are straight forward, easy to compute and understand. They provide a quick look at model forecast performance, especially in the operational setting.

  Disadvantages: it is often necessary to make objective statements regarding which areas are significantly different between two fields.

- Root Mean Square Error (RMSE) is defined as the positive square root of the mean square error (MSE). MSE is the mean square of any residual. RMSE is the also called the standard error of estimate.

  Operational: RMS errors typically increase with forecast time. RMS is generally greater in Winter than in Summer, because Summer typically has more moderate weather compared to Winter. RMS is very useful to verify the wind vector which is decomposed to the u and v components.

  Advantages: simple to produce, RMSE/MSE measures provide useable statistics to verify model forecasts, and are applicable to a large number of analysis and forecast elements, and model types.

  Disadvantages: RMSE and MSE tend to conceal intensity (SLP and height) and movement (position/directional) errors. The nature of these errors is sensitive to the variance within the data field. They must be normalized or the score regionalized before a great deal of emphasis is placed upon the interpretation of the RMSE and MSE value. They are particularly sensitive to large differences, and to any data field smoothing or filtering in the analysis and forecast model.

- Standard Deviation (SD) is a measure of the scatter or variability about the mean in a series of observations. SD is the positive square root of the variance.

  SD advantages and disadvantages are similar to RMSE and MSE.

Operational: the importance of the SD in relation to the RMSE/MSE is often overlooked in verification systems. Many studies place too much emphasis on the RMSE values of hemispheric fields without regard for the inherent variability within the system. Certain geographic regions are naturally more variable than others, both observationally and in model simulations. The "naturally more variable areas" influence the RMSE value much more than the "less variable areas". Thus, the variance of the individual grid points must be known before any significant degree of relevance is placed on the RMSE.

- Anomaly Correlation is widely used to evaluate large-scale/medium-range forecast skill and provides a reliable indication of overall model skill. The correlation coefficient is a generalized measure of a relationship between pairs of variables from two samples. The anomaly correlation is the relationship between observed and predicted deviations from climatology of the 500 mb height field. It is influenced by trends in the data, and therefore uses departures from a monthly climatology (interpolated to the current day). (NOGAPS uses the average of the 12-hourly correlation values of the height field interpolated from the monthly climatology at one or more levels of the atmosphere.)

  Operational: the anomaly correlation skill score can be regionalized and used with basic forecast error graphics which depict the U/L synoptic flow pattern. The regional anomaly scores can then be directly related to basic intensity and position errors associated with circulation changes, and individual synoptic and sub-synoptic scale features. An anomaly correlation score of one (1.0) implies a perfect forecast. Based on experience with the anomaly correlation, a score near 0.6 suggests forecast errors are sufficiently large to indicate minimal skill. A score below 0.6 signifies a forecast is not useful. A score below 0.6 occasionally occurs for all models at 120 h, and typically represents a rapidly changing synoptic pattern. A low anomaly score can also occur when model history continuity is broken because of computer problems. Forecast models typically take 1 to 2 days to re-establish model equilibriums in moisture and boundary layer parameters.

  Advantages: easy and inexpensive to compute, the anomaly correlation skill score provides a reliable indication of overall forecast skill. The anomaly correlation skill score uses a climatology to account for seasonal and monthly anomalies.

  Disadvantages: The anomaly correlation is especially sensitive to position errors in large circulation systems.

- Regression Techniques are comparable to RMSE and the correlation coefficient. Regression is often used as an adjustment to forecasts based strictly upon a statistically measured relationship. However, regression analysis does not always lend itself to easy, straight forward interpretation.

  Operational: especially useful when comparing related model analysis and forecast values to traditionally observed environmental parameters.

  Advantages: simple and inexpensive to compute, regression can statistically compare various related physical parameters. It is useful for examining the difference between predicted and analyzed or observed parameters. It is therefore possible to estimate a future state based solely on the observed behavior of the environment.

  Disadvantages: difficult to assign any statistical confidence to regression results. Simple linear regression equations are subject to significant sampling errors that do not

reflect the real environment's complicated non-linear dynamics and physics.

11 Results and Conclusions

The most important fact on the comparision is the possibility to compare to the performance of other NWP models and a relatively simple measure for representing the results. This is after carefully evaluating the given possibilities, the anomaly correlation. We will present the standard anomaly correlation of the 500 hPa geopotential field and additionally the 100 hPa geopotential field.

The results of the 500 hPa geopotential anomaly corelation (see figures 62 and 63) show a difference in the results on the northern and southern hemisphere. The gain in crossing the persistence level of 60 % is about one day better on the northern hemisphere. This difference vanishs on the 100 hPa level (figures 65 and 64). The amount of conventional observation data in the Northern hemisphere is much larger than in the Southern which results in the usual forecast performance gap between the hemispheres - major responsible influence is the poor knowledge of water vapour in the Southern hemisphere. In the upper part of the atmosphere the GNSS RO derived data dominate and equalize the state - here the influence of water vapour can be neglected. Differences in the 100 hPa level are only marginal any more.

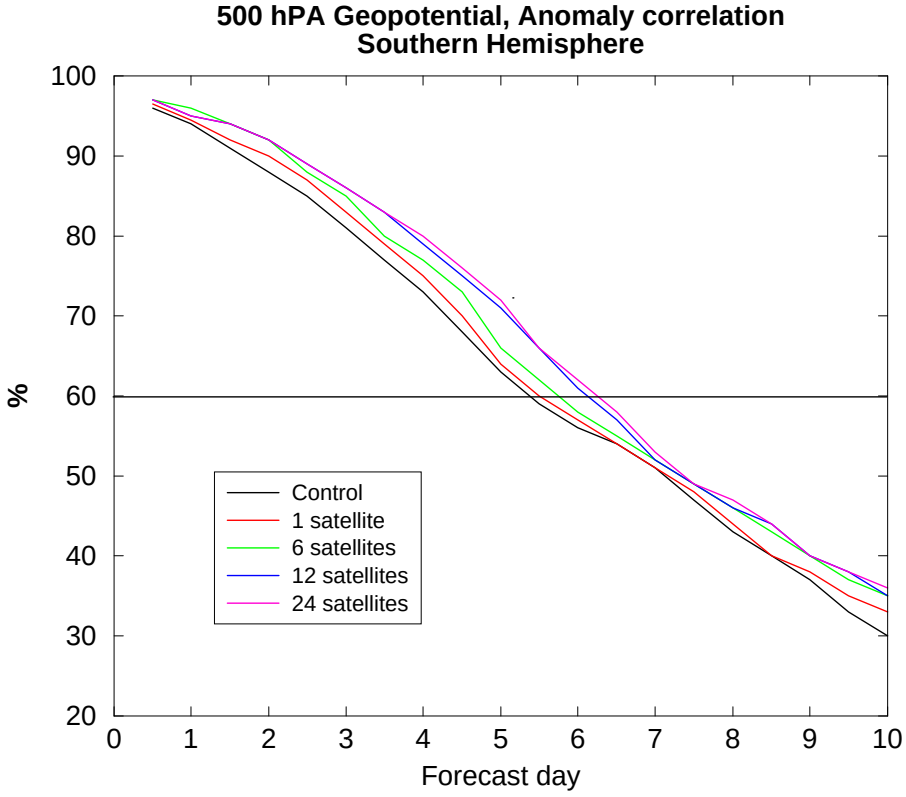

Figure 62: 500 hPa geopotential, anomaly corelation, Southern hemisphere

Another important aspect is the convergence of the cases with 12 and 24 satellites. This can be seen in all results. This seems to show a saturation of the information content of additional

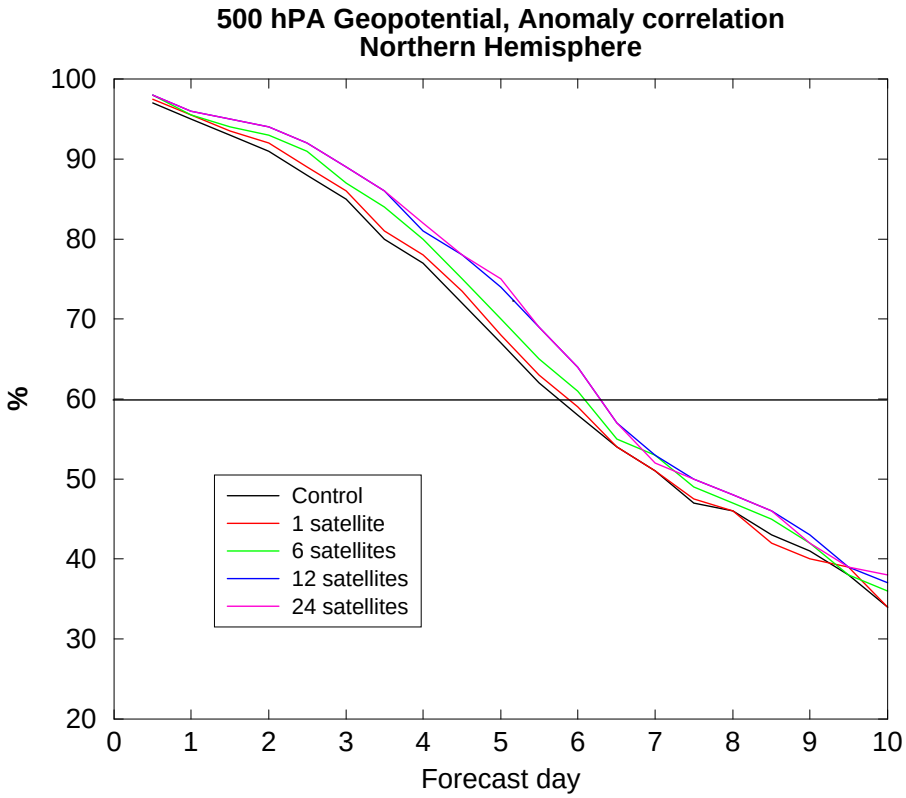

Figure 63: 500 hPa geopotential, anomaly corelation, Northern hemisphere

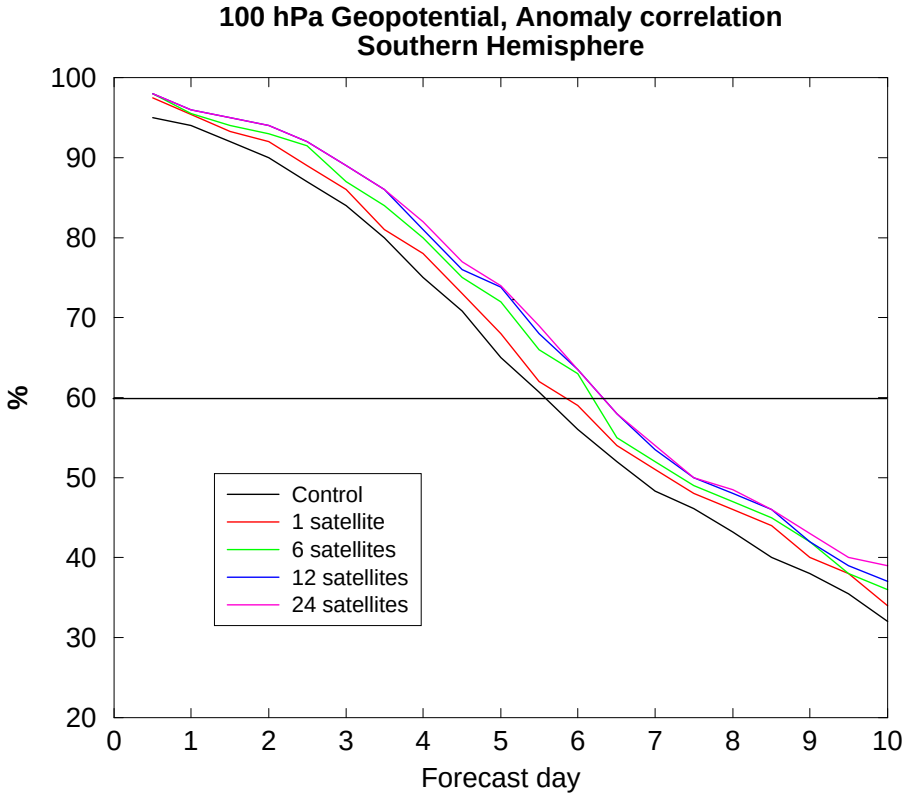

Figure 64: 100 hPa geopotential, anomaly corelation, Southern hemisphere

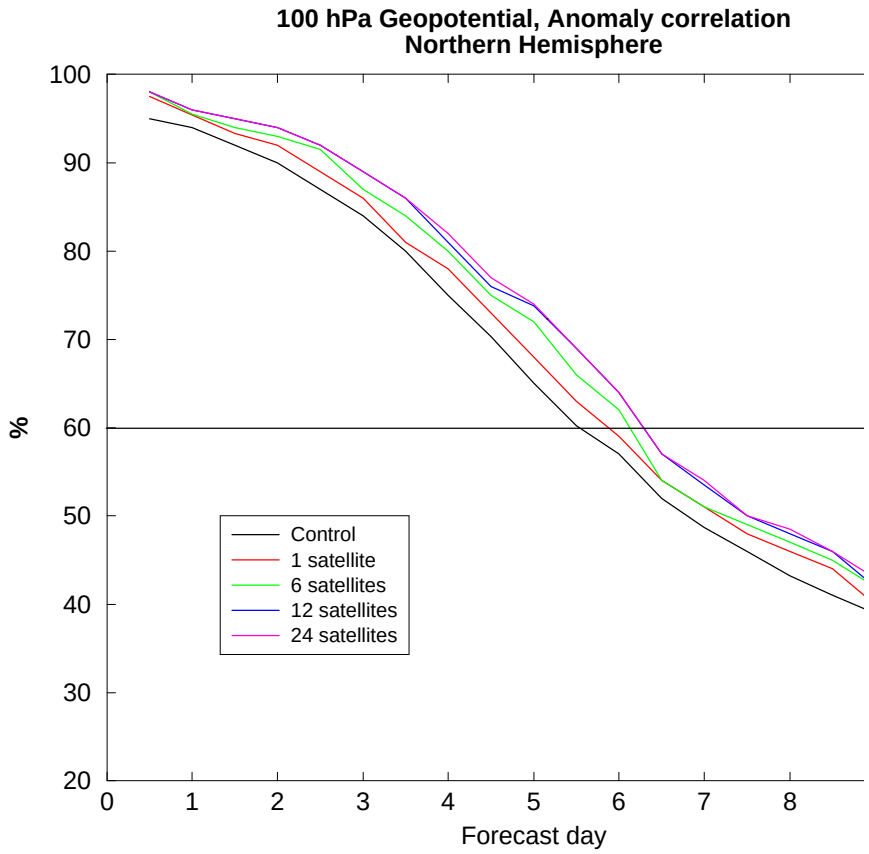

Figure 65: 100 hPa geopotential, anomaly corelation, Northern hemisphere

observations. The defined horizontal area measured by the GNSS RO is given by the GRAS SAG to be around 300 km. So most information is getting redundant, explaining the results.

Beside the explained saturation effect remarkable is the improved forecast performance by approximatelly one day. This is a promising result for a single new instrument. But we would like to warn on taking this result as absolut measure. An OSSE is always overestimating the influence of the results due to the fact that the generated observations fit very well the models state.

A comparison with the forecast performance of several well known NWP centers shows that the results of this experiment fit very well in the standard range of forecast skills (see figure 66).

Concluding all information given by our experiments the following points are the most important:

- GNSS RO data improve forecasts - in the experiments by a remarkable additional 1 day.
- There is a saturation effect somewhere between 12 and 24 satellites. This has to taken very carefully: rising and setting LEOs have been taken into account and a full set of GPS

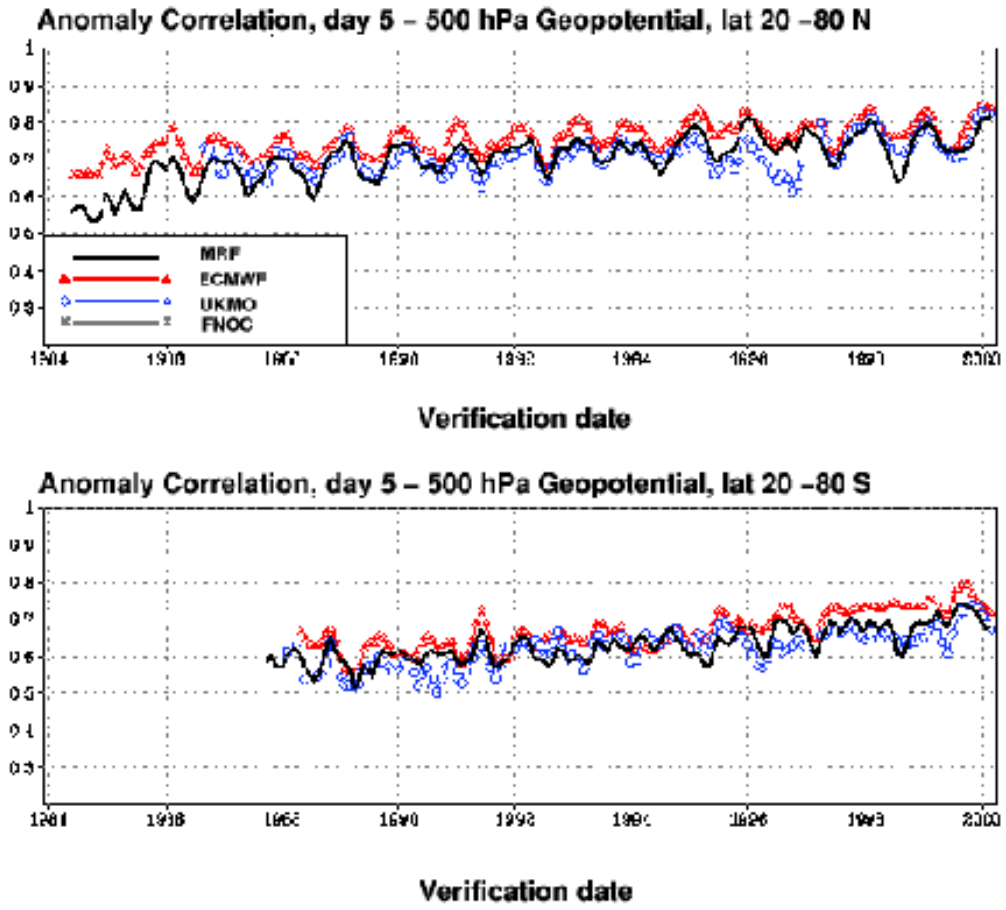

Figure 66: NCEP intercomparison of 500 hPa geopotential anomaly correlation of several NWP models.

and GLONASS satellites. Currently GPS only is working and most likely GLONASS will never work. Which means that only half of the occultations might be available in the real world, doubling the necessary number of LEO satellites and requiring a new orbit setup - different to the one proposed in this study. On the other hand the setup of an European system, GALILEO, is on the way. In case this is available, we will get the simulated environment of this study.

- The technique used to process the GNSS RO data is not optimal in using the information content. Improvements may be possible with advanced techniques in the near future (assimilation of bending angles based on ray tracing for 3/4DVAR).

- The handling of error covarince matrices have been taken very carefully, but nevertheless only a long term monitoring of an actual flying instrument can give really reasonable numbers.

Acknowledgement

We have to thank ESA for providing the funds for this study and support as well as patient in all possible situation. DWD has kindfull provided their Optimal Interpolation scheme and all necessary software around this large package. ECMWF has provided the ERA15 Reanalysis data and the observations used in this project.

References

Anthes, R., Exner, M., Rocken, C. and Ware, R. (1997): *Results from the GPS/MET experiment and potential applications to GEWEX*. GEWEX News, **7**, 3–6.

Eyre, J. R. (1994): *Assimilation of radio occultation measurements into a numerical weather prediction system*. Tech. Rep. Technical Memorandum No. 199, European Center for Medium-Range Weather Forecast.

Fjeldbo, G. and Eshleman, V. R. (1968): *The atmosphere of Mars analyzed by integral inversion of the Mariner IV occultation data*. Planetary and Space Science, **16**, 123–140.

Gorbunov, M. E. and Sokolovskiy, S. V. (1993): *Remote sensing of refractivity from space for global observations of atmospheric parameters*. Tech. Rep. Report No. 119, Max-Planck Institute for Meteorology, Hamburg.

Gorbunov, M. E., Sokolovskiy, S. V. and Bengtsson, L. (1996a): *Space refractive tomography of the atmosphere: modeling of direct and inverse problems*. Tech. Rep. Report No. 210, Max-Planck Institute for Meteorology, Hamburg.

Gurvich, A. S. and Krasil'nikova, T. G. (in Russian 1987, in English 1990): *Navigation satellites for radio sensing of the Earth's atmosphere*. Soviet Journal of Remote Sensing, **7, no. 6**, 1124–1131.

Hocke, K. (1997): *Inversion of GPS meteorology data*. Annales Geophysicae, **15, no. 4**, 443–450.

Kliore, A. J. et al. (1965): *Occultation experiment: Results of the first direct measurement of Mars' atmosphere and ionosphere*. Science, **149**, 1243–1248.

Kuo, Y.-H. et al. (1997): *Sounding through an intense upper level front*. Bulletin of American Meteorological Society.

Kursinski, E. R. et al. (1996): *Initial results of radio occultation observation of Earth's atmosphere using the global positioning system*. Science, **271**, 1107–1110.

Kursinski, E. R. et al. (1997): *Observing earth's atmosphere with radio occultation measurements using the global positioning system*. Journal of Geophysical Research, **102, no. D 19**, 23429–23465.

Lindal, G. F. (1992): *The atmosphere of Neptune: An analysis of radio occultation data acquired with Voyager*. Astronomical Journal, **103**, 967–982.

Lindal, G. F. et al. (1990): *The atmosphere of Neptune: Results of radio occultation measurements with the Voyager 2 spacecraft*. Geophysical Research Letters, **17**, 1733–1736.

Melbourne, W. G. et al. (1988): *GPS geoscience instrument for EOS and Space Station*. Tech. Rep. JPL Proposal to NASA AO OSSA-1-88, JPL.

Mortensen, M. D. and Høeg, P. (1998): *Inversion of GPS occultation measurements using fresnel diffraction theory*. Geophys. Res. Lett.

Phinney, R. A. and Anderson, D. L. (1968): *On the radio occultation method for studying planetary atmospheres*. Journal of Geophysical Research, **73**, 1819–1827.

Rangaswamy, S. (1976): *Recovery of atmospheric parameters from the APOLLO/SOYUZ-ATS-F radio occultation data*. Geophysical Research Letters, **8**, 483–486.

Rocken, C. et al. (1997): *Verification of GPS/MET data in the neutral atmosphere*. Journal of Geophysical Research.

Stauffer, D. R. and Bao, J.-W. (1993): *Optimal determination of fdda coefficients using the adjoint equations*. Tellus, **45**, 358.

Syndergaard, S. (1999): *Retrieval Analysis and Methodologies in Atmospheric Limb Sounding Using the GNSS Radio Occultation Technique*. Tech. Rep., DMI, Copenhagen, Denmark. No. 99-6.

TERMA Elektronik AS (1998): *Final report: Study of synergies and impacts of global navigation satellite systems for operational meteorology and climatology*. Tech. Rep., ESA. Contract No. 11930.

Ware, R. et al. (1996): *GPS sounding of the atmosphere from Low Earth Orbit: Preliminary results*. Bulletin of the American Meteorological Society, **77, no. 1**, 19–40.

Yakovlev, O. I., Matyugov, S. S. and Vilkov, I. A. (1995): *Attenuation and scintillation of radio waves in the Earth's atmosphere from radio occultation experiment on satellite-to-satellite links*. Radio Science, **30, no. 3**, 591–602.

Zou, X. et al. (1998a): *Direct assimilation of GPS/MET refraction angle measurements: Part I: Concept and results of raytracing*. Journal of Geophysical Research. submitted.

Zou, X. et al. (1998b): *Direct assimilation of GPS/MET refraction angle measurements: Part II: Variational assimilation using adjoint techniques*. Journal of Geophysical Research. submitted.

Zou, X., Kuo, Y.-H. and Guo, Y.-R. (1995): *Assimilation of atmospheric radio refractivity using a nonhydrostatic adjoint model*. Monthly Weather Review, **123**, 2229–2249.

Zou, X., Navon, I. M. and Ledimet, F. X. (1992): *An optimal nudging data assimilation scheme using parameter estimation*. Quart. J. R. Met. Soc., **118**, 1163.